UNIVERSITY OF CALIFORNIA SAN DIEGO

Patternable Smart Materials for Actuation of Mesoscale Soft Machines

A dissertation submitted in partial satisfaction of the
requirements for the degree
Doctor of Philosophy

in

Engineering Sciences (Mechanical Engineering)

by

Adriane Fernandes Minori

Committee in charge:

Professor Michael T. Tolley, Chair
Professor Shenqiang Cai
Professor Nicholas Gravish
Professor Darren Lipomi
Professor Frank Talke

2021

The dissertation of Adriane Fernandes Minori is approved, and it is acceptable in quality and form for publication on microfilm and electronically.

University of California San Diego

2021

DEDICATION

To my family, friends and those who believed in me.

TABLE OF CONTENTS

LIST OF FIGURES

ACKNOWLEDGEMENTS

My Ph.D. would not have been the same without all the amazing support, help and belief I received during this journey.

First, I would like to thank my advisor Prof. Mike Tolley. Thank you for your guidance, patience, and support. I am grateful for you belief in me at key moments during my journey, and for the amazing opportunities you allowed me to have in the Bioinspired and Robotics Design lab. The research and creative freedom you gave me has enabled me to grow as an independent researcher.

I would also like to thank my committee members, Professors Shengqiang Cai, Nicholas Gravish, Darren Lipomi, and Frank Talke. Thank you for your time and invaluable feedback, as well as the resources provided whenever necessary to conduct interdisciplinary research.

My experience would also not be the same without all the incredible people in the Bioinspired and Robotic Design lab. Thank you all for the insightful discussions, suggestions, shared social events, support, and collaborations. Our time together made my foreign experience in graduate school feel less foreign. I am particularly fortunate to have met and spent time with starting Ph.D students Ben, Calleb, Dylan, Will and later on with Saurabh, Paul, Jess, Michael, Emily, Iman and Jiayao. A huge thank you to all of you, including past visitors, and members in the lab, you made my graduate school experience more enjoyful.

Thanks also to all of my collaborators/coauthors and undergraduates for your time and effort towards each project involved. I learned a lot from you. In particular, thank you Saurabh, Qiguang, Paul and Iman for your time and discussions. Our knowledge exchange, conversations and overall interactions while working together were invaluable. It allowed me to broaden my skill set and consequentially grow as researcher.

I would also like to thank all the colleagues, mentors and professors I had during and before my graduate studies at UCSD. Thank you for your knowledge, experience, advice and support, they shaped me as a person. Thank you Professors Paulo Arratia and Mark Yim for the

opportunity to work with you and your groups at UPenn, as well as all the colleagues, staff and faculty I had the chance to interact with during my time there. That experience allowed me to broaden my research skills and interests. Additionally, I would like to dedicate a special thanks to my high-school and college professors (specially to those no longer here). You provided the foundations that I needed to arrive at this stage in my journey.

Also, thank you to all the staff and people at UCSD who helped me in one way or another.

Finally, a warm thank you to my parents, brothers and friends for their unshakable support and being the fuel to my resilience whenever needed. You are my pillars.

Chapter 2, contain material as it appears in **Minori, A**., Jadhav, S., He, Q., Cai, S., & Tolley, M. T. (2017, September). Reversible actuation of origami inspired composites using liquid crystal elastomers. In Smart Materials, Adaptive Structures and Intelligent Systems (Vol. 58257, p. V001T08A015). American Society of Mechanical Engineers.The dissertation author was the primary investigator and author of this paper.

Chapter 3, in full, is a reprint of the material as it appears in **Minori, A. F.**, He, Q., Glick, P. E., Adibnazari, I., Stopol, A., Cai, S., Tolley, M. T. (2020). Reversible actuation for self-folding modular machines using liquid crystal elastomer. Smart Materials and Structures, 29(10), 105003. The dissertation author was the primary investigator and author of this paper.

Chapter 4, in part, is currently being prepared for submission for publication. **Minori, A.F.**, Jadhav, S., Chen, H., Fong, S., Tolley, M. T.(2021) "Soft Power Amplification System for Jumping using Patternable Artificial Muscle and Snap-through of Shells". The dissertation author is the primary investigator and author of this paper.

VITA

2008-2013	B. S. in Mechatronics Engineering, Universidade do Estado do Amazonas
2014-2015	Research Assistant, University of Pennsylvania
2017	M.S. in Engineering Sciences (Mechanical Engineering), University of California San Diego
2015-2021	Ph. D. in Engineering Sciences (Mechanical Engineering), University of California San Diego

PUBLICATIONS

Minori, A.F., Jadhav, S., Chen, H., Fong, S., Tolley, M. T. (2021) "Soft Power Amplification System for Jumping using Patternable Artificial Muscle and Snap-through of Shells". *In Preparation.*

Minori, A. F., He, Q., Glick, P. E., Adibnazari, I., Stopol, A., Cai, S., Tolley, M. T. (2020). Reversible actuation for self-folding modular machines using liquid crystal elastomer. *Smart Materials and Structures*, 29(10), 105003.

He, Q., Wang, Z., Wang, Y., **Minori, A.**, Tolley, M. T., Cai, S. (2019). Electrically controlled liquid crystal elastomer–based soft tubular actuator with multimodal actuation. *Science advances*, 5(10), eaax5746.

Minori, A., Jadhav, S., He, Q., Cai, S., Tolley, M. T. (2017, September). Reversible actuation of origami inspired composites using liquid crystal elastomers. In *Smart Materials, Adaptive Structures and Intelligent Systems* (Vol. 58257, p. V001T08A015)

Minori A., Shih B., Christianson C., Tolley M. T. (2016), "3D Printed Shape Memory Polymer Composite for Fabric Actuation", Robot Makers 2 Workshop, *Robotics: Science and Systems (RSS)*,Ann Arbor, MI, June.

ABSTRACT OF THE DISSERTATION

Patternable Smart Materials for Actuation of Mesoscale Soft Machines

by

Adriane Fernandes Minori

Doctor of Philosophy in Engineering Sciences (Mechanical Engineering)

University of California San Diego, 2021

Professor Michael T. Tolley, Chair

In applications such as search-and-rescue and minimally invasive surgeries, as well as devices for aerospace (e.g., solar panels), there is a need for lightweight, deployable, compact, and scalable systems. Traditional robots made of rigid parts have been explored for repetitive tasks in industrial settings or daily tasks such as cleaning. However, is still challenging to achieve less bulky or ubiquitous solutions as observed in nature to morph and adapt their shapes given an environment or need. For instance, organisms such as ladybugs, pinecones, and jumping gal maggot fleas have achieved mesoscale morphability via folding or compliance of their body for locomotion and survival.

Inspired by nature, self-folding and soft robots have been developed by exploring the

intersection between rapid fabrication and soft materials. However, it is still challenging to achieve mesoscale actuation that can be easily integrated to these systems while still leveraging their advantages towards compact, lightweight, scalable and deployable robots. For instance, traditional motors (e.g., electromagnetic motors) enable simple and accessible integration with other electronic parts to achieve autonomous robots. Despite that, they are not simple to pattern (i.e. adapt its shape), to scale (i.e. size), and to integrate with soft materials and rapid fabrication methods. In the intersection of these desired features lies the opportunity to explore actuation methods and system designs using smart materials that inherently respond to stimuli and behave as artificial muscles.

In this thesis, I propose to leverage the advantages of smart materials to achieve patternable actuation for mesocale self-folding and soft robots. When combined with lightweight composite mechanisms, these smart material actuators enable new types of lightweight, compact, and modular robots. First, I propose an approach that explores the artificial muscle liquid crystal elastomer (LCE) advantages with rapid fabrication techniques towards reversible self-folding composite hinges. Second, I develop a new methodology to achieve reversible, lightweight, modular, and patternable self-folding machines with a single layer of LCE. Then, I focus on the challenge of amplifying the power output of artificial muscles that offer desirable features for mesoscale actuation but are inherently slow. To achieve this power amplification, I developed a modular system with a nonlinear elastic element to slowly store energy, and release it rapidly when triggered by a latch mechanism.

This work lays the foundation for applications that go beyond mesoscale actuation—for instance, exploring these methodologies that combine smart materials with composite mechanisms towards embodied computing, sustainable robots, and interactive systems.

Chapter 1

Introduction

Robots have been explored in repetitive tasks in industry (e.g., assembly lines) or even in daily tasks such as cleaning (e.g., roomba robots). However, the hardware of these robots is composed of rigid parts that pose significant challenges for applications in constrained environments that require lightweight, compact, deployable, and scalable systems. For instance, there is a need for such systems in search-and-rescue, aerospace (e.g., solar panels, and launching devices) and medical applications (e.g., minimally invasive surgeries). This challenge has provided an opportunity for designing robots that can adapt their body by ubiquitously transforming its shape to fulfil those needs.

Nature provides some insights about ways to achieve these deployable and adaptable systems. For instance, a ladybug can fold and unfold its wings accordingly for locomotion [1], whereas a larvae of gal maggot leverages the compliance of its body to achieve ballistic motions for jumping [2]. Inspired by some of these features of folding and compliance, new design and rapid fabrication approaches (e.g., laser cutting, printing) have propelled the emergence of origami-inspired and soft robots that have expanded the possibilities to achieve morphing and adaptable robots [3, 4].

For instance, origami-inspired robots have taken advantage of folding to develop mesocale

machines that can self-fold for deployment [5], are compact and scalable [6]. These features can be explored for search-and-rescue [7] and minimally invasive medical applications (e.g., drug delivery)[8]. Robots made of soft materials, on the other hand, have bridged the fields of chemistry, material science and robotics by leveraging the intelligence or compliance inherent from materials to develop robots that utilize the properties of materials such as compliance to mitigate impact [9], adapt to constrained environments [10], and safely interact with humans and environment [11].

However, while the body of these mesocale robots can achieve deployable, deformable and compliant shapes, it is still challenging to achieve actuation with complementary features that do not hinder those capabilities. For instance,traditional motors (e.g., electromagnetic motors) enable simple and accessible integration with other electronic parts to achieve autonomous robots. However, they are not simple to pattern (i.e., adapt their shape), to scale (i.e., size and quantity), and to integrate with soft materials and rapid fabrication methods. The desirable features for actuation towards ubiquitous mesocale origami and soft robots include: i) patternable (tunable shape and performance), ii) amenable to system integration (can be easily integrated with system's fabrication process and parts), iii) lightweight (without significantly compromising compliance for load bearing).

There are different actuators that are soft and behave similarly to muscles (artificial muscles) [12] and their advantages and disadvantages will be discussed throughout this dissertation based on the application and problem being solved. Among those artificial muscles, smart materials that are designed to respond to a stimuli, in particular those activated by temperature are capable to achieve all of those three desirable features. For instance, shape memory polymer (SMP), liquid crystal elastomers (LCEs) and shape memory alloys (SMAs), are materials that are lightweight, patternable (e.g., their shape can be easily tuned based on geometry, as well as their mechanical performance such as actuation strain and stress, based on their synthesis)[13]. Furthermore, they can be electrically activated via Joule heating at low voltages (< 12 V) making

them accessible and simplifying their integration with scalable, compact and flexible electrical systems [14, 15, 16, 17].

In particular, LCEs are polymers that contain the self-organization of liquid crystals and mechanical properties of elastomers [18]. This thesis focuses on the exploration of these inherent properties to achieve patternable actuation of LCEs for mesocale self-folding and soft robots. Each chapter provides the background between the advantages and disadvantages for actuating mesocale soft machines and proposes new design methodologies that use artificial muscles combined with lightweight composite mechanisms to enable new types of lightweight, compact, and modular robots.

1.1 Thesis Overview and Contributions

The outline of the chapters and the summary of the main contributions of this thesis are described below:

Chapter 1: Introduction

- This chapter provides the motivation for the research topic and relevance of this thesis as well as relevant background on previous work related to mesocale robotics and patternable smart materials.

Chapter 2: Reversible actuation of origami inspired composites using liquid crystal elastomers

This chapter address the challenge: how to achieve reversible self-folding with lightweight and scalable actuation using laminate fabrication approaches? The hypothesis is that if the uniaxially aligned LCE (i.e., accessible alignment method) is constrained with a rigid layer, it is possible to achieve and predict the reversible self-folding angle of the composite hinges. Until then, previous work has relied solely on the performance of actuators and did not demonstrate the feature of patternability or amenable system integration. The key contributions of this work are:

- A methodology to generate reversible self-folding composites hinges as well as the estimation of their folding angle using uniaxially aligned Liquid Crystal Elastomers (LCE) with a rapid laminate fabrication approach.

- The analysis and demonstration of the advantages and disadvantages of the hinges with a tensional design compared to a flexural design, and which performs more reliably with an uniaxially aligned LCE.

- The demonstration of the ability to electrically actuate small (2,5 cm) composite crawling robots with this design approach.

Chapter 3: Reversible actuation for self-folding modular machines using liquid crystal elastomer

This chapter address the question: how to design reversible self-folding machines (i.e., beyond a hinge) with a single layer of unidirectionally aligned LCE? The results of the previous chapter identified the type of hinge necessary to achieve reversible self-folding with an uniaxially aligned LCE. However, tensional designs pose significant challenges for amenable system integration for designs that require more than one hinge since they need at least one actuation per hinge. In this work, the hypothesis is that if a transmitting mechanism coupled with the tendon driven actuation of the LCE is used, it is possible to achieve reversible folding to more than one hinge with a single layer of LCE. The key contributions of this work are:

- A design approach to achieve reversible self-folding of complex origami-inspired shapes with a single actuation layer of LCE using a tensional design.

- The investigation of a mechanism to achieve biaxial, modular and reversible self-folding origami-inspired composites.

- The demonstration of the high-strength-to-weight ratio of our modular composite.

- The demonstration of the ability to achieve distributed actuation of a single layer of LCE for locomotion with a self-folding crawler with and without directional friction pads.

Chapter 4: Soft power amplification system for jumping using patternable artificial muscle and snap-through of shells

This chapter address the following challenge for soft robotic actuation: How to amplify the actuation of soft muscles (which tend to be relatively slow) to achieve rapid motion (like jumping)? The hypothesis is that a nonlinear elastic element could be used to amplify the power output of soft artificial muscles by storing energy slowly over time, to be later released quickly, if mediated with a latch that decouples the different time scale of responses between actuator and storing element. The key contributions of this work are:

- An approach to designing soft mechanisms using snap-through of shells for power amplification of jumpers actuated by a soft artificial muscle.
- A methodology to estimate the performance of the system (e.g., jumping height, power amplifcation) with a set of design parameters for the shell (e.g., radius, angle of curvature, thickness), actuator (e.g., geometry), and latching system.
- A new methodology to pattern and fabricate the LCE to achieve high-force.
- The demonstration of this methodology with a mesocale jumping robot.

Chapter 2

Reversible actuation of origami inspired composites using liquid crystal elastomers

2.1 Introduction

The need for devices with controllable physical properties (including shape) has inspired research towards smart composites. Smart composites consist of a heterogeneous combination of materials that can exhibit a desired function given an environmental stimuli (e.g., control of the composite shape or induction of internal stress and strain [19]). These composites contain smart materials, which are capable of controllably changing their properties and offer features beyond those provided from their individual constituents [20]. For instance, a smart composite may achieve improved properties and features such as improved actuation speed, tuned mechanical properties (e.g., stress and strain), as well as reduced actuation threshold (e.g., phase transition temperature) than compared to each constituent material of the composite [21].

Given the above advantages, previous work has explored the use of smart composites to achieve origami-inspired self-folding. For example, origami-inspired robots take advantage of a laminate manufacturing process that stacks patterned layers to enable automated folding

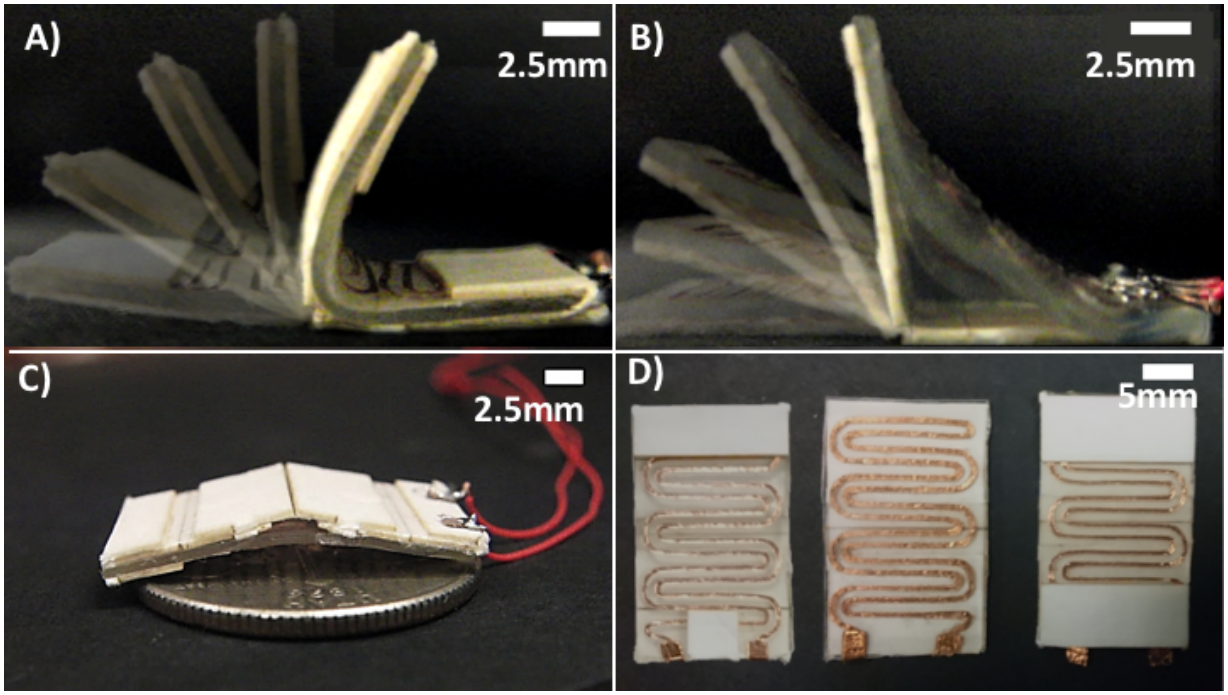

Figure 2.1: Liquid crystal elastomer (LCE) actuation for origami-inspired self-folding composite hinges. **A)** Folding motion of the flexural composite hinge. **B)** Folding range of the tensional composite hinge. **C)** Crawler smart composite robot on top of a quarter. **D)** Bottom view of the composite hinges, from left to right: crawler, tensional and flexural single fold composites showing the electrical heating layer (i.e., serpentine patterns).

through the activation of a smart material layer [22, 23, 24]. The self-folding process occurs when an stimulus, such as temperature, generated by an electrical heating layer, activates the smart material in the composite. This activation causes the smart material to contract and results in folding of the composite. Laminate manufacturing and the self-folding process enable these smart composites to transform from 2D to 3D configuration without an external force. These features allow for a scalable, lightweight, repeatable process, and depending on the constituent materials [25], an affordable manufacturing process for morphing structures. Given these advantages, laminate manufacturing and origami-inspired smart composites have been explored for assembly of structures [22], robots [25], and medical applications devices [8].

Previous work has examined different methods of generating self-folding mechanisms. The folding occurs using active layers that allow either unidirectional or bidirectional actuation.

The former can be considered to rapidly obtain the body of complex structures at different scales [25, 24], whereas if a self-contained, deployable and actuated morphing structure is of interest, then smart materials capable of reversible actuation for folding may be desired [26].

Reversible folding using smart composites has been demonstrated using pouch motors, dielectric elastomers actuators (DEAs), hydrogels and shape memory alloys (SMAs). Pouch motors (i.e., not technically smart materials but included for completeness) are flat layers patterned with chambers designed to generate folding when inflated [27]. These pouches operate as either a tensional layer [27], or flexural layer [28] capable of reversibly actuating a fold when inflated with a pressurized fluid [29]. Disadvantages of this actuation method include susceptibility to leaks, which can affect the performance and repeatability of the system, and scalability, since at least one (typically electromagnetic) pump or valve is required per actuated degree of freedom.

Dielectric Elastomers (DEs) are an alternative smart material for bidirectional self-folding. DEs are compliant capacitors, consisting of a soft dielectric layer coated with soft electrodes on both sides [30]. When a voltage is applied, electrostatic forces compress the dielectric film, which then expands in the perpendicular direction, due to the incompressibility of the dielectric layer. When both electrodes are brought to the same electric potential, the DE returns to its original shape, due to the elasticity of the composite. Depending on the geometry of the dielectric layer and electrodes, bending and folding can be obtained [31]. DEs have the advantage of obtaining large strain deformations (300%) and rapid actuation (i.e., 1 ms) but require high voltage (i.e., kilovolts), as compared to other smart materials. As the voltage is proportionally dependent on the thickness of the dielectric elastomer membrane, thin dielectric membranes are typically used to limit the required electric potentials. The challenge of a DE membrane is that if punctured, the actuator will short-circuit and no longer function, limiting the resilience of DE actuators.

Another class of smart materials that has been explored for bidirectional folding are hydrogels. Hydrogels are polymer networks with hydrophilic properties that swell in the presence of water. Furthermore, they can be designed to deswell upon application of an external stimuli

[32]. If sandwiched between patterned rigid layers, hydrogels can achieve reversible folding by increasing the hydrogel temperature [26]. The use of this material allows a scalable manufacturing process for small scale smart composites, and offer an alternative folding mechanism for applications in aqueous environments. Despite these factors, hydrogels need to be hydrated to operate properly, complicating their application in non-aqueous settings. Additionally, the time response of self-folding hydrogels is typically slow (e.g., 10 min to swell and 2 min to deswell) [26].

Shape Memory Alloys (SMAs, e.g., muscle wires) are smart materials that can change their shape due to thermal variations. This desired shape can be pre-defined through a process called training or memorization [33] in which the SMA is held in the desired shape and annealed for a few minutes at high temperature, then cooled. Subsequently, at temperatures below the phase transition temperature, (which is below the annealing temperature) the material can be easily deformed, but upon heating above phase transition temperature, the SMA recovers its initial shape. Given these properties, SMAs have been explored for reversible folding in origami inspired structures [34]. SMA wires have a contraction of $\approx 8\%$, which limits the range of folding angles unless trained into a more complex shape for actuation (i.e., linear and torsional spring). Although SMA foils exist [35], in general they are challenging to pattern or machine. Additionally, SMAs require high training temperatures (i.e., annealing temperature $\geq 300^{\circ}$C) to achieve the desired shape deformations [34, 35], which may be outside of the working range of other materials desired in an origami composite.

Unidirectional folding has been obtained using shape memory polymers (SMPs) to create origami inspired structures [5]. Similar to SMAs, shape memory polymers can change into a desired shape upon training. The polymer can deform its shape depending on the transition temperature (*Tt*). Below the *Tt* the polymer remains stiff (i.e., glassy state) and above it becomes soft (i.e., rubbery state) [13]. In this soft stage, the training of the SMP into the desired shape occurs through an external force capable of generating mechanical deformation [13, 36]. The

temporary shape is sustained upon cooling and removal of this external force until an external stimulus (e.g., temperature) resets the SMP to its original state [36]. This type of SMP is also known as having a one-way shape memory effect, which requires an external reshaping process to return to its original shape [33]. Previous origami inspired self-folding work has used this type of SMP (e.g., prestrained polystyrene or polyolefin) [22]. The interest of using SMPs comes from the fact that they can easily be fabricated as layers and are commercially available as sheets (e.g., shrink films). These characteristics make SMPs ideal active layers for smart composites fabricated by laminate manufacturing. Additionally, shape memory polymers offer good shape recoverability (100% recoverability for deformation up to four times its original length) and the ability to tailor their properties such as transition temperature and stiffening [36]. Previous work took advantage of these features and used mechanical design constraints to fold complex structures transformations from 2D to 3D through heating [5, 25].

Despite these advantages, the aforementioned SMPs (e.g., prestrained polystyrene or polyolefin) lack the ability to spontaneously return to their original shape when the activating stimulus is no longer applied. This disadvantage prevents the use of these SMPs to generate reversible self-folding and cyclic actuation. Alternative smart materials, however, feature a reversible memory effect without requiring an external force to switch between the temporary and original shapes [37]. Liquid crystal elastomers (LCEs) are an example of this type of reversible smart material with polymeric structure. Previous work has demonstrated the use of LCEs as artificial muscles [38], their ability to achieve reversible deformation, and tailorable processes for their manufacturing to generate mechanical responses such as bending and twisting [39].

In this work, we explore the use of LCE as the active layer in laminate manufactured shape memory composite capable of reversible actuation for folding and locomotion. We explore the performance of LCE in two configurations, one where it serves as a flexural actuator (composite design enables LCE bending), Fig.3.1A, and a second where it serves as a tensional actuator, (Fig.3.1 B). Using the induced bending configuration, we also demonstrate an inchworm-inspired

crawler, (Fig.3.1 C).

The remainder of this paper is divided in four sections: i) Liquid Crystal Elastomers, where we provide some background about LCEs and their fabrication; ii) LCE Actuated Hinge Design and Performance Results, where we describe the design and results of the flexural and tensional composite hinges as well as the performance of the composites regarding their respective blocked torque, reversibility, and we demonstrated the repeatability of the LCE with the actuation of a laminate crawler robot; iii) Discussion, where we discuss the folding angle performance between the two hinge designs and potential applications of the LCE for origami inspired smart composites; and iv) Conclusion and Future Work, where we summarize our results and describe the future directions of LCE for origami inspired smart composites.

2.2 Liquid Crystal Elastomers

Liquid crystal elastomers are polymer networks that exhibit both the self-organization of liquid crystals as well as the mechanical properties of elastomers [18]. The polymer chains of an LCE are composed of rod-like structures known as mesogens [40]. The polymer backbone connects the mesogens through covalent bonds (i.e., cross-links), forming polymer chains, see Fig.2.2. In this work, we use a uniaxially oriented LCE capable of changing between two different shapes [41]: when the temperature of the LCE is below its T_t (known as the nematic phase), the mesogens are uniformly aligned. Once a stimulus is applied that raises the temperature of the LCE past its T_t (isotropic phase), the anisotropic mesogens change their orientation and become disordered. This phase transition between nematic and isotripic generates a microscopic change to a macroscopic deformation of the LCE shape, (Fig.2.2). Apart from the uniaxial configuration, the LCE also offers interesting features such as the ability to tailor the orientation of the deformation for the desired application. For instance, recent work has utilized LCEs to obtain undulatory locomotion [42] as well as to generate three reversible shape stages and a

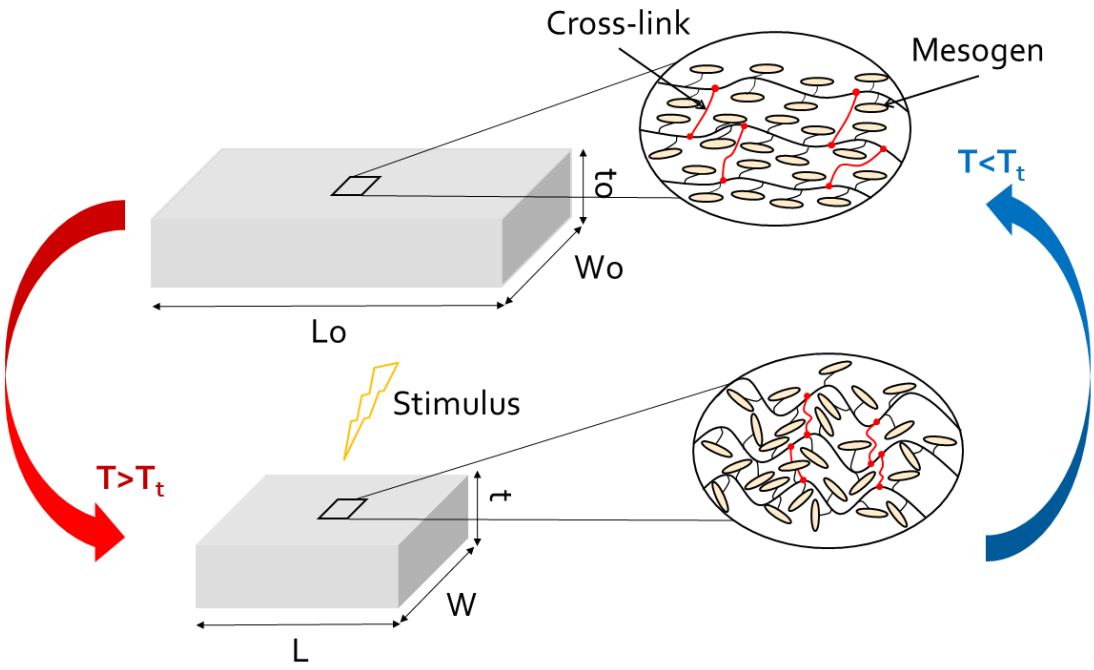

Figure 2.2: LCE behavior in the nematic and isotropic phase. The LCE uniaxially contracts when heated (i.e., stimuli) to a temperature higher than its phase transition temperature (i.e., $T \geq T_t$) changing from the nematic to isotropic phase. Once the stimuli ceases (i.e., $T \leq T_t$), the LCE returns to its original shape.

Miura pattern folding by changing the orientation of the LCE directors [43] using an optical patterning system. Other work used topology optimization to achieve LCE folding by optimizing the director pattern for a specified shape using twisted nematic hinges [44].The last two articles patterned the LCE by aligning complex directors profiles for folding, however at a cost of a more intricate fabrication process, and relatively high phase transition temperature (i.e., 100°C) [43]. Alternatively, another LCE fabrication process utilizes a simpler two-step crosslinking reaction method, and straightforward steps to pattern the LCE directors (by stretching) resulting in a relatively smaller LCE phase transition temperature (i.e., 80°C) [45, 41, 46].

2.2.1 LCE fabrication

In this work, we used a uniaxial LCE fabricated with the method described in previous work [45, 41, 46]. The preparation of the LCE required two cross-linking steps. The first step used 10 g of 1,4-bis-[4-(3-acryloyloxypropyloxy) benzyloxy]-2-methylbenzene (RM257, Wilshire company, 95%) dissolved in 3.1 g toluene and the mixture was placed in 85°C for 20 minutes. Then, 0.0642 g (2-hydroxyethoxy)-2-methylpropiophenone (HHMP, Sigma-Aldrich, 95%) used as crosslinker was added into the mixture and heated to 85°C in the oven. 2.26 g 2,2'-(ethylenedioxy) diethanethiol (EDDET, Sigma-Aldrich,95%), the spacer in LCE, and the tetra-arm thiol crosslinker, 0.58 g pentaerythritol tetrakis (3-mercaptopropionate)(PETMP, Sigma-Aldrich, 95%) were added to the mixture. After that, 0.0284 g dipropylamine (DPA, Sigma-Aldrich, 98%), the catalyst, was added into the mixture. Next, we stirred and degassed the mixture in the vacuum chamber to remove bubbles. Then, the mixture was poured into a rectangular mold (70 mm x 50 mm x 1 mm). After 24 hours of chemical reaction at room temperature, we removed the glass slide and put the sample into the oven to evaporate the solvent (toluene) for 12 , finishing the first step of the cross-linking of the LCE. Next, for the second step (aligning the LCE director), the crosslinked LCE film was stretched (pre-strain = 100%) by external force and exposed to UV irradiation for 30 minutes. After this second crosslinking step, the LCE film was ready to be integrated into the fabrication process of the hinges.

2.3 LCE Actuated Hinge Design And Performance Results

In this section we present the design, modeling, fabrication and results of the two hinges composites that we denominate as flexural and tensional, as well as the LCE performance for reversible folding, blocked torque and actuation of an inch-worm robotic crawler.

2.3.1 Flexural Composite Hinge Design Model

We propose a preliminary design based on the fabrication of laminate composites [5]. Our design is composed of six layers: rigid, adhesive, actuator (LCE), flexible, and rigid, the LCE (Figure 2.3A). The composite folds when the LCE uniaxially contracts (Figure 2.3B).

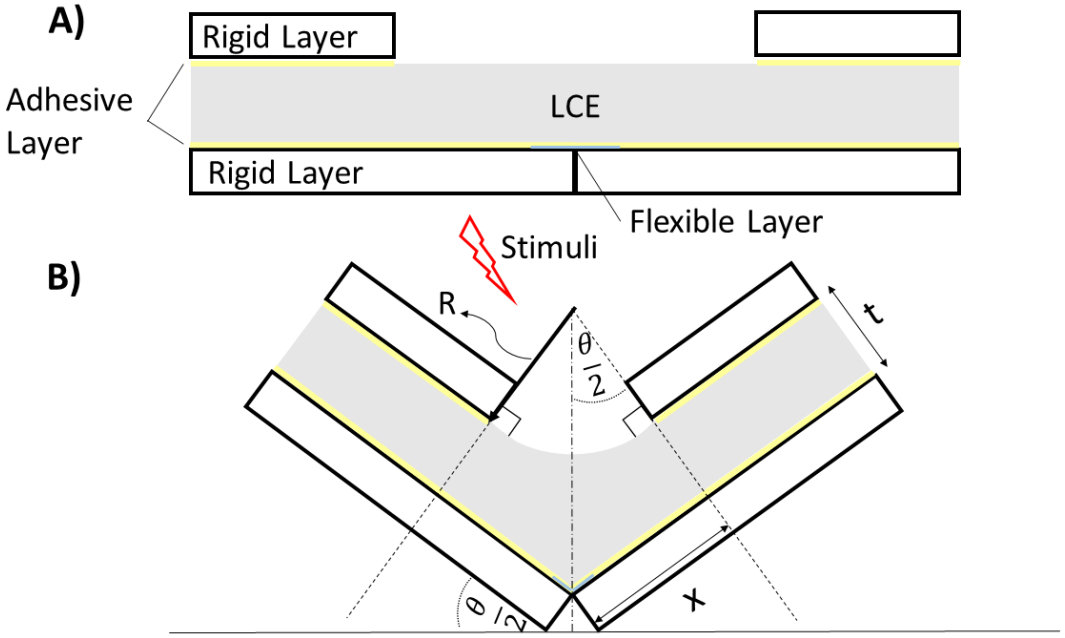

Figure 2.3: Proposed design for a flexural single hinge smart composite design. **A)** The composite is composed of two rigid layers, two adhesive layers and one consisting of a smart material layer, in this case, the LCE. **B)** Upon the application of a stimuli (applied heat) the LCE contracts inducing folding and its respective folding angle.

The composite starts to bend and fold in the direction of the gap in the top layer, where the LCE is not constrained by the other layers. The folding angle of the composite hinge depends on the strain which is a function of the temperature ($\varepsilon = f(T)$)). To model the flexural hinge composite design, we made the following assumptions: i) the folding of the composite is symmetric about the hinge, ii) the rigid layer is much stiffer than the LCE, iii) the LCE deforms as an arc without delaminating from the rigid layer and iv) heating of the LCE is uniform. Considering these assumptions, and knowing that $\varepsilon(T) = \alpha(T)$ (i.e., α is the coefficient of thermal

expansion, which is negative), we can find the geometric relationships described in Eqn. 2.1-2.4, see (Fig. 2.3):

$$X\,(1-\varepsilon(T)) = R\frac{\theta}{2} \tag{2.1}$$

Here, X represents the distance along the right layer between the hinge and the point at which the arc is tangent to the upper layer, Fig.(2.3A), R is the radius of the arc length formed upon the LCE bending, θ represents the folding angle of the smart composite, and t the combined thickness of the LCE and adhesive layers. From trigonometry, and assuming the bottom layer of the LCE is constrained by the adhesive layer (i.e., constant X), we observe that:

$$\frac{X}{R+t} = \tan\left(\frac{\theta}{2}\right) \tag{2.2}$$

For thin LCE layers (i.e., $X \gg t$), we assume that the thickness is negligible (i.e., $t \ll R$), and we can reduce Eqn. 2.2 to:

$$\frac{X}{R} = \tan\left(\frac{\theta}{2}\right) \tag{2.3}$$

Solving for R and substituting Eqn. (2.3) into Eqn. (2.1) we see that:

$$(1-\varepsilon(T)) = \frac{\theta}{2}\cot\left(\frac{\theta}{2}\right) \tag{2.4}$$

Substituting the first three terms of the Taylor series expansion of the cotangent into Eqn. (2.4), we can find the following relationship between the folding angle and temperature for the flexural hinge composite design with one physically possible solution (Eqn. 2.5):

$$\theta = \sqrt{\left(-30(1-\sqrt{(1+0.8\varepsilon(T))})\right)} \tag{2.5}$$

2.3.2 Characterizing LCE vs Temperature

To use our model, we require the relationship for strain as a function of temperature, $\varepsilon(T)$ (for a more elaborate LCE characterization, please see chapter three section *Results and Discussion*). We obtained this function by measuring the contraction and corresponding temperature of LCE on a hot plate (Fig.2.4). We measured the temperature, once the value stabilized (i.e., $\pm$

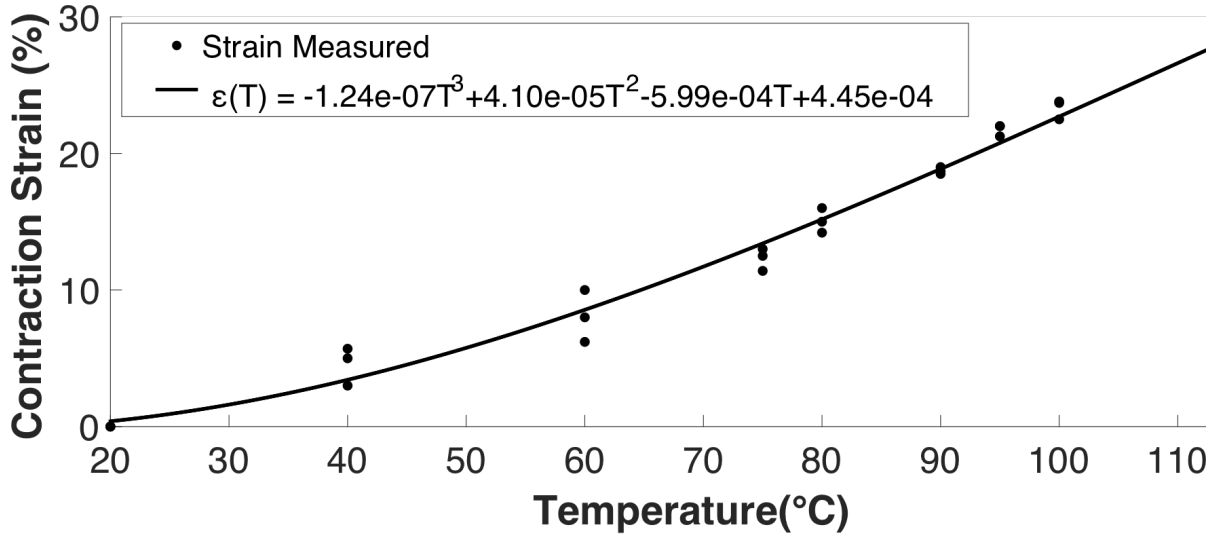

Figure 2.4: Experimentally measured strain-temperature relationship. We recorded the strain of three unconstrained LCE films during heating and fit the results to a 3rd order polynomial.

2 °C), using a thermocouple attached to the surface of the LCE. This procedure was repeated for three LCE samples from different manufacturing batches. The resulting data was then plotted and fitted with a third order polynomial using a least square curve fit. The phase transition temperature range of the LCE (i.e., 70 °C to 80 °C, [45]), is apparent in the measured data (Fig. 2.4), and can be seen in the increase in the slope of the fit curve.

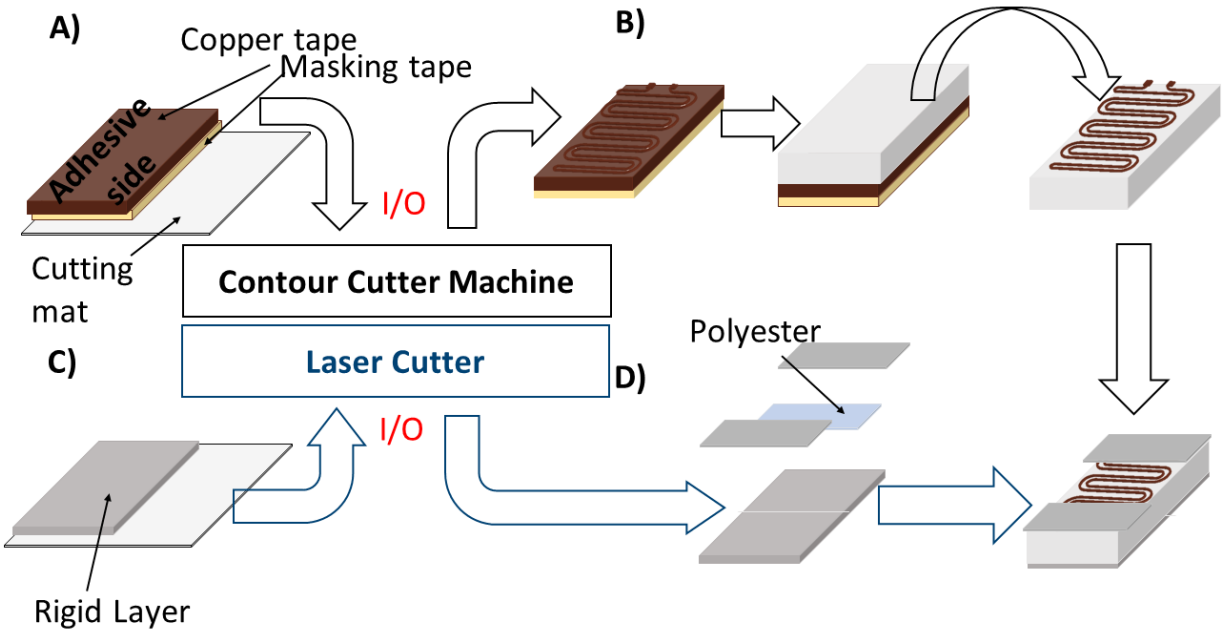

Figure 2.5: Fabrication process of the self-folding hinge composite. **A)** Insertion of the raw material (i.e., copper tape attached to the masking tape and cutting mat) into the contour cutter. **B)** Transfer of the output of the contour machine, the serpentine pattern cut on the copper tape, to LCE layer. **C)** Laser cut patterned rigid layers parallel fabrication. **D)** Assembly of the stacked layers as proposed in the model (Fig.2.3).

2.3.3 Single Hinge Folding Actuator Fabrication

We fabricated a single hinge flexural actuator (25 mm x 15 mm), (Fig.2.5), using a laminate manufacturing process [25, 5] (Fig.2.6A). The two rigid layers, and their thickness, (watercolor paper, 0.5 mm), adhesive layers (silicone tape, 0.05 mm), transferring tape (crepe paper masking tape, 0.2 mm) and the flexible layer (polyester film, 0.04 mm) are patterned using a laser machining system (Fig.2.5C). For expediency, we cut the LCE samples we tested manually with a blade, but it is also possible to laser cut them. We next laminated the Joule heating layer onto the LCE (Fig.2.6). For cyclic actuation of the LCE, this heater is subject to the two competing objectives of providing uniform heating across the layer, while providing minimal mechanical resistance to strain. We addressed these objectives with a layer of copper tape cut into a serpentine pattern using a contour cutting machine (Silhouete Cameo), (Fig.2.5A). We then

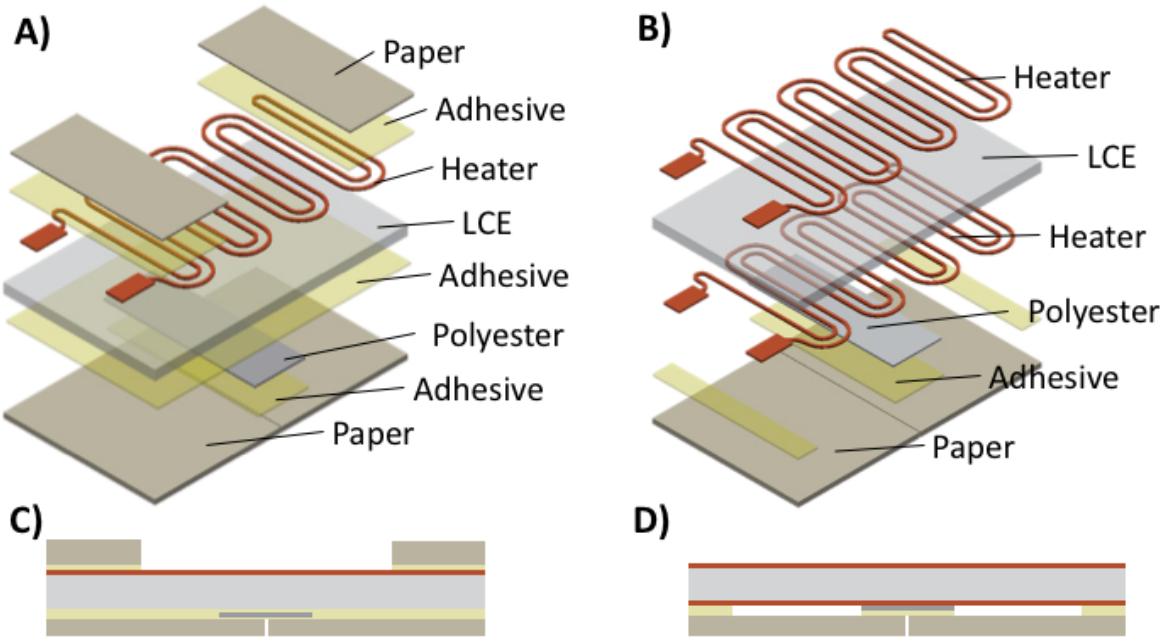

Figure 2.6: Assembly of the layers for the flexural and tensional composite hinges. **A)** Flexural layers aligned and assembled after the fabrication process shown in Fig.2.5**B**. Tensional layers aligned and assembled after the fabrication process shown in Fig.2.5. **C)** Side view of the flexural hinge showing the layers assembled. **D)** Side view of the tensional hinge showing the layers assembled.

stamped the LCE layer (0.7 mm thick) onto the copper tape (Tape Master, 0.06 mm). A little pressure was applied to transfer only the released electrical traces. We subsequently removed the LCE from the remaining carrier copper tape, leaving only the serpentine pattern of the copper on the LCE, (Fig.2.5B). In the final fabrication step, the LCE and its heating layers were incorporated with the other layers previously patterned using the laser cutter (Fig.2.5D).

2.3.4 Flexural LCE hinge composite results

In this section we test our flexural hinge composite and check the experimental results with our model proposed previously. In the flexural hinge experiment, we fixed one side of the prototype and allowed the other side of the hinge to rotate freely. We measured the temperatures using a thermocouple and proceeded to heat the LCE (i.e., 2.8 W) using a power supply (Fig.2.7).

Observing the images of the flexural hinge prototype and the plot, we can see an increasing discrepancy between the model and measured data at 40°. This difference may be due to the delamination observed during the experiment, (Fig.2.7). In the experiment, the delamination between the paper and the flexible layer on the hinge, became evident at an angle of approximately 40° and increased until it reached approximately 125°. At this angle, we also observed additional delamination, between the copper tape and the LCE. This secondary detachment may be due to the maximum recommended adherence temperature tested (i.e., rated to be -20°C to 120°C). These results violate our assumption of perfect adhesion between the flexural LCE layer and the structural and heater layers. Another explanation for the discrepancy in the results may be our assumption of negligible LCE thickness.

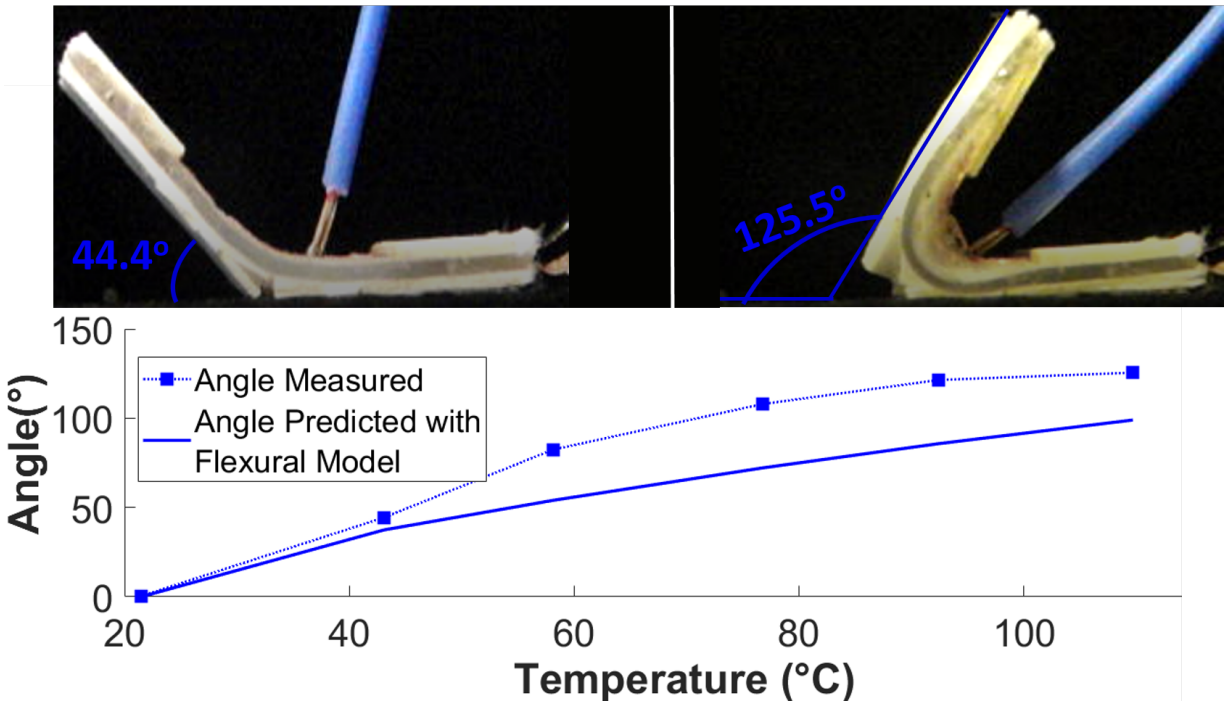

Figure 2.7: Angle vs temperature plot demonstrating the performance of the folding angle model for the flexural single hinge compared to the values measured experimentally. At 40° the delamination between the rigid layer is visible and it propagates until the maximum angle measured at 125°. At this maximum angle the corresponding temperature is 109.7°C and some delamination between the copper tape and LCE occurs.

2.3.5 Tensional LCE hinge composite design

Aiming to explore different ways to incorporate LCE as an actuator on laminates, we decided to test an alternative design that uses the LCE as a tensional layer, similar to a cable tendon or muscle, where we assume uniform uniaxial stress and no bending in the LCE layer. Instead of constraining the LCE on the hinge, we affix it to the rigid layer a distance L away from the hinge, (Fig.2.8). In this tensional hinge design, the LCE contracts uniaxially upon application of heat, resulting in folding of the composite. We developed a second model for the folding of this composite hinge as a function of LCE contraction. This model has the same assumptions as

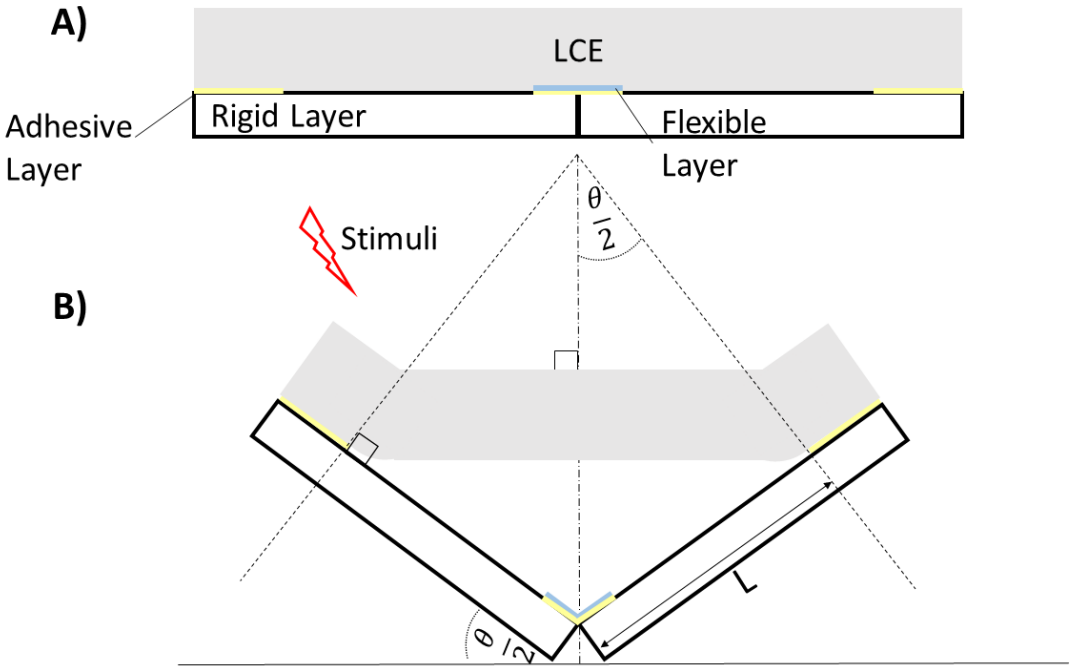

Figure 2.8: Proposed design for a tensional smart composite hinge. **A)** The composite is composed of 1 rigid layer, 2 adhesive layers, 1 flexible layer and the LCE. **B)** Upon heat application the LCE contracts inducing folding.

the previously proposed flexural model with the exception that we assume a tensional behaviour of the LCE given the composite design constrains. The LCE is attached only on the edges of the rigid layer. Similar to the flexural design, we use a geometric analysis to find the relationship

between LCE strain and the resulting angle of the composite hinge (Eqn. 2.7).

$$(1-\varepsilon(T)) = \cos\left(\frac{\theta}{2}\right) \tag{2.6}$$

Solving for θ we find the following relationship:

$$\theta = 2\cos^{-1}(1-\varepsilon(T)) \tag{2.7}$$

2.3.6 Fabrication of the Tensional Hinge Composite

We fabricated the tensional hinge composite following a process similar to the one described previously for the flexural hinge composite (Fig.2.5). The design follows the hinge design proposed in the previous section *Tensional LCE hinge composite design* for the LCE as a tensional case (Fig.2.8A). The layers consisted of a single rigid layer (watercolor paper board), a flexible layer (polyester) functioning as the hinge joint, and adhesive layer (silicone tape). In this design, we control the contraction of the LCE using an electrical heating circuit (i.e., copper tape) on both sides to guarantee uniaxial contraction (Fig.2.6B). We only constrained the LCE on the edge of the rigid layer (silicone adhesive), Fig.2.8.

2.3.7 Experimental Characterization of Tensional Composite

As for the tensional hinge design, we measured the folding angle as function of temperature and compared it against the model presented above, using the same strain values from the fitted curve we found previously, Fig.2.4. In this case, these angles predicted by the model showed close agreement with the experimental angles (Fig.2.9). We observed the largest deviation from the model between 55° and 75.5°. These variations may likely be due to the temperature variation on the LCE surfaces (i.e., the different convection between its surface, top surface can exchange temperature variation directly with the environment, whereas the bottom surface has the gap

between itself and the rigid layer of the composite). At 75.5° some warping was visible on the LCE layer and at 108.5 °C with an angle of 87°, warping and some delamination of the copper tape heating layer was visible.

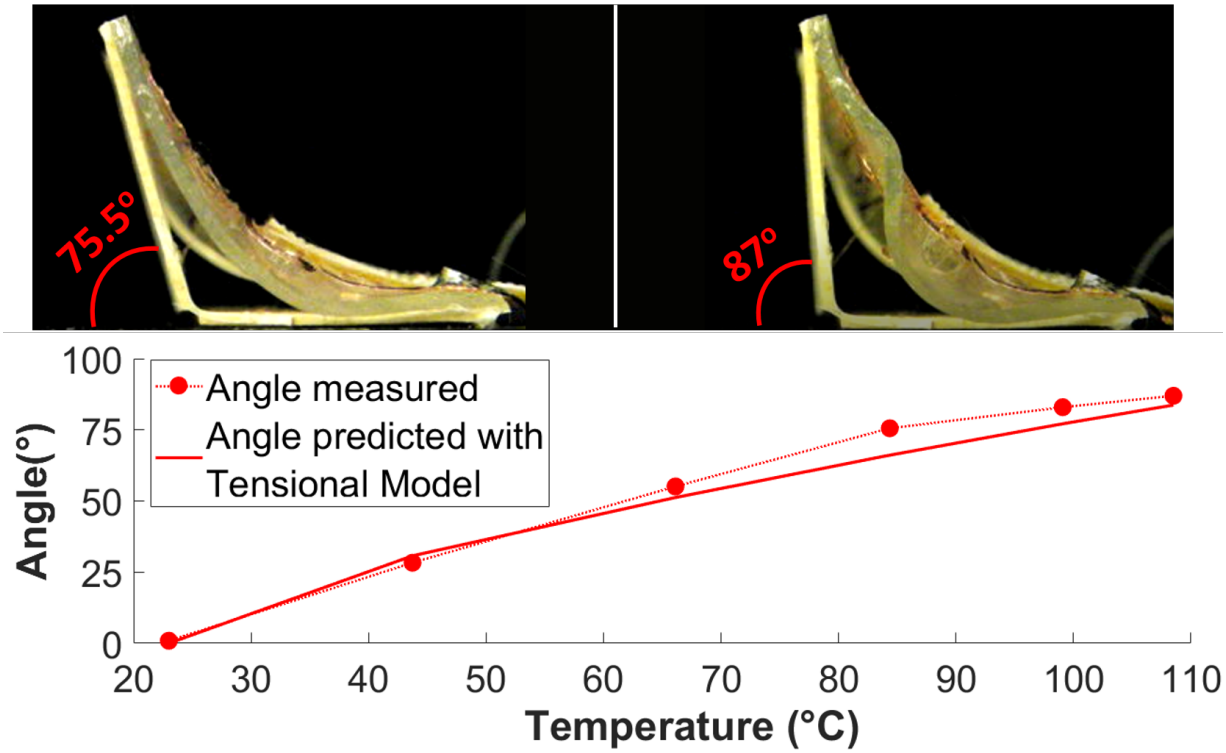

Figure 2.9: Angle vs temperature plot demonstrating the performance of the folding angle model for the tensional single hinge compared to the values measured experimentally.

2.3.8 LCE Performance for Single Hinge Composites

Regarding the performance of the LCE as an actuator, we verified the hinges reversibility as well as performed a blocked torque test, and demonstrated LCE repeatability through a laminate crawler. Based on the range of the angles achieved by both designs (i.e., flexural and tensional composites), we observed that in the flexural case, the LCE is capable of folding up to 125° at 110 °C from an initial flat state. For the same power (2.8 W) at approximately the same temperature (i.e., 109 °C), the LCE used as a tensional layer generated a folding angle of 84°

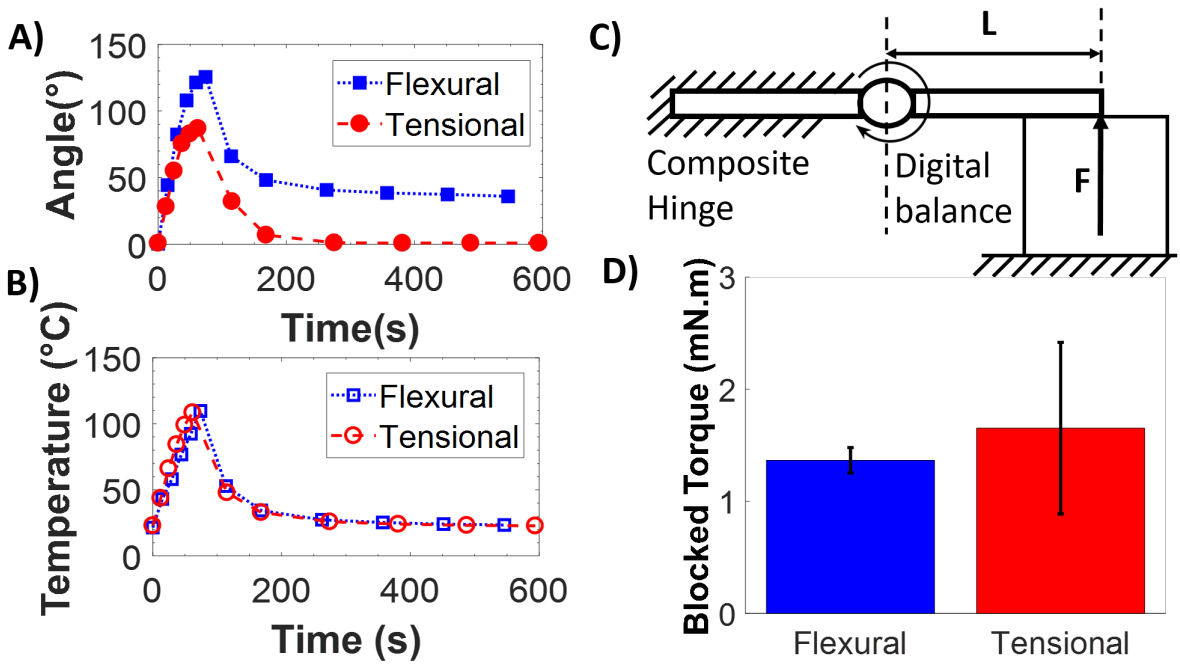

Figure 2.10: Angle and temperature change with respect to time of composite hinges and blocked torque results. **A)** The tensional design reaches a higher angle value (≈ 125°) during 102 s, but did not fully return to its original flat state. On the other hand, the flexural hinge design fully recovered its flat state, but was not able to reach higher angle values (i.e.,≈ 87° during 68 s). **B)** The tensional and flexural hinge designs folded at 110 °C and 109 °C, respectively, from approximately the same room temperature. In both hinge designs, the samples cooled back to values close to its original room temperature. **C)** Schematic of the blocked torque experimental setup. F is the reaction force measured from the balance and L the arm length. **D)** Average blocked torque bar graph of the flexural (at 86 °C) and tensional (at 70°C) composite hinges at 0°.

(Fig.2.10). These results are expected given the mechanical advantage of each design. In the flexural case, the smart composite hinge demonstrated some hysteresis in the fold angle which may be due to the material used as a rigid layer (i.e., at certain angle ranges and temperatures the paper appeared to deform plastically). For the tensional case, the folding was fully reversible after the actuation ceased, (Fig.2.10), despite a smaller angle range compared to the flexural hinge design, and some small slip between the LCE and adhesive layer causing LCE warp slightly upwards during cooling.

In this work, we also made some preliminary measurements of the blocked toque at 0°, but further investigation for the full range of motion is necessary. The experiment consisted on

fixing one side of the hinge while the other is touching a digital balance, which we obtained the reaction force (F) and calculated the blocked torque upon multiplication of the arm length (L).For each composite hinge design we tested at least two different samples and took four measurements using the experimental setup, Fig.2.10C, to compute the average blocked torque. For the flexural hinge composite we used L = 5.5 mm but for the tensional composite we tested L = 5.5 mm and 7.5 mm, in an attempt to decrease the friction between the contact area of the hinge and balance. The blocked torque test for the flexural hinge composite demonstrated an average value of 1.4 mN·m ($\pm$ 0.1) at $\approx 86^{\circ}$C, whereas the tensional hinge composite had 1.7 mN·m ($\pm$ 0.7) at $\approx 70^{\circ}$C, (Fig.2.10D). The safest temperatures (i.e., no delamination between LCE and rigid layer) observed for blocked torque actuation for flexural and tensional hinge design composites were at $\sim 85^{\circ}$C and $\sim 70^{\circ}$C, respectively. Despite these initial challenges, the blocked torque measured at 0° seemed comparable with previous work blocked torque measurements of laminate robots using SMAs as an actuation layer [35].

2.3.9 Crawler Demonstration

We also demonstrated the use of LCE as a periodic actuator for origami inspired robots with an inch-worm crawler. The crawler motion is a friction based locomotion and for one degree of freedom both asymmetric friction and actuation strokes are necessary to generate net displacement [47]. The crawler, Fig.2.11, was made utilizing the same manufacturing procedure (Fig.2.5) to produce the single hinge laminate designs. The crawler consisted of 10 layers (i.e., rigid, flexible, LCE, electrical heating, and adhesive) aligned and stacked together (Fig.2.11A). By design, the bottom layer (rigid) of the crawler has asymmetric pattern, which enables an asymmetric friction with respect to the body of the crawler (Fig.2.11B). The LCE, in this case, has the electrical heating layer attached only on the bottom surface of the LCE (Fig.2.11C). When current passes through the serpentine pattern, the LCE starts to bend and enables the folding of the structure. By controlling the rate of the power stroke (power supply on, 30 s) and the relaxation

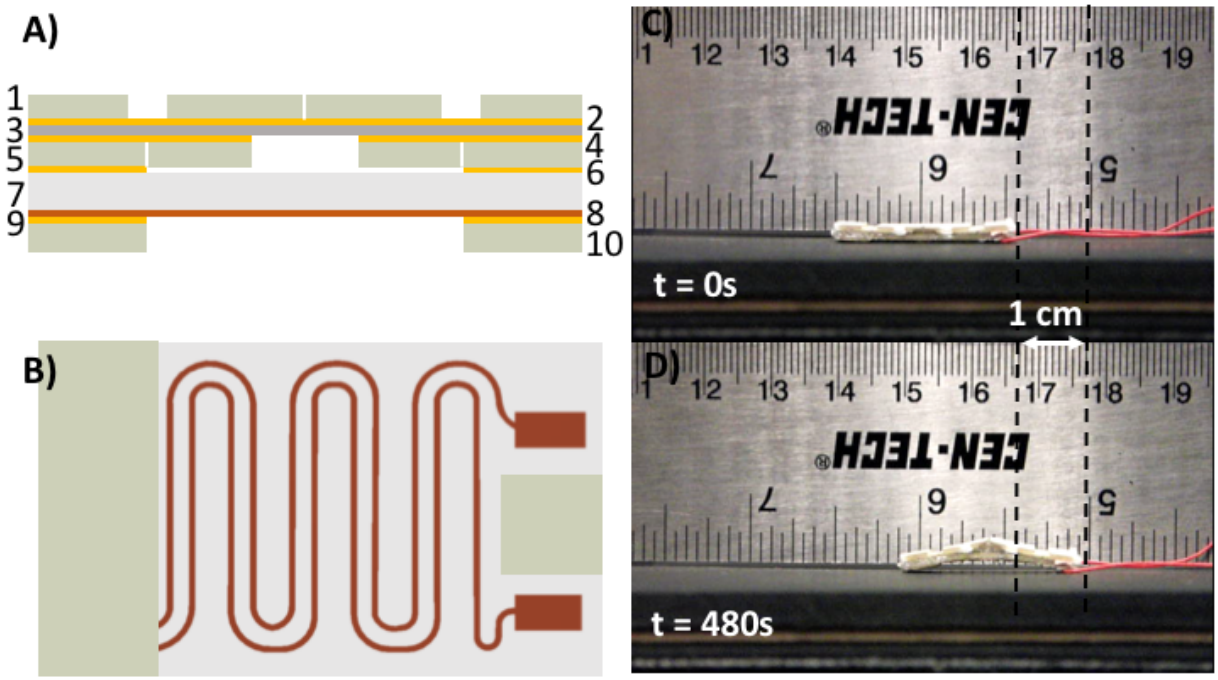

Figure 2.11: Crawler design and locomotion upon actuation of the LCE. **A)** The crawler layers: top bottom rigid layer of the flexible hinge (1,5), Adhesive (2,4,6,9), Flexible (3), LCE (7), heating circuit (8), Bottom rigid layers with asymmetric surface area (10). **B)** Bottom view of the crawler showing the asymmetry of the two bottom layers for locomotion. **C)** The initial state of the laminate crawler (i.e., 25 mm x 15 mm). **D)** Final state of the crawler at the end of 6 cycles: 5 with cyclic actuation (i.e., 30 s of actuation and 60 s of relaxation) and 30 s used to obtain its relaxed state for the last cycle.

stroke (power supply off, 60 s) of the LCE, we are able to generate an asymmetric motion. The overall net displacement measured was of 10 mm during 6 cycles with an average speed of 1.25 mm/min (Fig.2.11D). It also is interesting to note that during this cyclic actuation the LCE does not fully recover to its original shape. This is due to the cooling time used during the relaxation strokes, which is happening through convection in a stable environment (i.e., relatively constant temperature), and was not enough to allow the LCE to fully recover its original shape (Fig.2.11D). Faster actuation cycles and unidirectional friction pads could also improve the net displacement.

2.4 Discussion

Based on the previous models and experiments, we observed that the model of the LCE as a tensional layer better predicted the experimentally measured angles (Fig.2.9) compared to the flexural layer case for a single hinge (Fig.2.7). These results suggest that the model of LCE as a tensional layer for folding is sufficient to predict the resulting fold angle. However, for the case where the LCE acts as a flexural layer, the impact of ignoring delamination between the rigid and flexible layers as well as the of the LCE layer greatly affect the prediction of the folding angle.

Overall both composite folding designs provided a bidirectional hinge actuator that could be used to fold complex origami patterns and potentially actuated folded designs to achieve lightweight origami inspired robots. The use of laminate manufacturing also enables a flexible design process since it allows the designer to tune mechanical properties for specific applications such as aerospace, robotics or medical devices. In this case, the smart composite hinge designs were made of affordable materials (e.g., watercolor paper and copper tape) using a scalable (in size and number) fabrication process.

It is also important to highlight that our manufacturing process applied a similar method from previous work [25], which used a bidirectional SMP and thus did not explore reversible folding. The main challenge we faced was trying to avoid delamination between the laminate layers. For instance, we utilized the watercolor paper as a rigid layer, but this assumption of rigidity proved inaccurate once the paper began to delaminate and deform. The copper tape heating layer offered an affordable, easily replaceable (i.e., compared to embedding the heater into the LCE [38]), and simple manufacturing solution. We were able to achieve a extensional heating layer, however, given the heater maximum temperature tolerance (i.e., $\leq$ 120 °C), the adhesion of copper tape at high temperatures may have limited the full range of folding that the LCE could achieve (due to the detachment between LCE and heater). The silicone tape also offered high temperature tolerance, but better adhesion could improve the performance of both

hinges (flexural and tensional).

These results provide insights for potential applications of the LCE as a smart actuator for laminate designs. Some applications, such as origami inspired structures, may take advantage of the LCE flexural design to obtain a reversible folding as well as a larger angle range and faster activation response than previous work using SMP. Additionally, flexural designs may be desirable for applications where self-contained structures are required such as in medical applications [8]. On the other hand, the tensional hinge design provides a simpler design (i.e., less layers) and folding angle model that could potentially be used to design tensional actuators for bioinspired locomotion mechanisms using laminate manufacturing.

2.5 Conclusions and Future Work

We presented two smart composite designs for folding, where the LCE acted as a controlled actuation layer upon joule heating (i.e., an extensible layer created using copper tape). The LCE as flexural layer demonstrated a better range of folding angles and time response, higher than previously reported using undirectional SMPs [5, 22], but assumptions such as delamination and the LCE thickness should be considered to obtain a more predictable folding angle model.The LCE as tensional layer had a simpler and predictable model for the folding angle, which was independent of the middle gap length between its layer constraints (Fig.2.8). Both designs demonstrated reversible actuation, despite the flexural design's hysteresis during its relaxation stroke.This capability aligns with the advantages of previous SMPs used for self-folding laminates (e.g., high strain, tunable mechanical properties and patternable for manufacturing) but with the bidirectional feature. In future work we aim to improve the hinge designs using LCE to generate more complex origami inspired self-folding composites.

Chapter 2, contains material as it appears in **Minori, A**., Jadhav, S., He, Q., Cai, S., & Tolley, M. T. (2017, September). Reversible actuation of origami inspired composites using liquid

crystal elastomers. In Smart Materials, Adaptive Structures and Intelligent Systems (Vol. 58257, p. V001T08A015). American Society of Mechanical Engineers.The dissertation author was the primary investigator and author of this paper.

Chapter 3

Reversible actuation for self-folding modular machines using liquid crystal elastomer

3.1 Introduction

Organisms can morph their bodies for locomotion, and to adapt to their environments. For instance, ladybugs control the folding of their wings for locomotion [1], and pine cones can fold and unfold depending on the humidity of the environment to control seed dispersion [48]. Recent work has used origami-inspired designs to similarly produce deployable, compact, and lightweight morphing structures [3]. For instance, previous self-folding robots could crawl [25], potentially deliver drugs for medical applications [8], and adapt to constrained environments for locomotion [7]. However, it is challenging to obtain actuation for self-folding machines that is reversible, patternable, and made with a scalable manufacturing process.

Previous work has used motorized actuation such as direct current motors (DC) or fluidic pumps [29], and smart materials such as dielectric elastomer actuators (DEAs) [49], shape

memory alloy (SMAs) [50, 35], shape memory polymer (SMP) [25, 22] for self-folding and actuation of origami inspired robots. Motorized and fluidic actuation methods have the advantage of being repeatable and reversible, but are not generally lightweight, deformable, or low-profile which limits their applicability for constrained environments. Also, the realization of designs with many, highly packed motors requires complex assembly, and fluidic systems have the potential to leak.

Smart material actuators, on the other hand, have advantages and disadvantages that depend on whether the structure is composed solely of an active layer (i.e., smart material), or combined with another layer (e.g., for structural support and sensing). In general, for self-folding actuation, polymers with One Way Shape Memory Effect (OWSME) and Two Way Shape Memory Effect (TWSME) have been used.

OWSME polymers have tunable properties (e.g., deformation and transition temperature), and are patternable (can be cut programmably with a laser or blade), but are not reversible once the stimulus ceases [36, 13]. By contrast, TWSME polymers share the advantages of OWSME polymers, but they return reversibly to their initial state once the stimulus ceases [13]. For instance, liquid crystal elastomer (LCE) is a TWSME polymer. LCEs have the self-organization of liquid crystals and the mechanical properties of elastomers, providing tunable deformations depending on the alignment of its directors (mesogens) [18].

There are different ways to align the LCE deformation, including magnetic or electric fields [51], surface alignment [43], and mechanical alignment [45]. The two methods that have been most explored are the surface and mechanical alignment methods. The surface alignment method provides thin (i.e., $\leq 100\ \mu$m) LCE layers as well as complex mesogen orientation, but at the cost of more complex fabrication methods [52, 45]. For example, previous work demonstrated intricate self-folding shapes of origami inspired LCE [43] in which they built a machine to generate programmable deformation of the LCE. Alternatively, the mechanical alignment method provides a straightforward alignment process, by unidirectionally aligning the mesogens by

stretching [45]. However, it is challenging to generate complex mesogen orientation using this method. Previous work also demonstrated 3D printed LCE shapes capable of reversible folding [53, 54, 55, 56]. While 3D printing provides customization, it also leads to long fabrication times and costly manufacturing processes.

In both the OWSME and TWSME cases, a single soft layer lacks the strength to carry loads that are typically necessary for robotics applications. Also, unconstrained deformation limits precision. Previous work has addressed these challenges using smart composites, combining passive layers with smart materials to generate self-folding machines [25]. However, the choice of material layer for actuation results in unique advantages and disadvantages. For instance, shape memory alloy (SMA) and magnetic actuation are repeatable and lightweight, but SMAs are challenging to pattern and both SMAs and magnetic actuation exhibit hysteresis [57, 58]; dielectric elastomer actuators (DEAs) are repeatable and lightweight but require large voltages for actuation [31], which may be a limiting factor for applications that require compact circuitry; SMPs used in previous work have large transformation strains (50%) [36], which is generally desirable for folding [59], and are easy to pattern, but they are not reversible once the stimulus ceases and require retraining.

Previous work with LCE as the smart material for smart composites used a unidirectional LCE embedded into 3D printed layers to achieve self-folding origami-inspired shapes [60], but each crease required an LCE sheet for actuation. Another work also demonstrated a printed LCE composite [61]. Despite these advances in using a 3D printer to enable shape customization, as previously highlighted, it also leads to long fabrication times and costly manufacturing process. Additionally, the aforementioned work did not explore the repeatable actuation of these printed composites. In initial work to generate reversible self-folding composites [62], we embedded mechanically aligned LCE sheets into a composite hinge made using a rapid laminate fabrication method [22]. However, this work focused on isolated hinges and investigated the challenges of using a thermoactivated material sandwiched between rigid layers for reversible folding through

a bending and tendon-driven motions. Recent work has also explored the combination of liquid metal with LCE to enhance its actuation and material properties, but at the cost of a more intricate LCE synthesis [17].

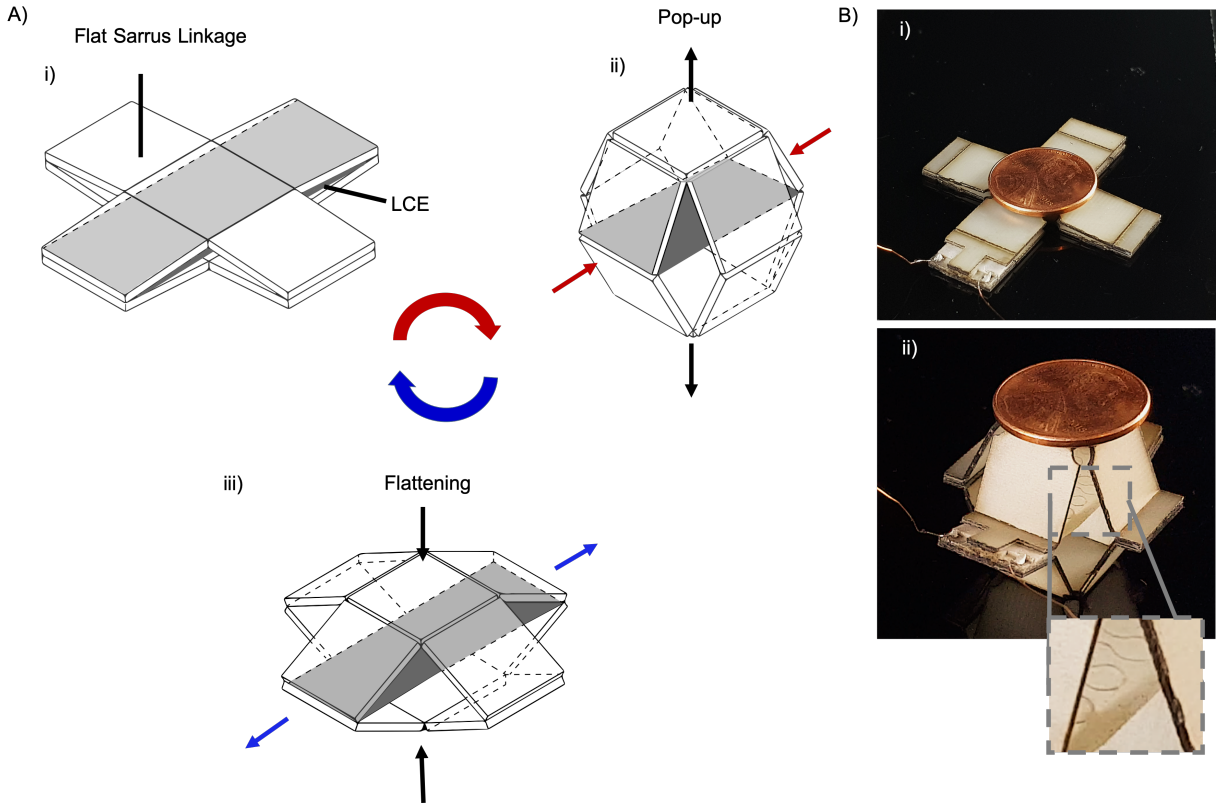

Figure 3.1: Reversible self-folding of the Sarrus linkage mechanism with a LCE actuator, where the red and blue arrows indicate the heating and cooling states of the LCE, respectively. A) Concept of the reversible self-folding of a Sarrus module with an embedded LCE actuator. i) Flat state of the Sarrus module. ii) The pop-up state of the Sarrus module when the LCE is Joule heated, where the arrows indicate the direction of the Sarrus movement. iii) The Sarrus module reversibly folding back to its flat state when the LCE actuator is cooling down, where the arrows indicate the direction of the Sarrus movement. B) Laminate Sarrus module. i) Flat state of the Sarrus carrying a penny to demonstrate its scale size. ii) Folded state of the Sarrus module when the LCE is active through the heating of an embedded resistive layer.

In this work, we propose LCE actuators composed of uniaxially pre-stretched LCE and stretchable electrical heater layers to achieve tendon-driven actuation of laminate mechanisms. Using this approach, we generate: patternable actuation (in the geometry), lightweight, reversible (returns spontaneously to the initial configuration) self-folding modules using a Sarrus linkage

mechanism, (Figure 3.1A). The Sarrus linkage is a mechanism that can convert limited circular to linear motion and vice-versa. It consists of at least four linkages connected to plates that are constrained to be parallel. These constraints enable biaxial folding with unidirectional actuation, and with only one degree of freedom allows pop-up designs of origami-inspired patterns such as a crane and a lily (Figure A.6A-B). When activated by a contractile layer, a Sarrus module can provide variable mechanical advantage. Using the LCE actuator as the contractile layer, allows the Sarrus module to lift and carry 13 and 38 times its own weight, respectively. Additionally, we demonstrate the sequential actuation of sections of a single LCE layer to induce a traveling wave behavior and locomotion of a crawler made of Sarrus modules with and without directional friction pads, and present as a simplified model for the crawler locomotion with anisotropic friction.

3.2 Methods

3.2.1 Design of Self-Folding Composites with LCE

We chose LCE as our actuator for our self-folding composite designs given its high recoverable strain [51], tunability [46], specific work [53], potential for patternability, actuation repeatability [63] and TWSME [13]. The reversibility of the LCE occurs due to the orientation of the mesogens during the nematic and isotropic states of the material. Once a stimulus causes the temperature of the LCE to increase past its transition temperature, the LCE contracts (mesogens become less oriented); returning to its original shape (mesogens become more organized), when the stimulus ceases [18]. If mechanically aligned, the LCEs can change from their untrained state (polydomain) to their trained state, (monodomain) [45]. Additionally, because of their limited thermal conductivity, LCEs can be locally heated without affecting nearby regions [64, 63]. While low thermal conductivity impacts actuation speed, which is often desirable, it may not always be critical (e.g., for systems that respond slowly, e.g., for solar tracking, or for stealthy

reconnaissance). Taking these features into account, we prepared an LCE strip (see *Fabrication* section) with embedded heaters in the regions we wish to actuate, and inserted this single sheet into a laminate mechanism to generate self-folding structures.

Due to its straightforward fabrication process, we selected the mechanical alignment method to fabricate LCEs with unidirectional actuation. However, folding complex origami geometries (e.g., a crane and flower) with a unidirectional actuation layer is challenging. We selected the Sarrus Linkage mechanism to overcome this challenge, given its capability to constrain two planes to be parallel, and allowing the unidirectional actuation of the LCE to generate folds along axes perpendicular and parallel to the actuation (see Figure 3.1A and Figure A.1 A). In other words, with this one degree of freedom (DOF) mechanism, we achieved biaxial folding with unidirectional actuation. These features of the Sarrus linkage allow pop-up self-folding mechanisms with a single tendon-driven actuation approach. We selected the dimensions of the Sarrus, based on the maximum contraction of our LCE (40%), as reported in previous work [63], and also consitent with the results in this paper.

To predict the fold angle of the Sarrus Linkage mechanism, we used a simple kinematic model relating the folding angle to the strain of the LCE [Equation (3.1)] where L is the overall length of monodomain phase LCE (35 mm), a is the length of side linkages of the Sarrus (11.5 mm), and b is the length of the top and bottom base of the Sarrus mechanism (12 mm). For the model, we assumed: i) uniform contraction of the LCE region containing the heating source; ii) ideal behavior of the rotational joints in the composite; iii) rigid links. Thus, we assumed that the LCE would behave as self-driven tendon that would uniformly pull the opposite joints to which it was attached, (Figure 3.2A).

$$\theta = cos^{-1}\left(\frac{L(1+\varepsilon(T))-b}{2a}\right) \tag{3.1}$$

To estimate the maximum payload of one Sarrus module, we used a static model (see Figure A.1). Based on the maximum force provided by the LCE actuator (F_{LCE}) and the angle of

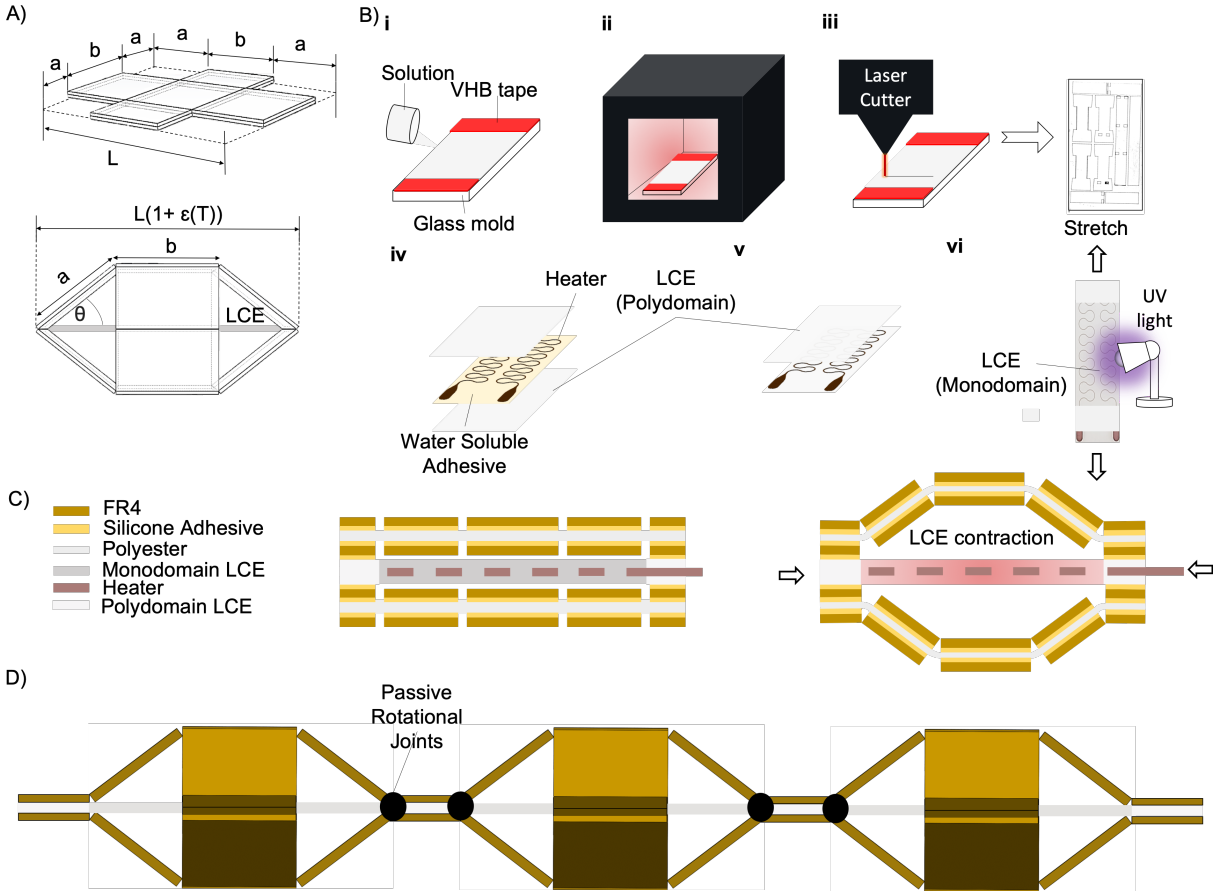

Figure 3.2: Design and fabrication of the Sarrus linkage modules and LCE actuation layer. A) Design parameters of the Sarrus module. B) Fabrication process of the LCE actuator (LCE): i) cast molding of LCE sheet, ii) solvent evaporation in an oven, iii) laser micromachining of LCE actuators, iv) transfer of photolithographically defined flexible electrical heater circuit onto the polydomain section of LCE actuator using a water-soluble adhesive, v) assembly of the LCE actuator with embedded heaters, vi) unidirectional alignment of the LCE actuator by mechanical strain and curing with UV light. C) Side view of monolithic Sarrus composite made using a laminate manufacturing approach [65] in flat (left), and poppep-up (right) configurations, with connecting links on the right and left sides added for composite manufacturing. D) Design of a crawler composed of three Sarrus modules embedded with a single distributed LCE layer (center layer, light gray) that can be locally actuated for locomotion.

the module (θ), we estimated the maximum payload (W_{max}) using Equation (3.2).

$$W_{max} = \tan(\theta) F_{LCE} \tag{3.2}$$

To demonstrate the capability of distributed actuation of the LCE actuation layer, we

designed a self-folding composite composed of three Sarrus modules in series (Figure 3.2D). We hypothesized that: i) by sequentially heating the three sections of the LCE actuator layer, we could induce a traveling wave of actuation for locomotion without the aid of directional friction pads. ii) by adding directional friction pads to the crawler, we could improve the locomotion speed of the crawler. To model the locomotion of the crawler with directional friction pads, we propose a simplified mass-spring-damper (MSD) system, (Figure A.2 A, Supplementary Material section *Crawler Locomotion Model and Simulation of Crawler Locomotion*). For the model we assumed that: i) the friction between the crawler and the ground is dependent on the direction of relative motion; ii) the effective equilibrium length of the springs in the MSD system are a function of the strains of the robot's LCE actuators [Equations (A.10-A.11)]. Given these assumptions, we can use Equations (A.7-A.9) to estimate the behavior of the crawler locomotion given the strain variation of the LCE.

3.2.2 Fabrication of Self-folding Composites with LCE

We fabricated the single Sarrus linkage mechanism module using a laminate manufacturing process, where patterned layers of different materials were stacked to form a smart composite (Figure 3.2C, Figure A.5A). The pattern of the layers for the Sarrus module crawler consisted of three Sarrus modules sequentially connected (Figure A.5B), and followed the same fabrication steps as a single module. We cut all the layers using a laser machining system (PLS6MW, Universal Laser Systems). The composite was comprised of the following layers: rigid (FR4, 254 μm); adhesive (high-temperature silicone tape, AR7876); smart material actuator (LCE, 500 μm per polydomain layer); flexural (polyimide, PI); and heating layer (microfabricated copper serpentines). The LCE and heating layer (coated with PI) were manufactured separately using a laminate (layer based) approach. For the joule heating layer, we used a fabrication method described in our previous work using photolithography [63]. This heating layer had a resistance of about 2 Ω. We fabricated the LCE using two step-polymerization method. The first step

used 10.957 g (18.6 mmol) of 1,4-bis-[4-(3-acryloyloxypropyloxy) benzyloxy]-2-methylbenzene (RM257, Wilshire company, 98%) dissolved into toluene and the mixture was heated at 85 °C on an oven for 20 minutes. Then, we added 0.0771 g (0.3 mmol) of the crosslinker (2-hydroxyethoxy)-2-methylpropiophenone (HHMP, Sigma-Aldrich, 95%) into the mixture and heated to 85 °C in an oven. We added 3.076 g (16.9 mmol) of 2,2-(ethylenedioxy) diethanethiol (EDDET, Sigma-Aldrich, 95%), the spacer in LCE and the tetra-arm thiol crosslinker, 0.244 g (0.5 mmol) of pentaerythritol tetrakis (3-mercaptopropionate)(PETMP, Sigma-Aldrich, 95%) into the mixture. After that, we added 0.038 g (0.4 mmol) of dipropylamine (DPA, Sigma-Aldrich, 98%), the catalyst, into mixture. Next, we stirred and degassed the mixture in the vacuum chamber to remove bubbles.

We poured the precursor into a rectangular mold (170 mm x 110 mm x 0.5 mm), Figure 3.2C(i), and after 24 hours of chemical reaction at room temperature, we removed the glass slide and put the sample into the oven to evaporate the solvent (toluene) for 12 hours (Figure 3.2B(ii)). We then defined the shape of our actuators by laser micromachining (Figure 3.2B(iii)), which for this work were rectangular shapes, but we have also explored other shapes (dog-bone) according to our Sarrus based designs such as the lily and crane (Figure 3.2B(iii), top view). After this first crosslinking step, we transferred the circuit using water soluble adhesive onto the polydomain LCE (Figure 3.2B(iv)); then we put the composite into a water solution to dissolve the adhesive. Once the adhesive was dissolved, we attached another polydomain phase LCE layer onto the LCE layer with the heater, (Figure 3.2B(v)). For the second step, aligning the LCE directors (mesogens), we stretched the loosely crosslinked LCE film (pre-strain = 100%) by external force, then exposed it to ultraviolet light irradiation for 30 minutes (Figure 3.2B(vi)), while also protecting the regions we desired to maintain as polydomain for the assembly of the Sarrus mechanism. In this fabrication process, we also observed that the polydomain LCE had an increased adhesiveness as compared to its monodomain section. Therefore, we used this feature to our advantage by selecting these regions as the constraining points (connecting links) of the

laminate Sarrus mechanism (Figure 3.2C).

3.3 Results and Discussion

3.3.1 Characterization of the LCE Actuator

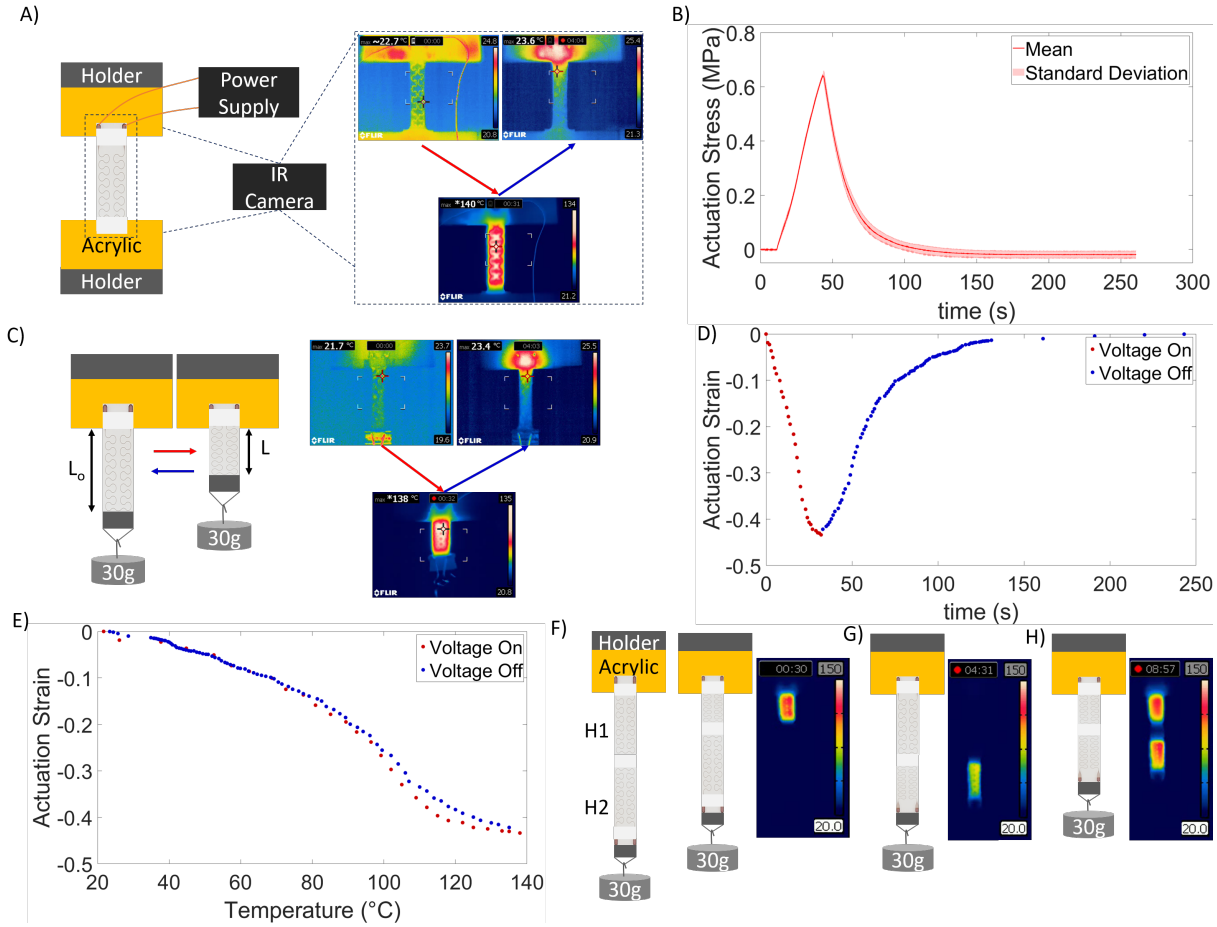

Figure 3.3: Characterization of the LCE actuator. A) Experimental setup of the actuation stress of the LCE when fixed and the thermal image of the LCE's maximum temperature, reached within 30 s. The red and blue arrows represent the heating and cooling, respectively, of the LCE actuator. B) Actuation stress measurements of the LCE when joule heated. C) Reversible actuation strain test of LCE sample and its respective thermal image. D) Actuation strain of the LCE as function of time when heated for 30 s and cooled at ambient temperature with a mass of 30 g. E) Strain and Temperature relationship of the LCE when joule heated at 3.5 V for approximately 30 s. F) Distributed actuation of the single LCE actuation layer with heater one. G) Actuation of heater two. H) Actuation of both heaters.

To characterize the behavior of the LCE, we performed three different experiments. The first two measured actuating stress and actuating strain with respect to temperature and time, and the third was a test of the distributed actuation of the LCE.

For the first experiment, we attached and fixed the length of the LCE sample with an embedded heater on a mechanical testing apparatus (Instron 5969), and measured the actuating stress as a function of time of the LCE as well as its maximum temperatures within the frame of the Infra-Red (IR) camera upon turning on the power supply. We repeated this experiment three times for the same sample, and averaged the results (Figure 3.3A and Figure 3.3B).

We observed the reversibility of the LCE after being thermally activated with Joule heating. The LCE reached maximum stress ($\sim$ 0.64 MPa) within the 30 s of actuation and relaxed to its original state within two minutes at room temperature (Figure 3.3B).

For the second experiment, similarly to our previous work [63], we measured the actuation strain by mounting a mass of 30 g on the opposite side of the circuit pads embedded in the LCE actuator sample (8 mm x 35 mm x 0.7 mm), and applied an electrical potential of $\sim$ 3.5 V (Figure 3.3C). We measured the temperature variation using an IR camera (FLIR E60) and analyzed the LCE contraction using the software ImageJ. We used image analysis to measure the strain of the LCE so we could avoid any constraint on the LCE during its activation (contraction). We calculated the *actuation strain* as $\varepsilon = (L - L_o)/L_o$, where L_o and L are the lengths of LCE artificial muscle in the initial (loaded) and fully actuated states, respectively.

In these experiments, we noticed a similar actuation and relaxation behavior regarding the strain of the LCE when we thermally actuated it for at least 30 s. The maximum strain was $\sim$ 43%, consistent with our previous work [63] that used an LCE synthesis with a similar cross-linking density. The LCE instantly started to relax when the Joule heating stopped (Figure 3.3D-E). We only observed a small difference in the temperature-strain relationship while cooling as compared to heating (maximum strain difference of 0.03 at 112 °C). This result indicates that thermal hysteresis of the LCE is not significant, which is a desirable feature for actuation control

and is consistent with the conclusions of previous work [51]. We believe these small variations in strain were due to the high sensitivity of the LCE to temperature variations. This sensitivity combined with nonuniform heating resulted in small undulations of the LCE that we observed when the LCE started to cool down at ambient temperature.

In the third experiment, we characterized the feasibility of distributed (local) actuation of the LCE, a desirable feature for sequential actuation of modular systems (Figure 3.3F-H). For this experiment, we first manufactured a single sheet of LCE with two embedded heaters that can be activated independently. The fabrication process was similar to that described in the fabrication section, but in this case we repeated the process of training by fixing the polydomain phase LCE and stretching each segment we wanted to train for reversible actuation. This method allowed the fabrication of a single strip with two segments (or more) of monodomain phase LCE for actuation (Figure A.4). To test the distributed actuation, we fixed one end of a two-segment actuator, and suspended the mass of 30 g from the other (Figure 3.3). We then activated the first monodomain segment of the LCE sheet and measured the temperature with the IR camera, later we repeated this procedure by heating the second monodomain segment of the LCE, and measured its temperature (Figure 3.3G). Finally, we measured the temperature when both segments of the LCE sheet were activated by Joule heating (Figure 3.3H).

By locally activating each segment of the LCE we were able to achieve distributed actuation of a single layer of LCE actuator (Figure 3.3F-H). This result demonstrates the potential to use our strip of LCE actuator for distributed actuation of reversible self-folding composites.

3.3.2 Characterization of the Sarrus Modules

For the characterization of reversible self-folding, we measured the actuation strain of the LCE embedded in one Sarrus module with no added load when heated (for approximately 35 s), and then let it fully relax, for at least three minutes (Figure 3.4A-C). We repeated this experiment three times and measured the strain on each trial as well as its corresponding folding angle as

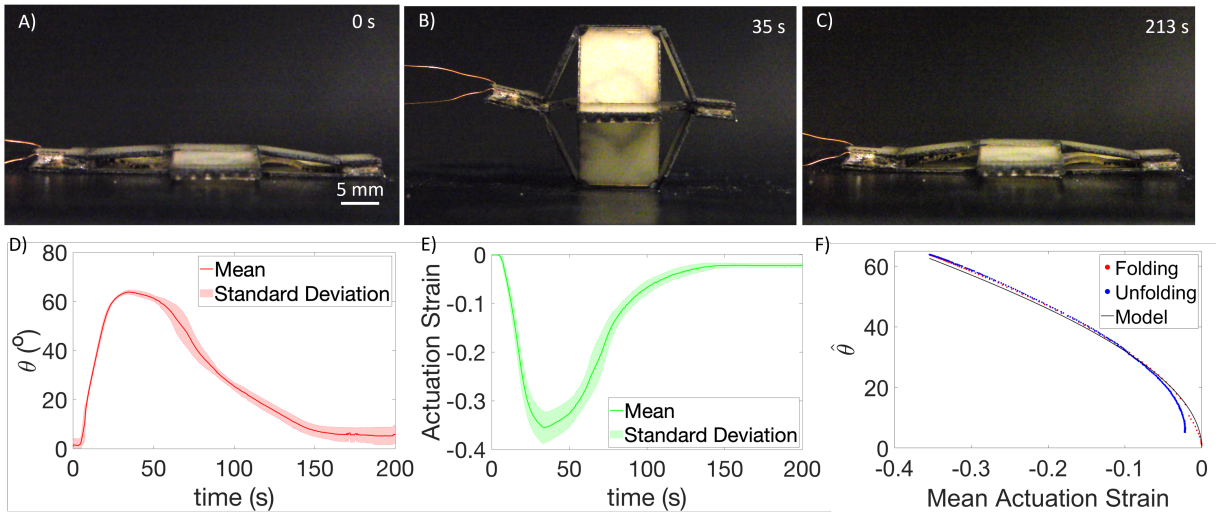

Figure 3.4: Characterization of reversible self-folding of the Sarrus linkage mechanism with the LCE actuator. The embedded heater heats the LCE in the Sarrus mechanism from A) to B) for 35 s when the power supply is on and it stops the heat once the power is off, B), reversing to its unfolded state, C). D) Folding angle plot as function of time, where the maximum averaged angle is approximately 64° among three trials of sequential actuation and relaxation of the LCE. E) The plot of the actuation strain of the LCE in the mechanism as function of time. F) Folding angle prediction based on the average actuation strain, compared against angle measured using image processing software.

a function of time using the image processing software Tracker (open source software, Open Source Physics (OPS) group) (see Figure 3.4D-E).

In Figure 3.4D, we observed the maximum folding angle of $\sim 64^\circ$ when we actuated the Sarrus module for 35 s. Upon turning off the power supply, the module reversed to its original state within two minutes. The strain of the LCE actuator embedded into the Sarrus module showed similar response (when heating and cooling) compared to when we tested the LCE actuator alone (Figure 3.4E). Furthermore, we showed the adaptability of the Sarrus module for biaxial folding of reversible self-folding origami-inspired designs, such as a lily (Figure A.6A) and a crane (Figure A.6B).

To predict the fold angle, we used the average actuation strain of the LCE embedded in our module to calculate the fold angle based on the geometric model [Equation (3.1)] and compared it to the value measured from experimental images (Figure 3.4F). Overall, our geometric model was

predictive with relatively small deviation (maximum value of 9.7°) which was more pronounced at the end of the unfolding of the module (i.e., when it returned to a flat state). We believe this deviation occurred because the physical mechanism did not fully match the assumption of perfect rotational joints. Due to the nonzero thickness of our composite (see Figure 3.2C-D), the joints at each end of the module that we approximated as a single joint actually behaved as two joints separated by a small distance. Thus, any asymmetry in the contraction of the LCE could cause the connecting links at the extremities of the composite to rotate instead of staying parallel to the ground. Nonetheless, the overall root mean square error (RMSE) was small (4.8°) particularly when folding (popping-up, RMSE of 1°). These results indicate that the assumption of perfect rotational joints is a good first approximation for predicting the folding angle. Moreover, this result also suggests that this simple geometric model could be used as a design guideline for other laminate based Sarrus modules as a function of an actuation strain.

3.3.3 Load Bearing Capability

For the lifting experiment, we incrementally increased the weight and heated the actuator for a maximum of three minutes (or until the module lifted from its flat position), Figure 3.5A-C.

We demonstrated that one Sarrus module (mass of 2.6 g) could hold and lift vertical loads 38 and 13 times its weight, respectively (Figure 3.5A-F). At its flat position, the module is in a singular configuration and theoretically requires infinite force to lift a weight [see Equation (3.2)]. However, in practice, when the LCE started to heat a small angle was formed on the joints of the module, and the Sarrus snapped from flat to folded position while supporting a load of 343.35 m·N (mass, 35 g), see (Figure 3.5A-C). The snapping is a result of the stored energy on the LCE, which increases with temperature. Based on our static model and the maximum average block force of the LCE ($\sim$ 3.5N), measured in the same mechanical apparatus as described in the *Characterization of the LCE Actuator* section, we predicted a maximum load of 6.867 N (mass, 700 g).

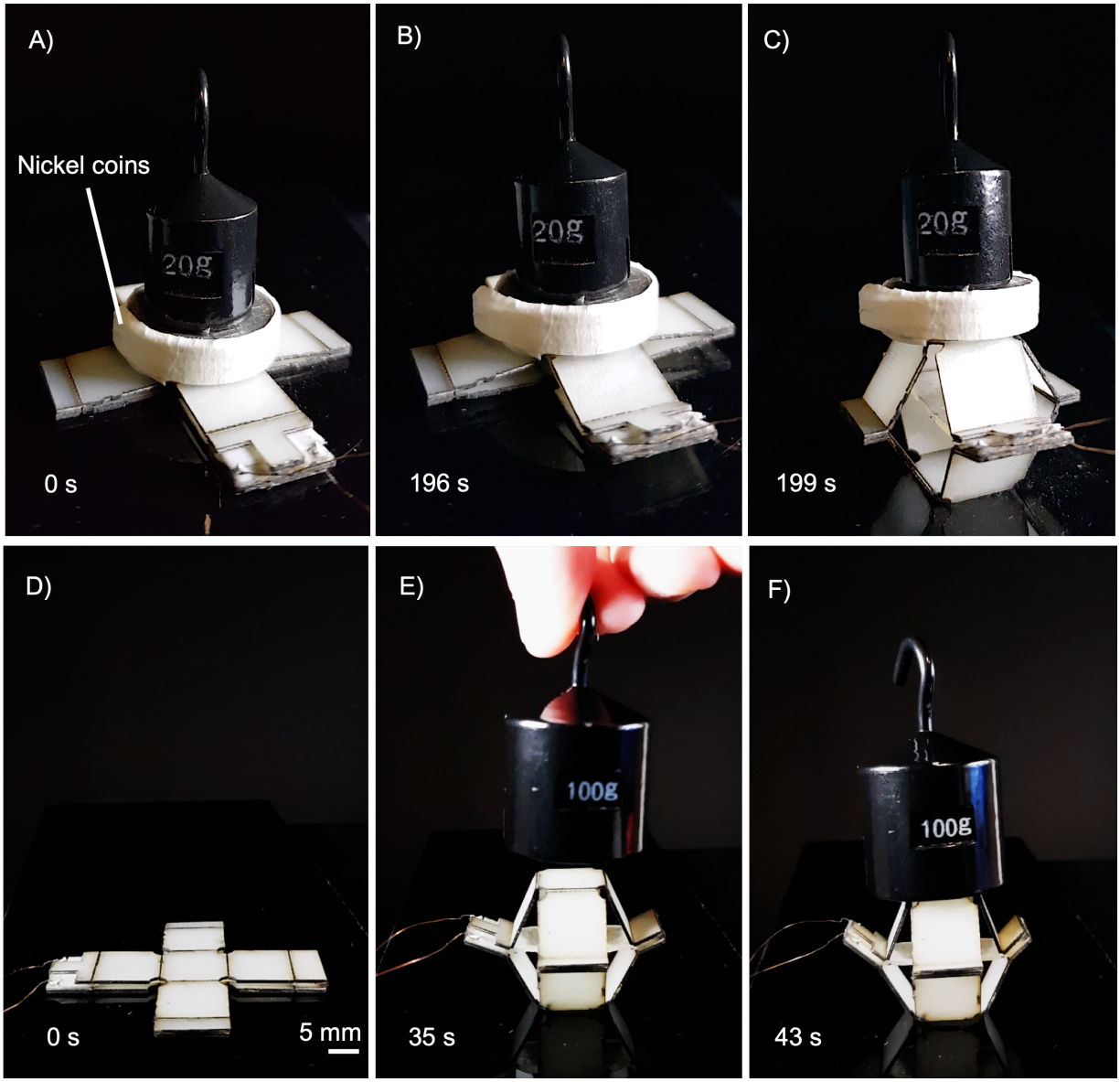

Figure 3.5: Weight-to-strength ratio of the Sarrus module (mass, 2.6 g,load of 25.5 m·N). A) Flat state of the Sarrus module with a mass of 35 g (load, 343.35 m·N) consisting of three nickel coins and a 20 g mass (load, 19.6 m·N). B) Beginning of folding and lifting of the 35 g mass from its flat position. C) Quick lifting of the payload upon initial folding from flat. D) Initial flat position of the Sarrus. E) Folded state of the Sarrus module for holding 100 g. F) The Sarrus module holding a mass of 100 g (load, $\sim$ 1 N) upon actuation.

For the holding experiment, we Joule heated our module for $\sim$ 35 s and then incrementally added loads (Figure 3.5D-F). Within this actuation time, the module was capable of holding 100 g (load, $\sim$ 1 N) (Figure 3.5D-F). At this point, we observed that the connection joints started to

bend upwards with the load (Movie S2). With a mass of 200 g (load, $\sim$ 2 N), the Sarrus started to tilt when the weight was on it, which made the weight fell off of the module. These results demonstrate that our module can lift and withstand significant vertical loads perpendicular to direction of the LCE actuation that would be very challenging with a soft layer of smart material alone.

3.3.4 Distributed Actuation of Self-Folding Modules

To demonstrate distributed actuation of the modules, we first fabricated an LCE strip with three actuation segments, one for each of the Sarrus modules of a three-module crawler. We fabricated the actuators and modules using the procedure explained in the Fabrication section, and further illustrated in Figure A.4. We then activated each of the Sarrus modules separately, starting from its original flat state, Figure 3.6A. This independent actuation of modules is an advantageous capability for the local control of multiple module with a single, embedded actuation layer.

We demonstrated this capability for locomotion by sequentially actuating a crawler composed of three Sarrus modules, and tested its locomotion with and without directional friction pads. We sequentially activated each module by applying an electrical potential of approximately 4 V for six cycles (18 actuations per test) with a cycle period of 117 s (see Figure 3.6B). We tested two actuation gaits (Figure 3.6C): 1) Sequential activation of modules in numerical order (right to left, "NP123", Figure 3.6D), and 2) sequential actuation in the opposite order (left to right, "NP321", Figure 3.6E). To analyze the motion of the crawler, we tracked the modules with the software Tracker, and all measurements were with respect to the origin (x,y) (see Figure 3.6C). For all of the crawler locomotion experiments, the robot moved on a smooth spring steel surface.

3.3.5 Crawler Locomotion without Directional Friction Pads

To achieve locomotion of our three-module Sarrus crawler, we generated a wave of actuation along the length of the crawler. The resulting locomotion of the crawler was opposite to the direction of the wave propagation (see Figure 3.6D-E). This behavior is also observed in earthworms (called retrograde peristalsis). The retrograde behavior of the worms occurs because of the contraction and relaxation of its segments combined with friction from their setae [66]. The first segment contracts, and propagates the wave but as the following segments of the worm contract, the setae act as anchor impeding the movement in direction of the sequence of contraction. Whereas the relaxing segments have lower friction than the ones contracting, and allow the movement against the wave. Thus, the gait actuation of the earthworm works with at least three minimum segments alternately contracting, anchoring and relaxing. After a cycle of contraction and relaxation, the worm has moved against the direction of the wave propagation (see Figure 3.6F).

This locomotion behavior analogous to that of the earthworm occurred with the actuation of our modules in both gait sequences, 123 and 321 (see Figure 3.6D-E, Movie S3). As the first module contracted and tilted, it propagated the wave to the second module as this started to contract (27 s). The second module then behaved as the anchor (high-friction) for the crawler (27 s - 52 s). Then, as the first module relaxed, expanded horizontally, (low-friction, $\leq$ 27 s) the third module started to contract becoming the anchor (42 s - 52 s), while the second and first modules relaxed, thus inducing locomotion against the sequence of actuation. In other words, the high-friction and anchoring behavior occurred when the base of the modules was in full contact with the surface and the module was fully contracted, limiting motions against the direction of the LCE contraction.

The low-friction and overall net displacement direction occurred when the LCE relaxed, and some of the modules tilted towards the direction of the sequence of relaxation (Figure 3.6D-E, 52 s - 117 s). This behavior made the crawler move opposite to its sequence of actuation. The

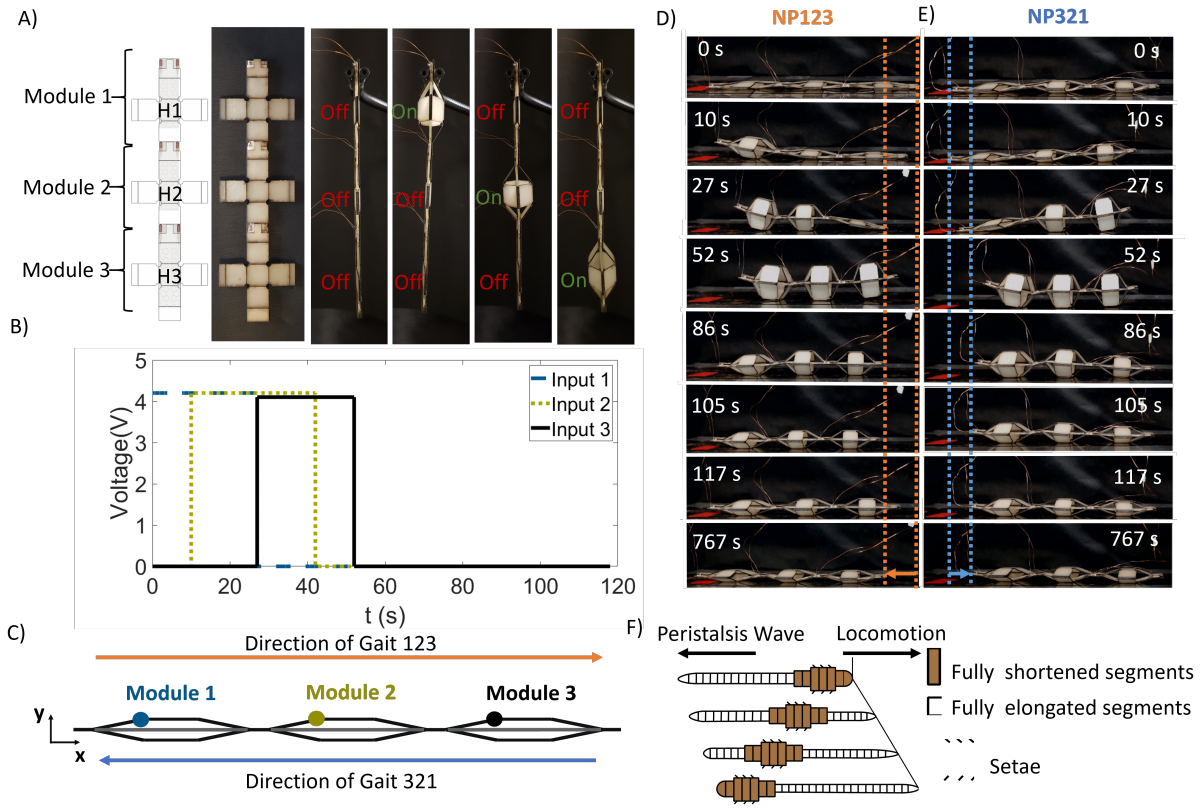

Figure 3.6: Distributed actuation of the crawler made of three Sarrus modules when each embedded heater (H1, H2, H3) is activated. A) Schematic showing a top view of the three modules with their respective actuators and the side view of the sequential actuation of each module. B) Input signal for the activation of the LCE through Joule heating. C) Schematic of the modules and the respective direction of actuation given the gait sequences 123 and 321, where the circles indicate the location of the the points tracked for displacement. D) Screenshots of the first and last cycle of actuation (with relaxation) of the crawler without pads and gait 123 (NP123). E) Screenshots of the first and last cycle of actuation (with relaxation) of the crawler without pads and gait 321, (NP321). F) Visual representation of the earthworm locomotion due to the retrograde peristalsis (adapted [66]).

gait 123 generated an overall crawler displacement of negative 17 mm (backwards), whereas a gait 321 made the crawler move 10 mm forward (Figure 3.6D-E, Figure 3.8B).

Without pads, the crawler had an average velocity per cycle of 0.4 mm/min ($\pm$ 0.7) and -1.4 mm/min ($\pm$ 0.6) with the 321 and 123 gait, respectively. We also observed a small out-of-plane displacement (yaw rotation) of the crawler with the 321 gait contributing to the small consistency of this displacement per cycle. We believe that this is due to the asymmetric loading

related to the electrical pads and tethers (see Figure 3.6D). Nonetheless, these gait sequence results indicate the feasibility to direct the overall crawler locomotion (forward and backward) without any directional friction pads. Unlike earthworm locomotion, which has the setae for directional friction, our robotic crawler used retrograde peristalsis motion without any features to enhance friction. The motion was solely based on the behavior of the three Sarrus modules design in series and their local actuation that varied their angle of contact with the ground.

3.3.6 Crawler Locomotion with Directional Friction Pads

To increase the displacement per cycle of our crawler (i.e., to limit backwards slippage), we added directional friction pad with minimum friction in the direction of propagation of the actuation wave. The pad had higher and lower friction with motions against and towards the foam position, respectively (see Figure 3.7A). The pads consisted of a rigid layer (R), foam (F), and a high-friction layer. For the latter, we used a gecko-inspired adhesive (G), which are known to have high friction under shear loads just as gecko feet, while being compact, patternable, and lightweight [67, 68] (more details on background and fabrication of gecko-inspired adhesives in Appendix A, *section Gecko-Inspired Adhesives and Manufacturing Approach*). When the pad was slightly tilted towards the foam, the unconstrained part of the gecko-inspired adhesive was flipped, decreasing the friction in that direction. Whereas, when the motion was against the foam the gecko-inspired adhesive tended to have more surface area contact with ground, thus having higher friction in that direction (i.e., van der waal force interaction).

Combining the pads and crawler behavior with the gait sequence 123, we observed that the locomotion of the crawler was analogous to a caterpillar (Figure 3.7B). The caterpillar moves by propagating a traveling wave through its body (compression and re-extension of its segments), with the support of its prolegs that assist with the motion of the caterpillar in the direction of wave propagation [69]. As the wave propagates through the caterpillars' body, the terminal and adjacent legs are lifted while the remaining legs hold their position, which allows the caterpillar

to move in the direction of wave propagation.

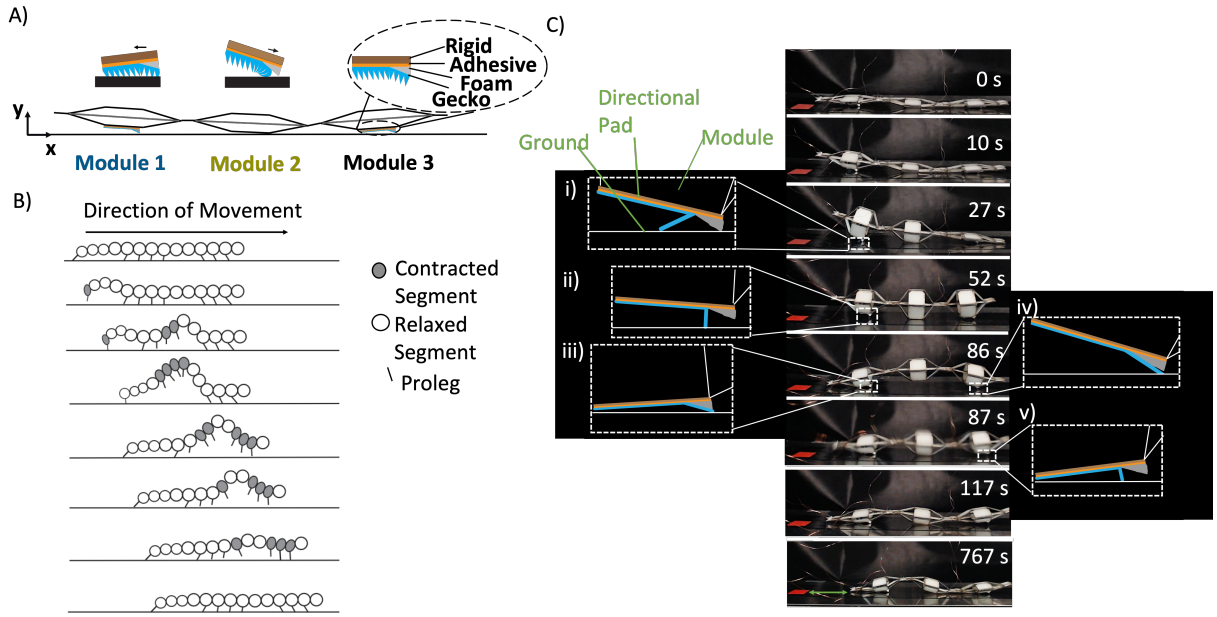

Figure 3.7: Directional locomotion of the Sarrus crawler with friction pads with gecko-inspired adhesive causes motion analogous to the caterpillar. A) Schematic of the Sarrus crawler made of three Sarrus modules in series. Module 1 and Module 3 also have directional friction pads for enhanced locomotion. The pad has low friction when the motion is toward the foam and high friction when against it. B) Illustration of the caterpillar locomotion given its body traveling wave propagation (adapted [70]). C) Representative experimental images showing the behavior of the Sarrus crawler moving due to the sequential activation of the LCE actuator layer and the directional friction pad. i) Gecko-inspired adhesive pad flipping clockwise with the module, enabling low friction to the module. ii) Marginal state of the gecko-inspired pad when module 1 is relaxing and starting to rotate counterclockwise. iii) Gecko-inspired adhesive pad in contact with the ground, enabling high friction to the module. iv) Clockwise rotation of module 3 and the beginning of the gecko- adhesive layer to flip as module 2 relaxes. v) Rapid flipping of the gecko-adhesive layer switching between the low and high friction state of the pad.

We observed a behavior similar to the caterpillar when we sequentially actuated the modules of the crawler with the directional frictional pads (see Figure 3.7C) and Movie S5 (additional information in the *Supplementary Material*). Most notably, as the first module contracted, it tilted, and propagated the wave to the second module (Figure 3.7C, 10 s-27 s, Movie S4). Once contracted, the second module pulled the first module towards it. This action exposed the low-friction region of the directional friction pad to the ground as the unconstrained part of the gecko-inspired adhesive flipped backwards. The foam then allowed the module to

slide and move towards the second module at 27 s. (Figure 3.7C). As the first module started to relax, it began to tilt counterclockwise, bringing the gecko-inspired adhesive side of the pad in contact with the ground again, and preventing the locomotion towards the first module.

Once the second module started to relax it became constrained by the first and third modules because the gecko-inspired adhesive on these pads were in full contact to the ground. Since the second module was constrained to relax horizontally, it started to move upwards losing contact to the ground at 86 s (Figure 3.7C). As the second module moved upwards, it induced the third module to rotate clockwise. This rotation made the gecko-inspired adhesive contact the ground to decrease and become an anchor for the third module rotation, until the gecko-inspired adhesive flapped backwards to the low friction direction of the pad. This allowed the third module to briefly slide in the direction of the actuation wave propagation, which made the second module drop back to the ground at 87 s (Figure 3.7C). This cyclic behavior with directional friction pads generated an average net displacement of 29 mm with a motion analogous to the caterpillar (Figure 3.8A, Figure A.9B). These results demonstrate the feasibility of using distributed actuation in a robot composed of self-folding Sarrus modules to achieve directional locomotion.

3.3.7 Crawler Performance with Directional Friction Pads

We also tested the relationship between the geometry of the foams on the pad, adhesive design patterns (gecko inspired patterns and smooth silicone rubber) and crawler displacement. For geometry of the foams on the pad, we used two designs made of the same foam (about 1.6 mm thick) but fabricated differently (Figure A.7). One consisted of cutting the foam pad horizontally, obtaining a rectangular cross-section area with a straight-forward fabrication approach. The second geometry consisted on making a diagonal cut on the foam, which generated a triangular cross-section area for this foam pad (Figure A.7A-B).

To achieve high-friction for the directional pad, we tested two silicone high-friction layers: plain and patterned with gecko-inspired adhesive. The former provided a straightforward

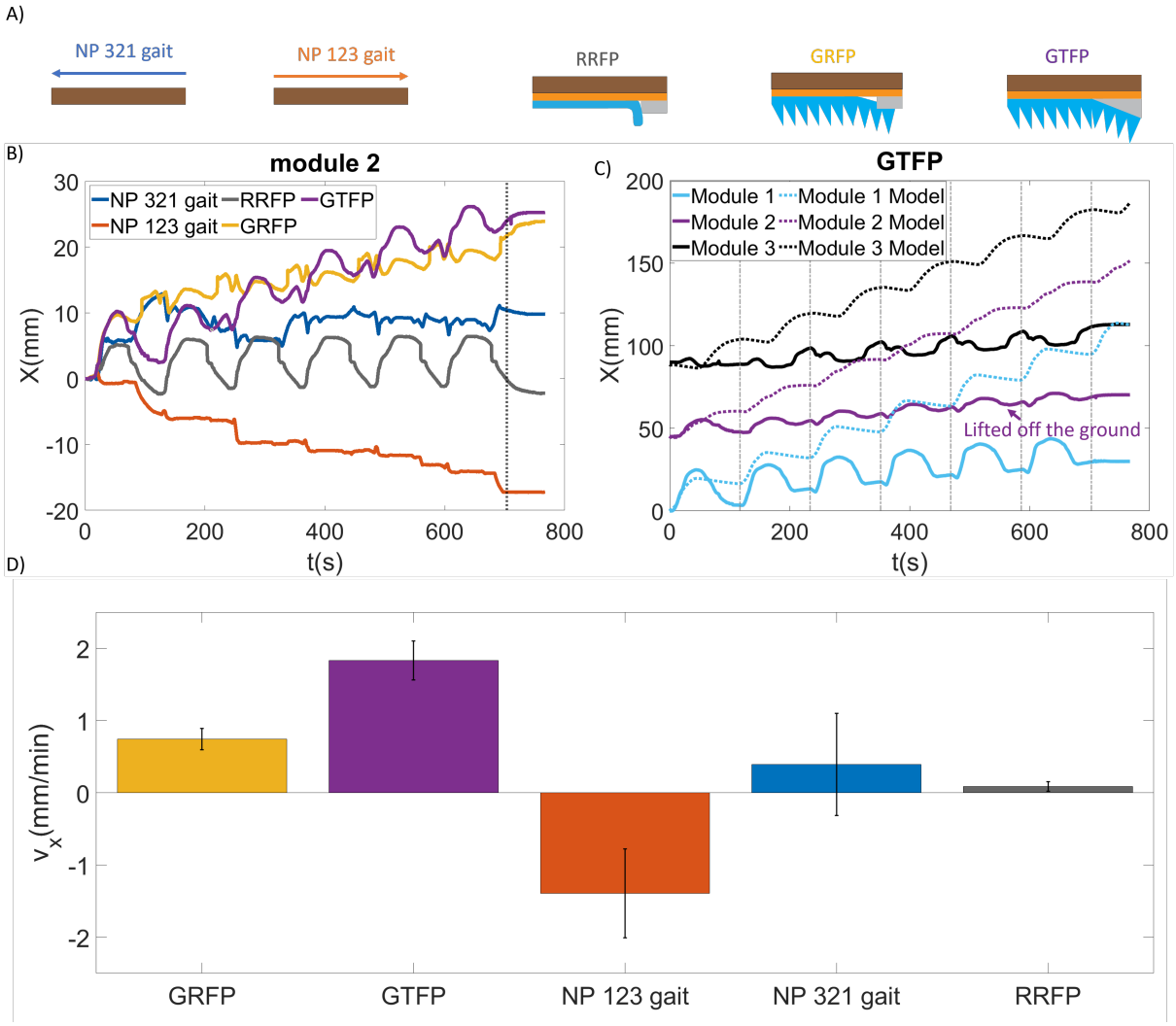

Figure 3.8: Performance of the crawler with and without frictional pads. A) Pad design. From left to right: No pad (NP) 321 gait with an actuating sequence from modules three to one and NP 123 gait with an actuating sequence from modules one to three; pads with anisotropic friction layers for directional friction varying based on the design of the foam (low-friction) and silicone layers (high-friction): Rectangular Rubber Foam Pad (RRFP); Gecko Rectangular Foam Pad (GRFP); and Gecko Triangular Foam Pad (GTFP). B) Horizontal displacement of the center module of the crawler for five experimental cases: no friction pad (NP 321), no friction pad (NP 123), and crawler with directional friction pads RRFP, GRFP, and GTFP, as described above. The dotted vertical line indicates the end of its sixth cycle of actuation and beginning of the full relaxation of the crawler. C) Comparison of the displacement of each module of the crawler in simulation (dotted lines) and experiment (solid lines) with respect to the first module, for the GTFP case. The dashed-dotted vertical lines indicate the beginning and ending of each cycle for comparison between data. D) Mean velocity per cycle for the five cases tested.

fabrication process providing a smooth layer without microfeatures. While the latter consisted of microwedges that deform under shear loads to modulate van der waal forces, providing a strong adherence on the surface [68]. The details regarding the fabrication of these patterns are described in the Supplementary Material. Both high-friction layers were attached along a portion of the directional-friction pads so that the rubber would contact the surface when moving in one direction and fold out of the way when moving in the other way [68] (Figure 3.7A, Figure A.7C-D).

We tested the locomotion and velocity repeatability for the crawler outfitted with each friction pad design. In all cases, the crawler locomotion settled to a more constant velocity within three cycles (see Figure A.8C and Figure A.8B for the displacement per cycle). For average velocity per cycle comparison, we considered the locomotion performance from the third to last cycle.

With pads, we improved the forward locomotion (gait 123) with respect to the crawler without pads, and observed the performance of the pads with different materials and foam geometry (Figure 3.8A). The pads with silicone rubber and rectangular foam cross-section (rectangular rubber foam pad, RRFP) had an average velocity per cycle of 0.1 mm/min ($\pm$ 0.1) without significant displacement after six cycles (-0.1 mm). This result indicates that the silicone rubber by itself was not enough to prevent backward motion of the lightweight crawler during segment relaxation. However, the pads with the gecko-inspired-adhesive and rectangular foam (gecko rectangular foam pad, GRFP) had an average velocity per cycle of 0.7 mm/min ($\pm$ 0.1) with a velocity performance similar to the crawler without pad (although more consistent per cycle).

Despite that, the GRFP pad had an overall displacement (from first to sixth cycle) of 21 mm (Figure 3.8B-C). This occurred because the crawler slipped the most in the initial cycle. The gecko-inspired adhesive helped to prevent this slippage and maintain a positive velocity for all cycles (Figure A.8C). The gecko inspired adhesive with triangular foam (gecko triangular foam pad, GTFP) had an average velocity per cycle of 1.8 mm/min ($\pm$ 0.3) and overall displacement

after six cycles of 24 mm, outperforming the previously discussed cases with and without pads. Given this performance, we also tested the same pad design to validate its consistency with a different crawler (gecko triangular foam pad two, GTFPC 2) and obtained an average velocity per cycle of 2.1 mm/min ($\pm$ 0.7) and overall net displacement after six cycles of 33 mm (Figure A.9B-C). In both cases with the GTFP design, we observed that crawler obtained its best performance moving forward.

Overall, the crawler with gecko-inspired adhesive moved faster than the one with a plain silicone rubber layer. This result indicates that the directional pads with gecko-inspired adhesive had a higher-friction — despite the negligible preload from our crawler weight — than the silicone rubber. Additionally, we observed that both the cross-sectional area, as well as the material of the exposed foam, contributed to the speed of the crawler moving forward. This coupled result occurred because the triangular foam pad had little to no backing compared to the rectangular (see Figure A.7A(i)-B). The raw foam consisted of two backing layers sandwiching a more compliant layer. Thus, the compliance of the exposed cut face of the triangular foam could have contributed to a lower friction, improving the anisotropic behavior of the pad and giving better overall performance. Considering both the geometry and exposed material of the foam pad we tested, the GTFP did perform better than the GRFP. However, further study would be necessary to decouple the effects of the geometry and the material of the foam on the overall speed of the crawler. Nonetheless, we demonstrated an option for improving the locomotion speed of thermally actuated systems such as a composite crawler actuated with LCE using laminate anisotropic friction pads.

3.3.8 Comparison of Model and Experiment with Directional Pads

A comparison of the experimental locomotion of our LCE actuated crawler with that predicted by the MSD model reveals overall agreement in the motions (Figure 3.8C). The overall net displacement per gait cycle for each module of the crawler occurred within the same portion

of the gait, and the shape of the displacements curves are similar (although different in magnitude, off by a factor of approximately four). Each module moved forward (positive slopes of the curves within cycle) and slightly backwards (negative slopes of the curves within cycle) consistently for each gait cycle (Figure 3.8B). Additionally, the relative amplitudes of the displacements of each module followed a similar trend in model and experiment (i.e., Module 1 exhibited the highest and Module 2 the lowest amplitude). These results support our hypothesis that the crawler locomotion can be largely described by a MSD system with sequential distributed actuation of the springs, combined with directional friction pads.

Looking more closely at the experimental results (Movie S5), the deviation from the predicted displacements occurs when Module 2 starts to lift off the ground. This vertical motion of the second module that occurred during its relaxation phase did not contribute to the forward locomotion of the crawler, which is represented by the decrease in slope curves at the end of each gait cycle on the experimental curve (Figure 3.8C, see annotation). This loss in displacement due to the module losing contact with the ground was not captured in the model. This effect, combined with the use of approximate values for the coefficient of friction and stiffness (see details on the Simulation method in the *Supplementary Materia*l) caused an over-prediction of the displacement in simulation by a factor of four with respect to the experiments. Nonetheless, the similarities between the simulated and experimentally observed motions, allowed the model to provide insights into the behavior of the crawler, as described above. Furthermore, these results form a basis for the optimization of the locomotion of LCE actuated origami crawlers in future studies.

3.4 Conclusion

In this chapter, we demonstrated a reversible, patternable and lightweight actuation method using Liquid Crystal Elastomers for self-folding systems. We showed that with a single,

unidirectionally trained monodomain LCE actuation layer, we were able to achieve a biaxial folding system using a Sarrus Linkage mechanism. The laminate Sarrus module with integrated LCE converted the unidirectional actuation of the LCE to foldings along axes perpendicular and parallel to the direction of actuation. This allowed us the versatility to accomplish complex foldings with simple actuation. Additionally, we demonstrated the distributed actuation of a modular self-folding robot made of three Sarrus modules with a single sheet of LCE embedded within the composite. We showed that our modular self-folding robot can achieve locomotion forward (with and without directional friction pads) and backwards through traveling waves caused by sequentially actuating the modules of the crawler. Given these features, we envision the use of a LCE layer of actuation for reversible self-folding of composites could enable novel ways to design, actuate, and control lightweight laminate robotics systems. These features are particularly desirable for search-and-rescue and medical applications because of the intrinsic scalability and morphability obtained through origami-inspired self-folding designs.

There are also many opportunities for further work. In particular, to address the challenges of the relatively low LCE actuation speed and exploring the tunability of the LCE for milli-scale robots. Since the LCE actuation is thermally driven, its actuation is not fast or energy efficient [63] which may limit its applicability. The speed of actuation is limited by the cooling time of the LCE. Previous work has addressed this challenge using a fluidic system [71]. However, this type of system is challenging to scale down and may have issues with leakage. Alternatively, thermoelectric coolers may offer a scalable fabrication process. Another approach is to tune the LCE material properties to achieve lower transition temperatures (with the cost of smaller range of operating temperatures). As we showed in this work, the LCE allows for a tunable and patternable laminate manufacturing approach for lightweight self-folding mechanisms. Thus, future work could explore gait sequence and parameter optimization (e.g., coefficient of friction and actuator design) of the laminate crawler for locomotion. Similar to a caterpillar, there is an opportunity to investigate traveling wave propagation of our system for locomotion at different

inclines.

Chapter 3, in full, is a reprint of the material as it appears in **Minori, A. F.**, He, Q., Glick, P. E., Adibnazari, I., Stopol, A., Cai, S., & Tolley, M. T. (2020). Reversible actuation for self-folding modular machines using liquid crystal elastomer. Smart Materials and Structures, 29(10), 105003. The dissertation author was the primary investigator and author of this paper.

Chapter 4

Soft power amplification system for jumping using patternable artificial muscle and snap-through of shells

4.1 Introduction

Soft robots—i.e., robots composed primarily of soft materials—have the potential to be more adaptable, conformable, and resilient than their rigid counterparts [4]. While many soft robots move slowly using bioinspired locomotions such as crawling, walking [9, 10] or slithering [72], previous work has taken advantage of the properties of soft materials to achieve rapid locomotion, for example jumping. A soft body can help jumping robots absorb the impact of landing without the need for dexterous landing capabilities [73, 74, 75]. To achieve mesocale jumping, compact and lightweight actuation is necessary. However, previous actuation methods for soft jumping robots used pneumatic actuation [76], chemical combustion [74, 73], or high voltage artificial muscles [75] that required either large rigid components or heavy external power supplies. Another challenge of soft jumpers is the trade-off between weight, and speed, given their

dependency on the size of the system and its actuation. For instance, low-voltage (i.e., < 12 V) and electrically driven smart materials offer compact, accessible and lightweight actuation but tend to be slow [62, 71, 50]. This time response is tied by the composition of these smart materials and their source of stimulation for actuation such as temperature, p.H., and moisture [12, 13].

In nature, rapid motions can be achieved by fully soft animals and plants such as the gal maggot larvae and the Venus Flytrap, respectively. The former can jump heights comparable to fleas (arthropods), and are thus among the best jumpers (relative to its body size) in nature [2]. The gal maggot larvae uses a latch-mediated spring-actuated mechanism that is slowly but forcefully actuated for jumping [2, 77]. This larvae jumps by forming an loop with it's body, with its head and tail held together by an adhesive latch, while it contracts its muscles to store elastic energy; when unlatched, this energy is released, as the larva pushes against the ground and takes off. Venus Flytraps, by contrast, are able to generate ballistic motions to trap insects for nutrition due to snap-buckling instabilities in their body [78]. Previous work has emulated these biological motions using artificial muscles [79], or fluidically actuated shells [76]. However, these approaches have relied on mechanisms that were coupled, where the energy is stored within the soft actuator itself, or in the shell design. Making these systems unable to decouple (i.e., temporally separation between the soft and slow actuator from the energy storage element) or to simultaneously optimize these components for jumping.

A common strategy to amplify the power output from an actuator is to use an amplifying systems/mechanism (e.g., a motor-spring-latch system [80, 77]). Particularly, the advantage of using composites with a motor-spring-latch for the power output of the actuator is that it offers a modular approach for synthesis and analysis by allowing spatially and temporally separation between each element. This type of system also enables the usage of artificial muscles that, albeit lightweight, have slow actuation speed but with sufficient force can transfer energy for the spring [81, 80].

Liquid Crystal Elastomer (LCE) is an example of an artificial muscle that is soft, can

reversibly deform given a stimulus (e.g., temperature), has good work density, and offers tunability in synthesis, geometry, and the direction of deformation [63, 82, 79]. LCE contains internal directors (mesogens), the orientation of which dictates the direction of the deformation of the elastomer when it is activated by a stimulus (e.g., temperature) [18]. This feature and patternability of LCE in fabrication and design has not been explored within a composite system for the design of rapid locomotion in robots, potentially because of the low actuation speed of this artificial muscle [63, 82].

Artificial muscles made of LCE (as with those made from many other smart materials) also have similar properties to skeletal muscles of mammals [83, 84]; in particular, during contraction, the maximum force that these muscles can exert decreases due to their length-tension relationship [85, 86]. This specific behavior in force-displacement can limit the performance of the actuator for loading a linear spring since the total stored elastic energy is proportional to force applied at the maximum displacement [86]. Previous work focusing on energy storage for jumping has demonstrated that nonlinear springs with variable stiffness (i.e., stiff to soft) store more energy than linear springs [87, 88].

Snap-through mechanisms such as shells are examples of powerful nonlinear springs that offer fast output and energy release to trigger rapid motions. Furthermore, the force-displacement characteristics of these nonlinear springs can be easily customized by adjusting their geometry and material parameters [89, 81, 90]. Previous work has demonstrated the impact of the geometry and material of a shell on its stability [91], which can be classified as monostable (the shell re-inverts or snaps-back once the applied load is removed); pseudo-bistable (it has a small delay before snapping back); and bistable (the shell does not snaps back when the initial applied load is removed, and it requires another load to re-invert the shell). The disadvantage of bistable shells is that they require actuation, physical work, to reach each stable state (i.e., to snapped-through/inverted and snapped-back/re-inverted), thus increasing the overall energy consumption and weight of the system, while pseudobistable shells are challenging to achieve consistently

with standard fabrication processes given the tight range of geometric parameters required [92].

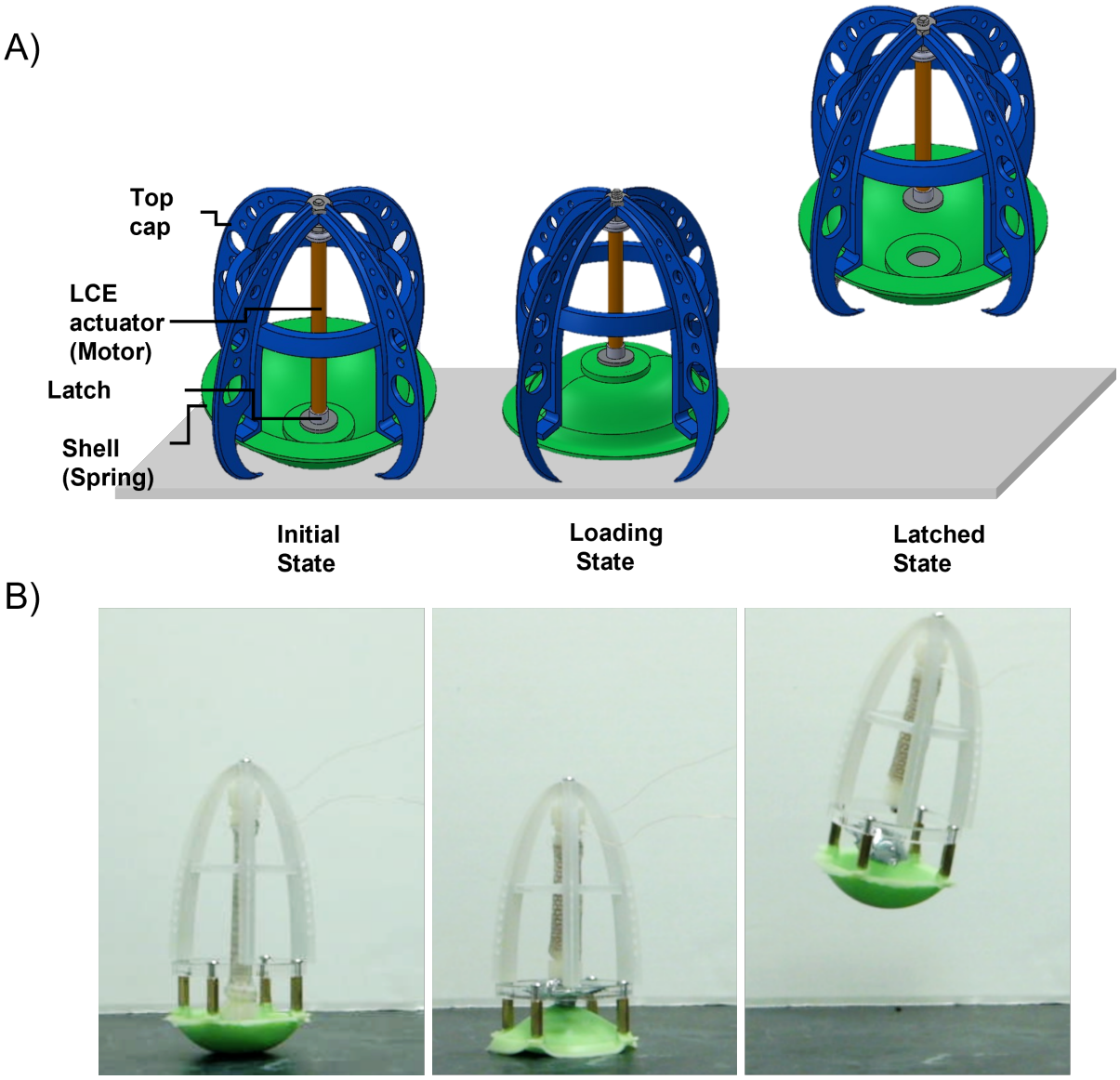

Figure 4.1: Soft Jumping robot with the soft-power amplification system. A) Initial state of the soft robot prior to actuation of the LCE muscle (left); Upon activation of the muscle by joule heating, it contracts, inverting the shell (middle); When the latch is triggered, the muscle decouples from the shell, allowing the latter to snap-back to the ground and propel the robot into the air. B) Images from experiments depicting the steps described in A), in the same order. Reference for scale: the radius of the shell was 30 mm.

In this work, we propose an approach to the design and fabrication of a modular soft robot with a mechanism for amplifying the power output of artificial muscles to achieve rapid motions

like jumping (Figure 4.1). The basic design, similar to previous jumping robots, consists of an actuator (with one side constrained by a stiff part, such as the top cap) that slowly compresses a spring, and a latch which quickly releases the stored energy for jumping. However, to achieve this design with soft components required us to address the key limitation of soft muscles: their inability to apply the large forces required to compress a spring at the large displacements required to store sufficient energy for jumping. To solve this problem, we relied on the nonlinear spring characteristics of a unique kind of soft spring: an elastic spherical shell. By coupling our soft muscle to a monostable shell that exhibited snap-through motion (which decreased the force requirements at larger displacements), and later decoupling the two with a latch, we were able to tune the energy stored for jumping while minimizing the requirements on the muscle. Furthermore, the continuous adjustability of each of these components (as opposed to the discrete options available for typical robotic systems) allowed us to tailor their capabilities to tune the performance of the entire system.

4.2 Design Principles and Fabrication

Our proposed design used a motor-spring-latch system composed primarily of soft components, where the LCE functioned as the motor, the shell as a spring, and the latch as a triggering mechanism to quickly release the shell from the actuator (Figure 4.1 A-B). Once the LCE was joule heated and contracted enough to invert the shell, the latch was subsequently triggered, and finally allowed the shell to snap-back and release the energy stored for jumping. To achieve this behavior and the desired power amplification required for jumping, we selected the geometry of the shell, the LCE muscle, and the latching system accordingly. To manufacture iterations of these components with various capabilities, we took advantage of rapid fabrication approaches, including molding, laser cutting, and printing.

4.2.1 Shell Design and Fabrication for Energy Storage

The identification of the stability and dynamics of shells is an active area of research given its complexity, non-linearity and dynamics during snap-through and back [93]. While there been significant work related to snap-through, most of these studies have focused on thin shells (i.e., $t \ll R$), whereas for thick shells numerical simulations were necessary [91, 92, 94, 76].

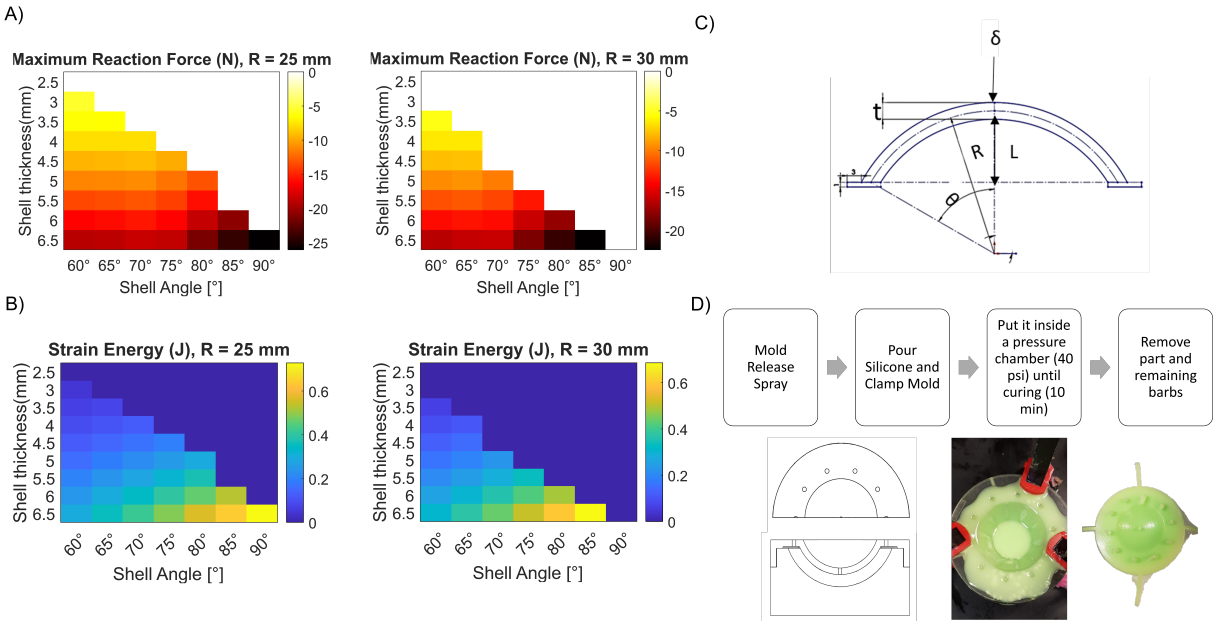

Figure 4.2: Design requirements for energy storage in monostable shells. A) Heat map from simulation of the maximum force required to invert the monostable shells, for various shell geometries (white regions indicate that the corresponding shells are not monostable). B) Heat map of the strain energy of monostable shells when their geometry varies (dark blue regions indicate that the corresponding shells are not monostable). C) Schematic of the tunable parameters used in the simulation, where R is the radius of the shell, fixed per design simulated, δ is the prescribed displacement, L is the vertical distance from the symmetric center of the shell to half of its thickness (t), and θ is the angle of curvature of the shell.

To identify the impact of the geometry of the shell (i.e., radius, thickness, and angle of curvature) on the stability, reaction force and stored strain energy, we used Finite Element Analysis (FEA, Ansys Inc.), (Figure 4.2A). For simplicity and given the relatively slow actuation of the LCE and inversion of the shell, we also assumed [76] a quasi-static simulation of the snap-through. For the dynamics of the system (jumping height of the robot over time), we used a

lumped parameter model (see Appendix B). As in previous work [91], we assumed that the shells can rotate and displace horizontally (roller constraints) on its edges and prescribed a displacement at its center to estimate the reaction force and energy storage of the shells. We used the Arruda-Boyce material model with the Initial Shear Modulus (μ) of 3.5 MPa and incompressibility parameter of 0. To simulate the cross-section of the shell, we used an eight-node axisymmetric quadrilateral element.

In simulation, we identified the desired regime of design parameters for monostability (i.e., the parameters such as geometry and reaction force direction for which the shell would spontaneously revert when inverted) and and the energy stored for each set of viable design parameters (Figure 4.2A-C). For a mesocale robot (i.e., height and length $<$ 15 cm), we investigated the shells within 25 mm - 30 mm radius, with varying thickness (i.e., 2.5 mm - 6.5 mm) and angle of curvature (i.e., 60° - 90°).

For the set of design parameters that we investigated, the monostable shell that stored the maximum energy had a radius of 25 mm, since higher angles led to bistability (Figure 4.2B). However, the trade-off for high energy storage was the force required from the actuator to invert the shell (Figure 4.2A). Since higher actuator forces required larger actuators (and thus large systems), even though a particular shell could store more energy, it did not necessarily result in the best shell for a mesocale system design and actuator.

To fabricate these shells, we used silicone (Elite Double 32, Zhermack, Inc.). We 3D printed the molds (out of VeroClear material on an Object Connex 500, Stratasys, Inc.), added a release coating layer and waited it to dry as instructed by the manufacturer (Ease Release 200 spray, Smooth-On, Inc.), and after mixing the silicone using a centrifugal mixer (for one minute), we poured the solution into the molds. Later, we clamped the molds to guarantee uniform closure and a consistent shape. Finally, we let the solution cure (15-20 min) inside a pressure chamber (at 40 psi, 0.276 MPa) to minimize bubbles in the cured sample (Figure 4.2D).

4.2.2 Design Requirements and Fabrication for Actuation and Latching

In this section, we describe a methodology that enables the tunability of the LCE geometry, and its relationship between the shell, and latching system. The performance of the system is dependent on the integration and interaction between these components and the LCE. Depending on the size of the system and the desired jumping height, the relationship between the parameters of the LCE, shell and latching can be used to achieve those design requirements. For instance, the actuator needs provide enough force and contraction to invert the shell until its snap-through position (Figure 4.3A, iii-iv). The latching system needs to hold enough load during the inversion of the shell and when its inverted (Figure 4.3A), so it does not release from the shell prematurely (less energy).

The geometry of the LCE and its actuation strain are also parameters necessary to consider for designing the top cap (stiff component). The height of the top cap is a function of the shell's geometry (radius, theta) and the LCE contraction, (Figure 4.3B-C). Thus, the height of the top cap can also be used as a design constraint since its weight increases with the geometry of the LCE and shell, and overall increasing the size required for a mesocale jumping robot.

To achieve the necessary force and contraction necessary to invert the shell, we need to be able to tune the cross-sectional area of the actuator and its length, respectively. However, to achieve high force, thick (i.e., $>$ 1.5 mm) and long actuators (i.e., $>$ 15 cm) would be required which would compromise the space and size of the actuator for a mesocale soft machine (height and length $<$ 15 cm). To address this actuation challenge, we developed an approach to fabricate LCE muscles that enabled us to continuously adjust their capabilities by taking advantage of the patternability of LCE. By preparing the LCE as a sheet [82, 63], we were able to easily adjust their cross-section area (thickness and width) by molding the desired thickness and laser cutting the desired length and width (Figure 4.4C). To satisfy the constraint on the size of the muscle, we took advantage of the compliance of the LCE and rolled the sheets into a tubular shape.

For the fabrication of the actuator, the LCE sheet was synthesized using the same process

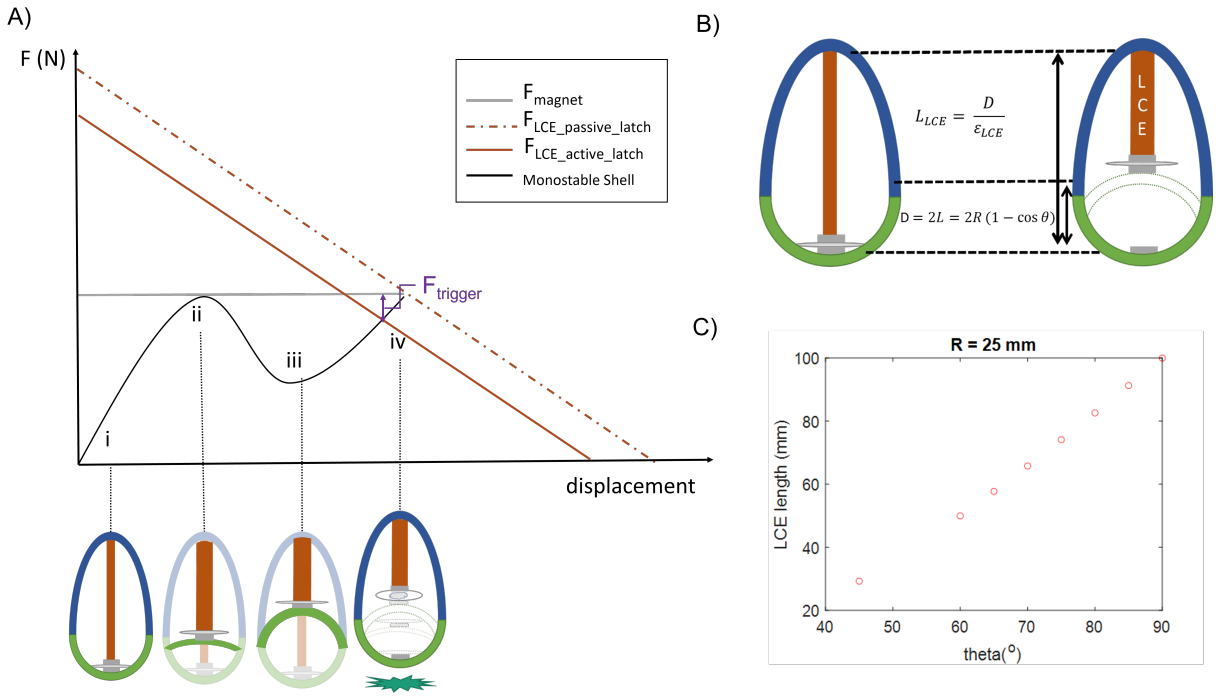

Figure 4.3: Design requirements for actuation and latching of the system. A) Representative plot indicating the force displacement curve of the monostable shell and the plot of the LCE based on its block force and free displacement values. i) represents the initial configuration of the shell (non-inverted); ii) its marginal inversion position; iii) the snap-through (inverted) state, and iv) triggering region past the snap-through region. B) Kinematic constraints on the top cap length as a function of the geometry of the LCE and shell. C) Representative plot demonstrating the minimum length necessary for the LCE given an actuation strain of 0.4, and varying curvature angles of the shell.

we used in previous work [82, 63]. For the heating layer, we used copper tape attached to a gel pack carrier and defined the shape of the heater traces using a custom ultraviolet (UV) micromachining system (Figure 4.4C). Once patterned, we removed the copper layer and used a water soluble tape to transfer in onto the LCE sheet. After dissolving the tape with dionized water (DI), we then sandwiched the heater layer with another layer of polydomain (loosely crosslinked) LCE. We then passed a glue (i.e., super glue, gorilla) on the edges of LCE to roll and bond the LCE sheet using two acrylic rings as guides, forming a tubular-shaped LCE actuator. Later, we stretched the tubular actuator and cured it under UV light for an hour. We used a glass rod to transmit the UV light inside of the rolled actuator to make sure the interior of the actuator was

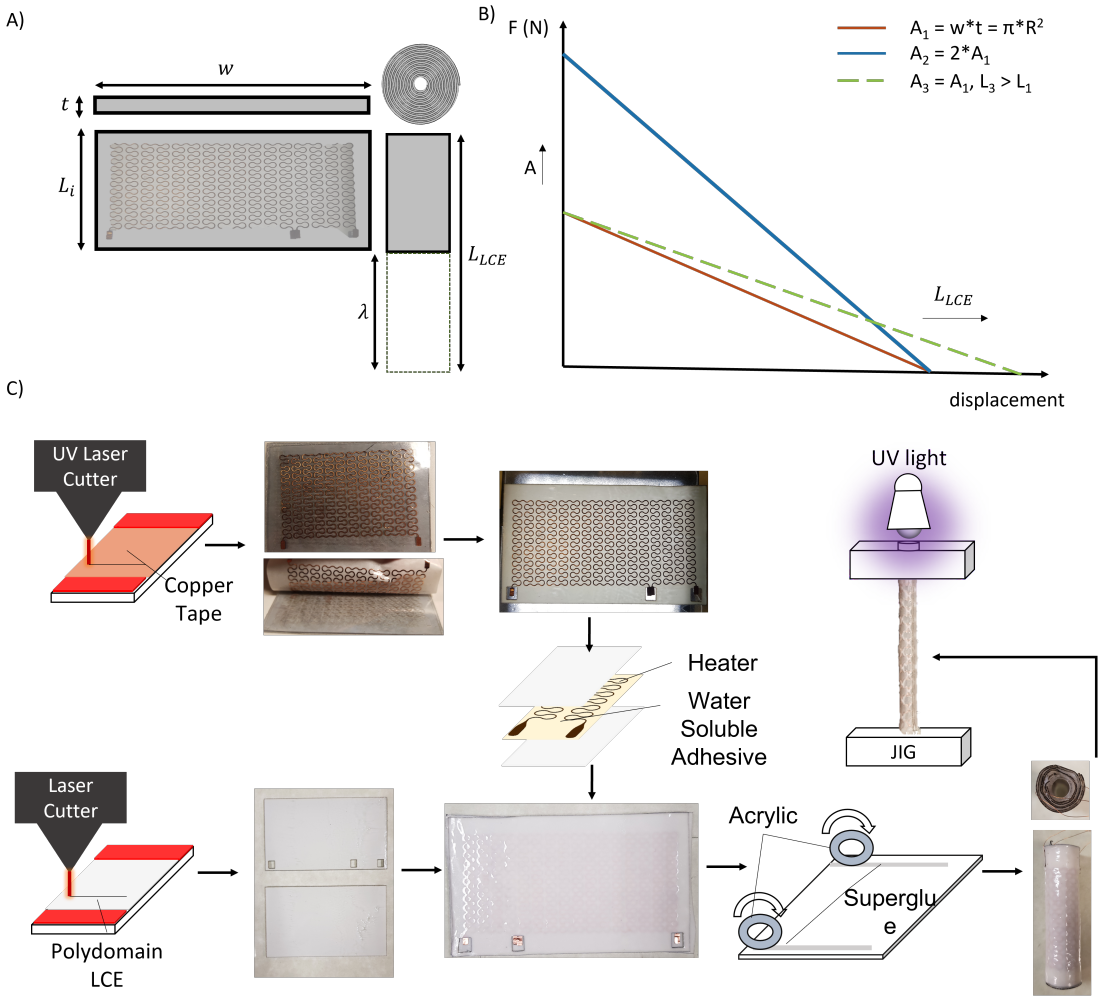

Figure 4.4: Design guidelines and fabrication process for rolled LCE actuators. A) Design parameters used to tune the geometry of the LCE. B) Representative plot indicating the tunability of the rolled actuator force-displacement characteristic, based on the dimensions of the initial LCE sheet. C) Process of fabrication of the rolled actuator.

fully cured.

For the latch, it was important to achieve a fast release [80] to avoid inefficiency in energy conversion. Being compact and reversible was also important so the latch did not compromise the weight, actuation performance (tied to its geometry, Figure 4.3A-B) and enabled reversible latching. To enable the reversibility and repeatability of the system, the latch should also be able to return to its original position (i.e., self-alignment), connecting the actuator with the shell. To fulfil the latching requirements of self-alignment, we used high-temperature neodymium magnets

according to requirements necessary from the selected shell and actuator. To quickly trigger the decoupling of the actuator from the shell with a compact latch, we used a pouch filled with liquid with a low temperature boiling point (Figure 4.3A, iii- iv). Once the LCE provided enough force and displacement to invert the shell, the liquid-phase pouch motor was heated, causing the liquid to evaporate and the pouch to inflate, separating the magnets of the latch. The advantage of using this active latching system was that it reduced the force required from the actuator at a large displacement to separate the magnets. The result was a significant reduction in the actuation requirements. This approach provided a control on when to trigger the shell, and minimized the force requirements on the actuator if the system relied only on a passive latch (i.e., on the attraction force of magnets) (Figure 4.3A, iv).

For the fabrication of the pouch, we followed the steps in previous work [95]. In our case, we used commercially available anti-static circuit bags as the layers for the pouch (25 mm x 25 mm), then cut and partially sealed them, to later insert the low boiling point (acetone, $\sim 80\%$) and completed the sealing process with a heat sealer.

4.3 Results and Discussion

4.3.1 Tunable Jumping Heights with Shells

To validate our model of the relationship between the shell dimensions and the jumping height of the robot (see Section *Shell Design and Fabrication for Energy Storage*), we tested two shells designs with the same radius (30 mm) but different thicknesses (3.5 mm, 6.5 mm) and angles of curvature (60°, 65°; see Figure 4.5). For this experiment, we emulated the behaviors of the artificial muscle and latch with a fishing line connecting the inverted shell to the top cap. To allow the shell to invert, we bonded the base of the top cap to the perimeter of the shell with soft feet (same material as the shell) using a bonding material (PolyKit, ttbonding; see Figure 4.5A). We manually inverted the shell and affixed the fishing line to the top cap with a screw. Once

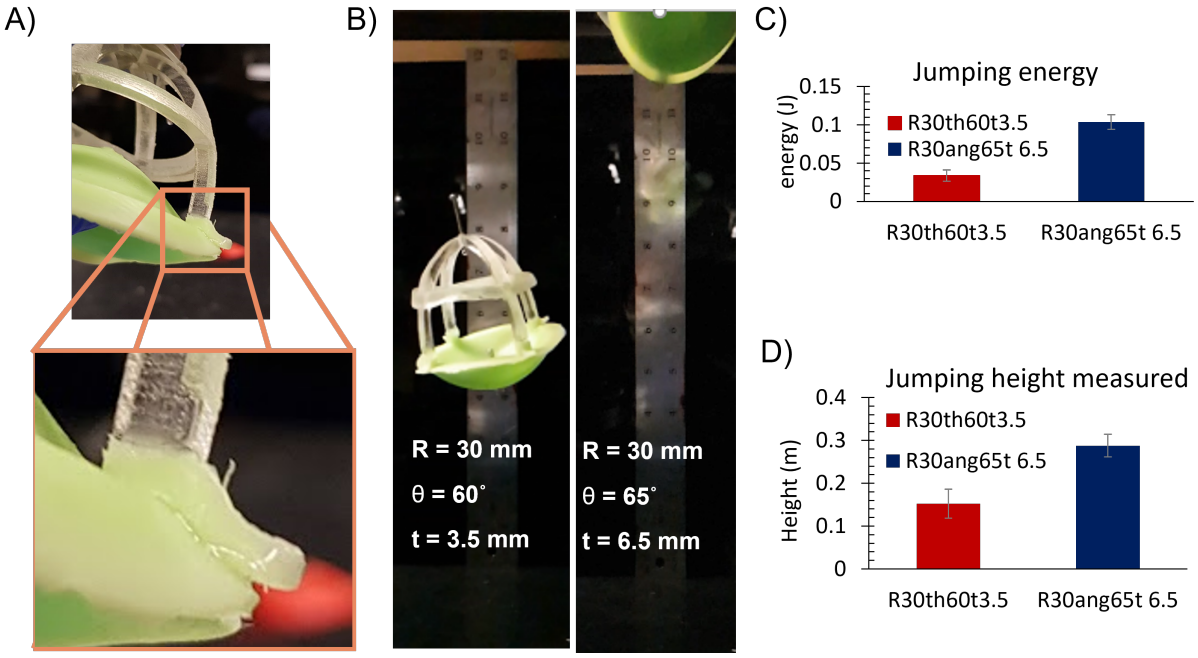

Figure 4.5: Demonstration of a jumping shell with a top cap and soft feet. A) Demonstration of a molded soft foot and its successful bonding between a rigid layer (Object Connex 500, VeroClear) and the shell. B) Snapshots of the jumping shells with different geometries and consequentially jumping heights. C) Comparison between the performance of these shells based on energy released.

inverted, we triggered the shell using a heat gun to melt a fishing line, simulating the action of the latch. This trigger allowed the snap-back of the shell to the ground.

The shell with thickness 3.5 mm and angle 60° generated a potential energy (total mass*gravity*height) and jumping height of 33.6 $\pm$ 7.4 mJ and 150 $\pm$ 36.6 mm, respectively. Whereas the shell with 6.5 mm thickness with an angle of 65° can achieve an energy of 103.8 $\pm$ 9.5 mJ and jumping height of 287.9 $\pm$ 26.4 mm. These results supported our hypothesis, demonstrating that by changing the geometry of the shell (almost doubling the thickness and slightly incrementing the angle) can proportionally impact the energy released and jumping height. Furthermore, we validated the approach of using a point force (to be generated by a muscle) to invert the shells for energy storage to enable lightweight and self-contained machines for rapid motions.

4.3.2 Actuator Characterization and Shell Selection

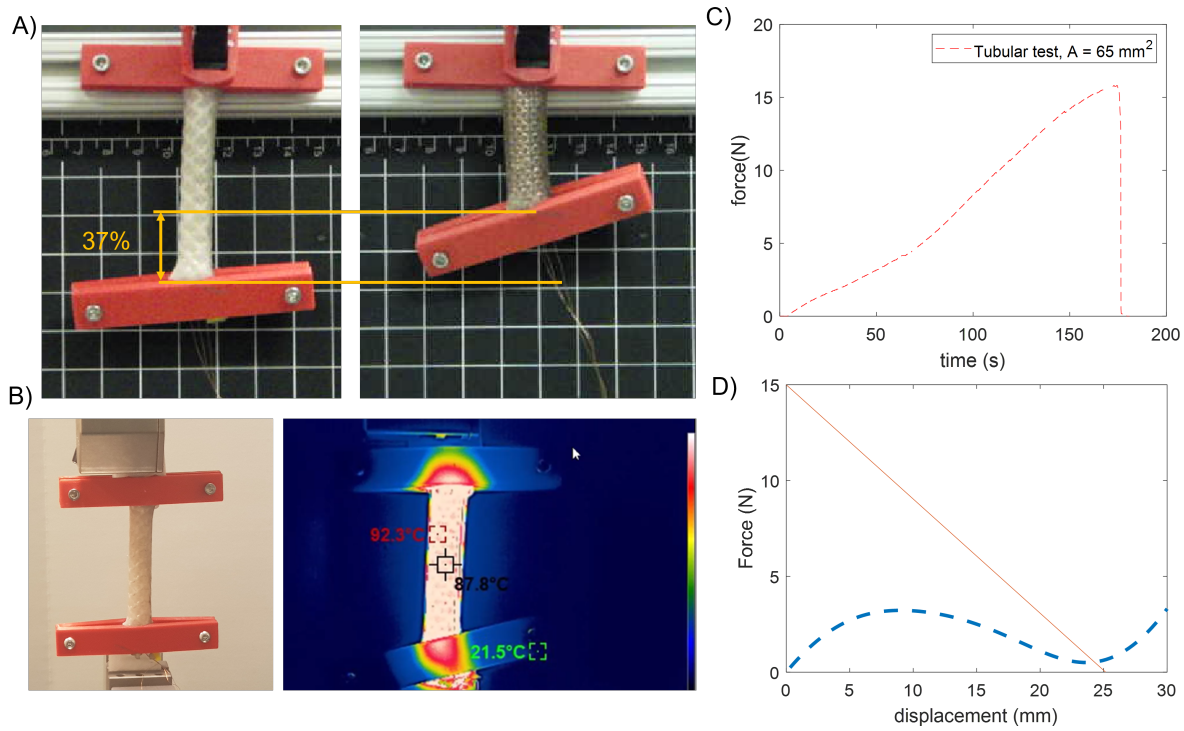

Figure 4.6: Characterization of the rolled LCE artificial muscle. A) Actuation strain of the rolled LCE actuator. B) Block force setup, and thermal image (HT-H8, Hti-Xintai) of the LCE at the point of failure. C) Maximum force measured from the 68 mm sample before failure. D) Force-displacement curve of the LCE actuator (orange line) based on empirical data from block force and strain, and of the simulation of the shell (blue dashed-curve).

Given that the height of the top cap was dependent on the length of the actuator, we constrained the maximum length for a single LCE actuator to be $<= 70$ mm to limit the overall height of the robot. To measure the maximum actuation force of the LCE actuator (i.e., cross-section area, 65 mm^2) with similar constraints as in the robot (clamped/fixed edges), we powered our system (9W from the power supply) until failure. We constrained its displacement of the actuator with two 3D printed clamps designed to accommodate the muscle, affixed to a load cell (250 N range, Mark-10 Corp.) and observed a maximum blocked force of 15.8 N before failure by delamination from clamps at approximately 92°C (Figure 4.6B-C). To measure the maximum actuation strain of the muscle, we fixed one side of the actuator and allowed the other

to contract and displace freely when Joule heated, until $\sim$ 110°C. The maximum actuation strain we measured for this sample was about 37 % (Figure 4.6A).

Considering these parameters, we can select shells that can be inverted by this actuator. Based on simulated results (Figure 4.2A-B), we can see that the shell with 30 mm radius, 3.5 mm thickness and 60° can be actuated with this actuator with the possibility to be triggered with least 4 N with an active latching system (Figure 4.6D). This result highlights the advantage of tuning other parameters to not rely mainly on the performance of the actuator. For instance, this actuator would no be able to effectively invert this shell with just a passive latching system (Figure 4.3A).

4.3.3 Soft Power Amplification System Demonstration and Performance

Based on our design guidelines, we used our power amplification system to build a jumping soft robot. To simulate a case with payload (with mass of $\sim$30 g, approximately the mass of two 3.7 V, 1300 mAh lithium polymer batteries), we added a modular part made of acrylic attached with stand-offs between the top cap and flexible feet on the shell. This part also simplified the assembly of the actuator and top cap while providing a modular way to adjust the height of the robot for the jumping test (Figure 4.7A).

To validate our design concept, we powered the rolled LCE actuator ($\sim$ 9W) until inverting the shell, and when fully inverted we heated the liquid-vapor activated pouch with a heat gun to separate the connecting magnets between the shell and actuator (Figure 4.7B). The triggering of the latching system and the resulting rapid motion of the snap-back of the shell were recorded with a high-speed camera (Phantom camera, Vision Research Inc.).

Once inflated, the pouch successfully decoupled the LCE and the shell, and allowed the latter to snap back to its original shape and propel the robot into the air to achieve a height of 55.6 mm at 0.49 m/s (average speed from take-off to maximum height) and potential energy (mgh) of 35.7 mJ with a total mass of 65.3 g. This total amount is five times the weight of the shell with mass of 13 g.

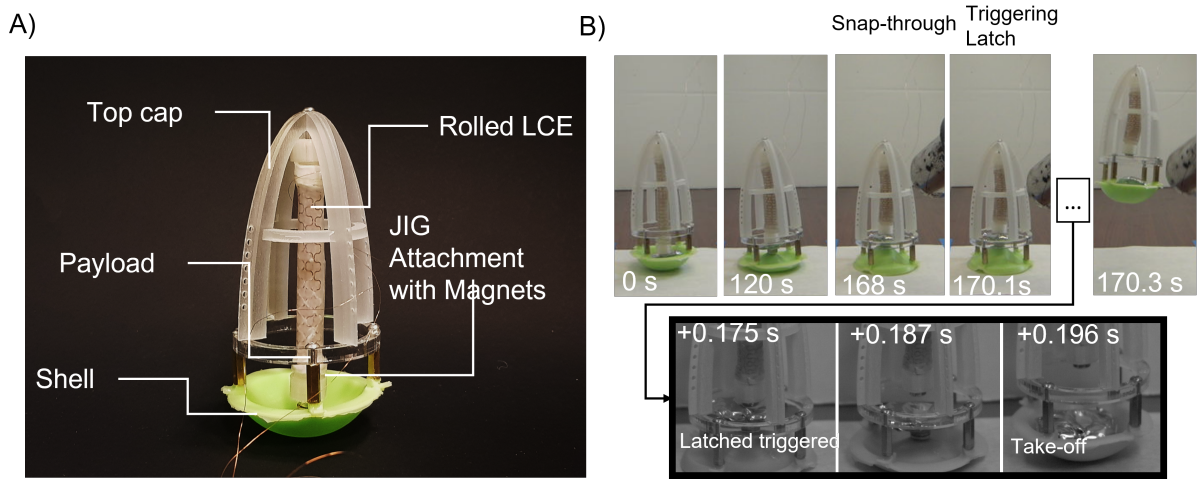

Figure 4.7: Demonstration of the soft power amplification mechanism for a jumping robot. A) Image of experimental system with key components labeled. B) Top: Frames from video of the LCE muscle inverting the elastic shell until snap-through occurred (0-168 s). Bottom: Frames from high speed video of the triggering of the latching system, showing the rapid snap-back of the shell once it is decoupled from the LCE muscle.

The work output of the LCE muscle as it inverted the shell was done at an average mechanical power of 0.2 W over 168.1 s (assuming the conservative case of no energy losses). Whereas with the average power output of the shell during jumping was 1.7 W over 20.7 ms (measured from the triggered detachment of the latch to the take off time of the robot). Thus, the power amplification ratio of our system was 8,199 and the energy efficiency was 73% (comparing the estimated strain energy stored in the shell right before triggering the latch, 49.8 mJ, from simulation with the final potential energy of the system at the apex of the jump). This substantial amplification of the power output of the LCE muscle enabled the robot to achieve rapid motion without compromising the advantages of the patternable and continuously variable dimensions of the LCE based soft actuator.

Our modular and soft power amplification system also generated a specific power of 26.4 W/kg, which is higher than values measured in previous work that relied on electrically powered dielectric elastomer [75] or shape memory alloy for actuation [6]. This powering method provides an accessible integration for autonomous mesocale systems (e.g., battery and sensors).

However, previous work relied solely on the performance of the actuator itself [79], the snapping of the shell [76], or a latch mediated system [75, 6], and did not account for payloads normally required for tethered systems [75, 76]. Thus, our soft power amplification mechanism has the potential to enhance rapid motions while leveraging the patternability of artificial muscles, and represents a key step towards mesocale, modular and untethered soft jumpers.

4.4 Conclusion

In this work, we demonstrated an approach to designing modular soft mechanisms using the snap-through of elastic shells to amplify the power output of soft artificial muscles for rapid motions like jumping. Using this methodology, we can estimate the performance of the system (e.g., jumping height and power amplification) given a set of design parameters for the shell (i.e., radius, thickness, angle of curvature), and actuator (i.e., cross-section area, length) when interacted with an active latching system. With our results, this approach also enables a way to solve the inverse problem (i.e., given a desired jumping height, we can select a shell and actuator design). Additionally, we proposed a new methodology to pattern and fabricate compact, high-force, electrically actuated LCE actuators with continuously variable performance (i.e., in terms of their blocked force and free displacement). Finally, we demonstrated the performance of our soft power amplification system with a mesocale jumping robot.

Our soft jumping robot was able to achieve a jumping height, specific power, and energy conversion efficiency comparable to previous work [75, 6, 76]. These comparisons are based on systems that used soft actuators with similar attempts to enhance the actuation for jumping. To our knowledge, this work is the first to contribute with a modular approach that enables the performance for jumping and rapid motions.

The opportunities for investigation in future work building on this work are based on the trade-off on the synthesis of artificial muscles such as LCEs (high actuation stress but low strain or

adherence to other layers), as well as the constraint on the size we could manufacture stretchable circuits in this work (70 mm x 60 mm). Nonetheless, building on these results, we enabled new opportunities and baseline towards rapid motion of soft robots using artificial muscles such as LCEs. For example, we used a heat gun to activate and validate our latching system, but it is possible to explore the control of the latching time and therefore its jumping height by integrating a flexible circuit onto the pouch. Furthermore, by exploring different cap designs for lightweight and self-righting, or even parallel actuation to explore shells that can store higher energy and achieve jumping heights than the ones we currently explored to validate our system. Finally, given our current results, we enabled a promising opportunity to achieve mesocale and untethered soft-jumpers, in which it is possible to investigate the tunability of the jumping height by also controlling the contraction of the artificial muscle.

Chapter 4, in part, is currently being prepared for submission for publication. **Minori, A.F.**, Jadhav, S., Chen, H., Fong, S., Tolley, M. T.(2021) "Soft Power Amplification System for Jumping using Patternable Artificial Muscle and Snap-through of Shells". The dissertation author is the primary investigator and author of this paper.

Chapter 5

Conclusion

This thesis proposed new methodologies to achieve patternable actuation for mesocale self-folding and soft robots by leveraging the advantages of smart materials such as LCEs with composites and mechanisms towards ubiquitously lightweight, compact, and deployable robots. The second and third chapter focused on self-folding robots with the exploration of the literature gap on reversible self-folding composites. The second chapter explored the research gap towards reversible self-folding origami composites hinges and validated the hypothesis that by constraining a uniaxailly aligned LCE (i.e., straightforward synthesis method) with a stiff layer, we can achieve and predict the reversible self-folding angle of the composite. The third chapter, building on the second chapter, leveraged the patternability of the LCE to achieve with a single uniaxially aligned LCE layer modular and complex self-folding machines. Finally, the fourth chapter of this thesis focused on the challenge towards utilizing LCEs when rapid motions are necessary. To fulfill this need, that chapter proposed a modular soft power amplification design that leverages the advantages of LCEs for actuation and can still achieve rapid motions towards mesocale soft jumping robots.

5.1 Open Questions and Future Directions

By identifying how to take advantage of smart materials to actuate self-folding and soft robots using mechanisms and a rapid fabrication approach, this research has also enabled future opportunities that can be explored beyond just robotic actuation applied for locomotion. In particular, these are some of the emerging research and future directions in the field that can take advantage of the contributions from this thesis:

- Sustainable systems: in this thesis we demonstrated ways to achieve mechanisms that can enhance the performance of a smart material for actuation. However, a topical question and research direction is how to leverage the stimuli responsiveness of smart materials and their inherent self-sensing properties to achieve sustainable robots and devices.

- Ubiquitous computing: another interesting and emerging research direction is the exploration of programmable materials to enable the mechanical programmability of devices to decrease the computation and control required in robotics systems.

- Interactive interfaces: by leveraging the advantages of rapid fabrication methods and soft and programmable materials, there is an emerging opportunity to develop more inconspicuous and interactive devices that are accessible and can easily interact with humans and environment.

Appendix A

Supplemental Materials: Reversible actuation for self-folding modular machines using liquid crystal elastomers

A.1 Derivation of the Static Load Model

For our static model, Figure A.1C, we assume: i) a rectilinear contraction of the LCE; ii) ideal rotational joints; iii) a symmetric Sarrus design; and iv) a constant load (W) on the top of the mechanism. Where F_{LCE} is the maximum LCE force at the folding angle θ, and F_{ij} is the reaction force onto its respective reaction force of bar i onto bar j.

In Figure A.1D, we find the following relationships from the force balance on link two:

$$F_{LCE} = F_{32}cos\theta + F_{12}cos\theta \tag{A.1}$$

$$F_{32}sin\theta = F_{12}sin\theta$$

$$F_{32} = F_{12} \tag{A.2}$$

Plugging Equation(A.1) into Equation(A.2), we get:

$$F_{LCE} = 2F_{12}cos\theta \tag{A.3}$$

From the force balance on link one, we find:

$$F_{21} = F_{51} \tag{A.4}$$

$$W = F_{21}sin\theta + F_{51}sin\theta$$

Which from Equation (A.4), reduces to:

$$F_{21} = F_{12} = \frac{W}{2sin\theta} \tag{A.5}$$

Plugging the Equation(A.5) into Equation(A.3), we get:

$$W = F_{LCE}tan\theta \tag{A.6}$$

A.2 Crawler Locomotion Model

We hypothesized that the primary locomotive mechanisms in the crawlers with friction pads are captured by a mass-spring-damper (MSD) system governed by the assumptions made in section *Design of Self-Folding Composites with LCE*. We then developed the equations of motion for this MSD system (see Equations A.7-A.9).

$$m\ddot{x}_1 = F_{k_1} + F_{c_1} \tag{A.7}$$

$$m\ddot{x}_2 = F_{k_2} - F_{k_1} + F_{c_2} \tag{A.8}$$

$$m\ddot{x}_3 = -F_{k_2} + F_{c_3} \tag{A.9}$$

Where:

$$F_{k_1}(t) = k_1(x_2(t) - x_1(t) - dl_1(t)) \tag{A.10}$$

$$F_{k_2}(t) = k_2(x_3(t) - x_2(t) - dl_2(t)) \tag{A.11}$$

The terms dl_1 and dl_2 are the equilibrium lengths of the springs and are functions of the LCE strains in each module, (ε_i (t)):

$$dl_1(t) = \frac{L_o\varepsilon_1(t)}{2} + \frac{L_o\varepsilon_2(t)}{2} \tag{A.12}$$

$$dl_2(t) = \frac{L_o\varepsilon_2(t)}{2} + \frac{L_o\varepsilon_3(t)}{2} \tag{A.13}$$

We used a Coulomb friction model to describe the sliding between the modules of the crawler and the ground. The Coulomb friction, as the damping in the system, changes depending on friction conditions:

$$F_{c_i}(t) = \begin{cases} F_{i_+}, & \text{if } \dot{x}_i > 0 \\ 0, & \text{if } \dot{x}_i = 0 \\ F_{i_-}, & \text{if } \dot{x}_i < 0 \end{cases}$$

Where i is the index for each module and F_{i_+} and F_{i_+} change in time based on the friction conditions assumed above.We assume directional dependence of frictional forces on, where positive velocities induce lower friction forces (i.e., $F_{i_+} = F_{\text{low}},\ i = 1,3$) and negative velocities induce larger friction forces (i.e., $F_{i_+} = F_{\text{high}},\ i = 1,3$). To compare our model with experimental

results, this frictional anisotropy is only applied on modules one and three because only these modules on the physical crawler had gecko-inspired adhesive friction pads. Module two was left bare and we model its friction with force coefficients $F_{2_+} = F_{2_-} = F_{low}$.

A.3 Simulation of the Crawler Locomotion

We used MATLAB Simulink to implement our model and to simulate the locomotion of our crawler with pads (block diagram in Figure A.3). In these simulations, we estimated some model parameters using approximate values seen in previous work. The stiffness of the springs, k_1 and k_2, between the masses was estimated to be 200 N/m from the baseline Young's modulus value of PDMS [96], which is similar to that of LCE at its isotropic state with a similar cross-linking density [46]. For the coefficients of friction of the directional friction pads, we modelled the design with gecko-inspired adhesive that resulted in the best locomotion performance (see Figure 8). We considered the coefficient of friction values of μ_{high} = 1.9 (when the gecko pad is in full contact with the ground) [67], and μ_{low} = 0.8 (when the foam and silicone backing of the gecko pad are in contact with the ground) [97]. Since both the foam and silicone touch the ground when the crawler slides forward, we assumed that the frictional effect of silicone would be more significant than that the foam, and selected an approximate value for the simulation using the coefficient of the former.

As input for our system, we approximated a strain curve from our experimental results with the Sarrus module with an eighth-order Fourier series of the form:

$$\varepsilon_{input_i}(t) = \sum_{n=0}^{8} a_n cos(w\ n\ (t - t_{shift_i})) + b_n sin(w\ n\ (t - t_{shift_i})) \tag{A.14}$$

The fitting curve function [Equation(A.14)] has the following coefficients: $a_0 = -0.1714$; $a_1 = 0.05498$; $b_1 = -0.1553$; $a_2 = 0.04284$; $b_2 = -0.006938$; $a_3 = 0.02076$; $b_3 = -0.006245$; $a_4 = 0.01196$; $b_4 = 0.006141$; $a_5 = 0.004833$; $b_5 = 0.002548$; $a_6 = 0.002382$; $b_6 = 0.002886$;

$a_7 = 0.001363$; $b_7 = 0.001266$; $a_8 = -3.252e-05$; $b_8 = 0.0009379$; $w = 0.0538$; and t_{shift_i} represents the time-shift of i^{th} modules actuation cycle, and were set to mimic the time differences of 0, 10, and 27 for modules one, two, and three, respectively, of the experimental crawler. The output of our simulation for the gait cycle from the experiments with the crawler is shown in Figure 8C.

A.4 Gecko-Inspired Adhesives and Manufacturing Approach

To turn the repeating isotropic gait of the crawler into a forward motion, we use a one-way friction foot with a layer of gecko-inspired adhesive. The gecko-inspired adhesive is comprised of 20 μm x 50 μm silicone micro-wedges [68]. This type of microfeature offers several key properties such as low detachment forces, long lifetime, and adhesion-controlled friction. These adhesive microstructures have been used for climbing [98, 99], gripping [100], and perching [101]. Recently work has focused on the property of adhesion-controlled friction to make new kinds of grippers [102, 103] and improve robotic locomotion [104]. This adhesion-controlled friction is important for this application given the low mass of the crawler. However, this type of microstructure does not exhibit a strong preference between the forward and backward directions and therefore does not work as an anisotropic friction device without modification.

Prior work has introduced the desired directionality into the adhesive by adding periodic undercuts to the wedges that make a flap, such that when loaded in the anti-preferred direction, this loose flap prevents most of the microfeatures from engaging [105, 106]. This process of modifying the microstructure for anisotropic friction requires additional complexity in the manufacturing process and has not been explored for robotic feet during a non-planar gait cycle. To simplify the manufacturing process and add robustness to the angle of the foot, we adapted the flap approach to a larger size scale (Figure A.7). By leaving 3 mm of the gecko adhesive unattached to the foot we create a macroscopic flap that can be made using traditional laminate

manufacturing techniques. The foam layer helps engage more of the adhesive when the foot is pulled in the preferred high-friction direction, and acts as a low friction surface when the foot is pulled in the anti-preferred low friction direction.

A.4.1 Gecko Pad and the Crawler Traveling Wave Behavior

We observed a snapping of the second module to the ground in all of our gecko-inspired pad samples. As described in the Crawler Locomotion with Directional Friction Pads section, this snap behaviour was more dramatic when the third module was slightly off the ground. Upon touching the ground, the third module allowed the gecko flap position to reach its marginal state and to quickly snap backwards to its low-friction side, (see Figure 7C(iv) at 86 s and 87 s and Movie S4). The GTFP 2, also had the snapping but the third module did not lift off the ground and the gecko did not flap backwards but just slid its tip forward (Movie S5). The second module, dropped when the first module on the second cycle started to actuate, forcing the second module to return to the ground. We observed the same behaviour with the GRFP, with the difference that the rectangular foam interacted more with the surface than the other pads with triangular foam. The only time the gecko did not prevent backward motion was when the second module dropped to the surface and relaxed at an angle. Consequentially this action made the first module to rotate counterclockwise and the gecko pad to be at an angle with the surface, therefore decreasing the frictional force.

A.4.2 Movie S1

Video demonstrating the reversible self-folding of a laminate Sarrus mechanism, and the Sarrys as a base for orgiami-inspired designs such as a crane and Lily flower. Movie S1.

A.4.3 Movie S2

Video demonstrating the ability of the Sarrus module to withstand vertical loads. Movie S2.

A.4.4 Movie S3

Video of the crawler locomotion without pads with different gaits analagous to an earth-wom locomotion. Movie S3

A.4.5 Movie S4

Video of the crawler with directional friction pad moving similarly to a caterpillar. Movie S4

A.4.6 Movie S5

Video of the crawler locomotion performance with different direction friction pads: Rubber Rectangular Foam Pad (RRFP), Gecko Rectangular Foam Pad (GRFP), Gecko Triangular Foam Pad Crawler two (GRFPC2), and Gecko Triangular Foam Pad Crawler one (GRFPC1). Movie S5

A.4.7 Movie S6

Video of the Sarrus crawler attached to a surface with magnets moving downwards. Movie S6

A.5 Supplementary Figures

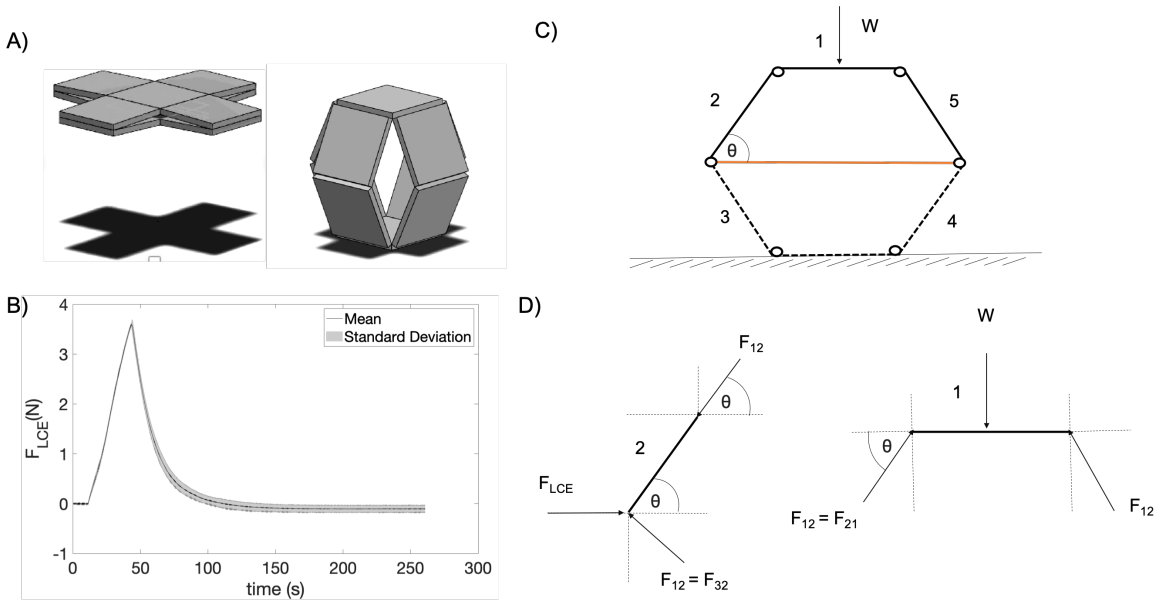

Figure A.1: Sarrus mechanism and static model to withstand vertical load with the LCE. A) Sarrus mechanism in its flat and folded position. The mechanism converts the unidirectional actuation of the LCE to folding along axes perpendicular and parallel to the actuation. B) Force measurements of the LCE during the actuation stress test, showing the average maximum force produced during the experiments. C) Schematic of the cross-section area of the symmetric Sarrus withstanding a load (W), indicating all the links of the mechanism. D) Body diagram of the link two and one for the force balance analysis.

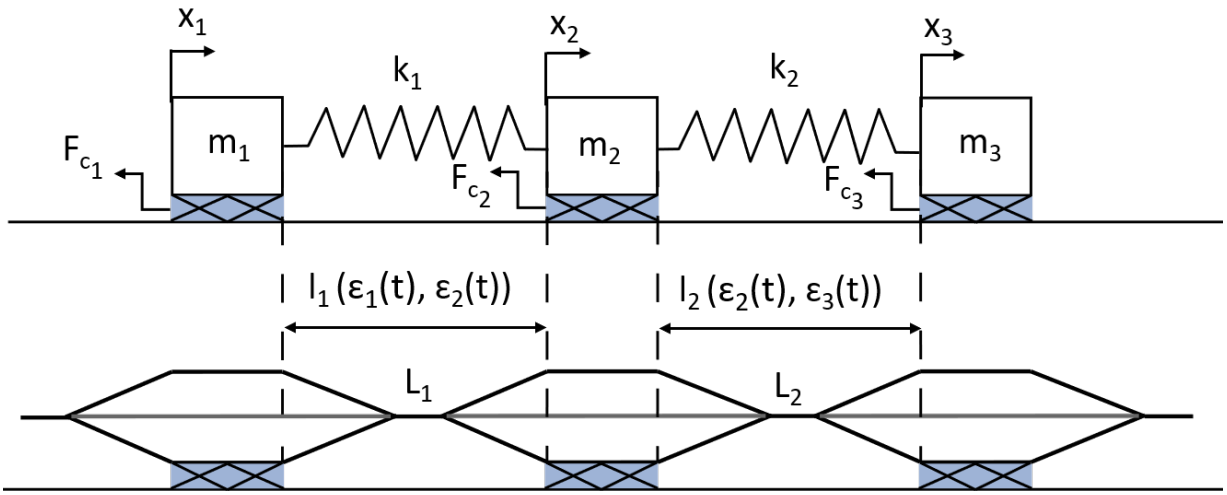

Figure A.2: Schematic of the MSD system simplifying the geometry of the crawler made of Sarrus modules with directional friction pads, in which the MSD displacement is a function of the strain of the LCE (l_1 and l_2) with respect to time and the geometry of the mechanism such as the links of the Sarrus module and its connecting link (L_i).

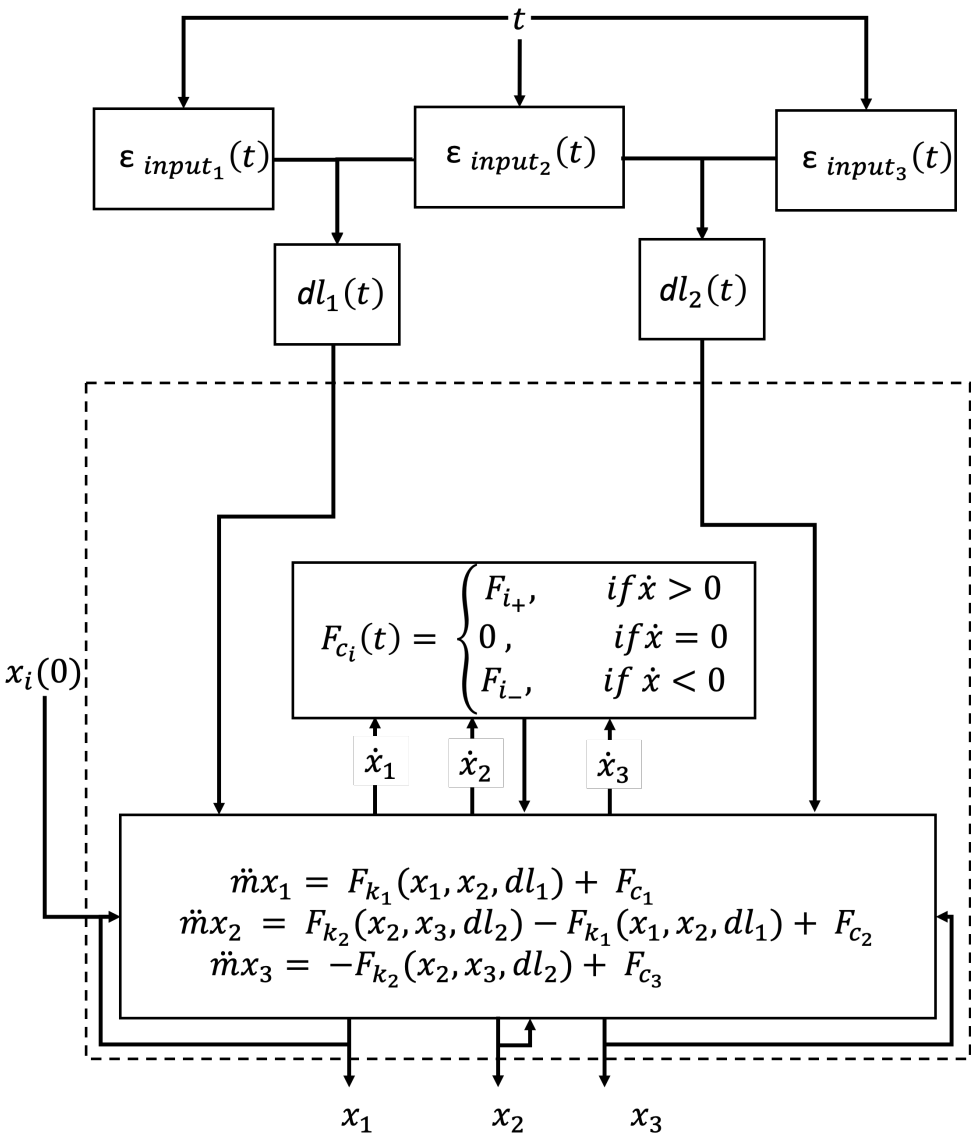

Figure A.3: Block diagram of the simulation, where each block represents the functions of the model with their respective variables, and the arrows indicate the input and output for each block for the crawler with pads.

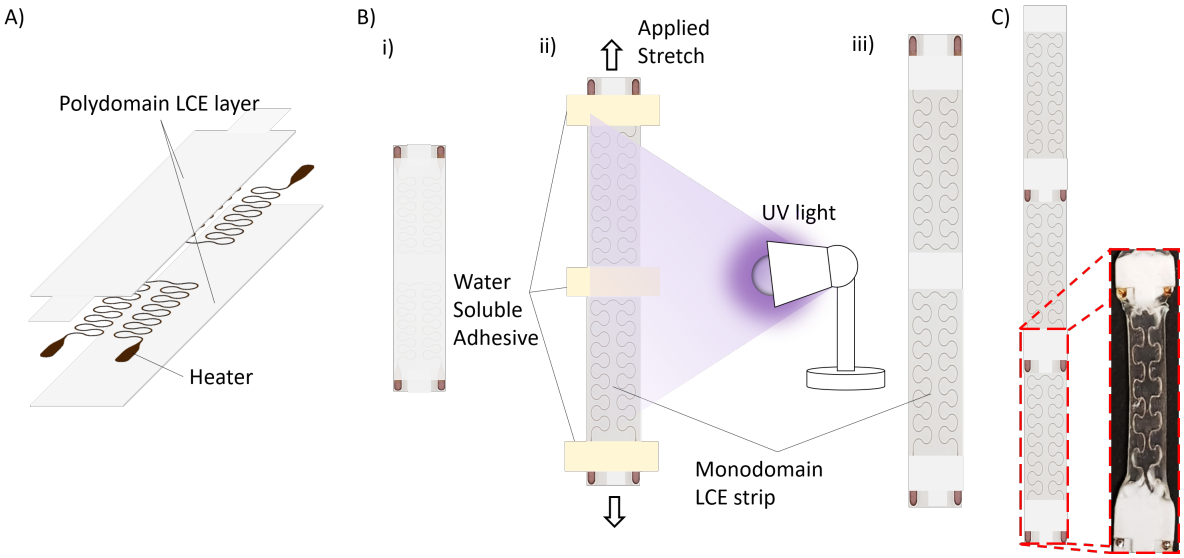

Figure A.4: Assembly of a single layer of LCE actuator for distributed actuation. A) Exploded view of a single layer of LCE for the distributed actuation of two modules, see Figure 3. B) Assembly and orientation (training) of the LCE actuator. i) Assembled LCE actuator in its polydomain state. ii) Training of the LCE actuator by stretching only the regions desired for actuation, constraining the others with soluble adhesive, and using UV light for fixing the LCE actuation direction, mesogen orientation. iii) Single layer of the LCE actuator for the independent actuation of two modules. C) LCE actuator layer for the independent actuation of three modules, with a zoom in of one of its sections showing its corresponding area in a sample.

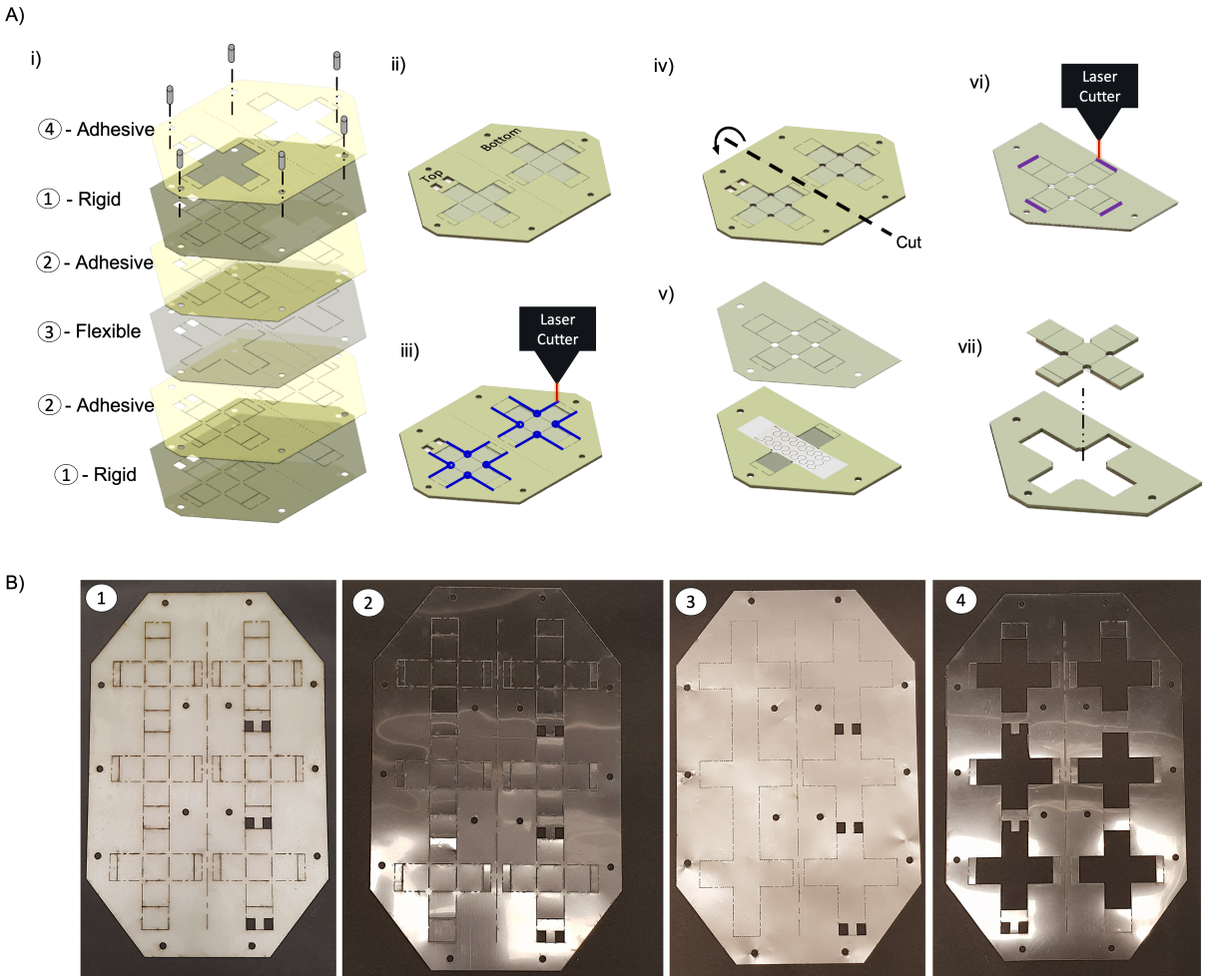

Figure A.5: Assembly of the Sarrus based composites. A) Assembly steps of the Sarrus module. i) Exploded view of the laser cut layers and its bottom-up assembly steps. ii) Composite after aligning and assembling the layers resulting in a symmetric top and bottom layers of the Sarrus composite. iii) Release layer step for future module detachement. iv) Cut of half of the composite to generate both halves of the module layers, top and bottom. v) Alignment and assembly LCE and the bottom half of the Sarrus onto its top half. vi) Final release step of the composite. vii) Detachement of the Sarrus module composite. B) Photos of the four different design layers used for the Sarrus module composite of the crawler, which follows the same assembly steps as a single Sarrus module. 1) Rigid layer with the top and bottom halves design patterns for the crawler assembly. 2) Adhesive layer that connects the rigid layers with the flexible layers. 3) Flexible layer. 4) Final adhesive layer to sandwich the LCE actuator layer onto the top and bottom half of the Sarrus-based crawler.

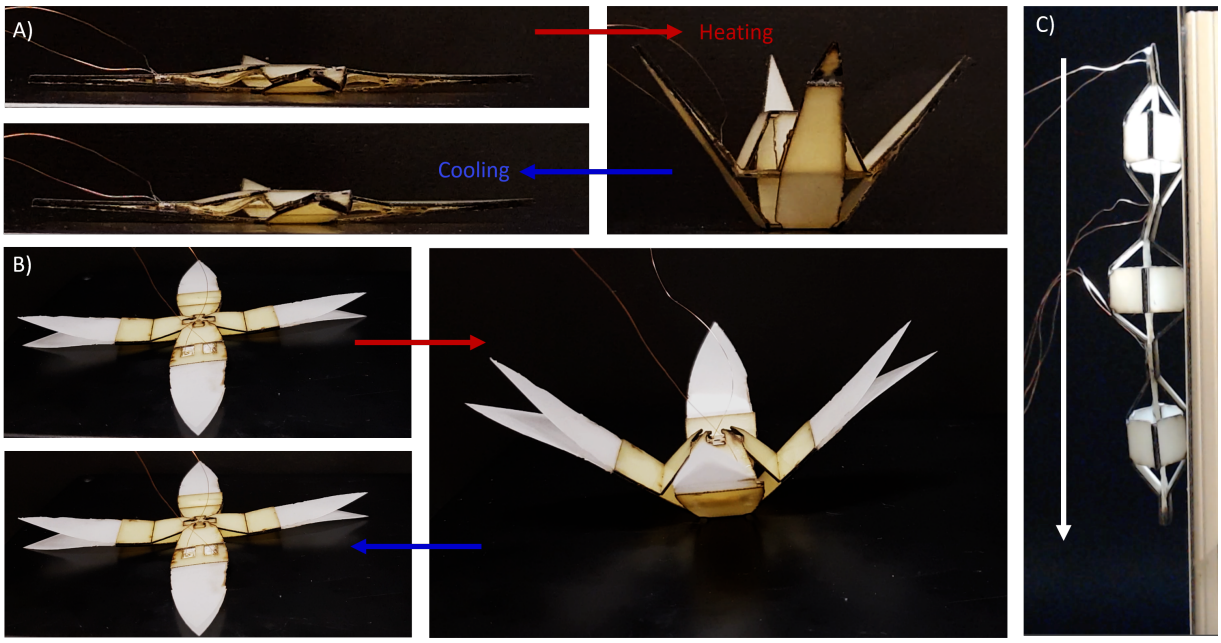

Figure A.6: Reversible self-folding of a Sarrus linkage mechanism module showing its versatility for origami-inspired designs and locomotion, where the red arrows and blue arrows represent the heating and cooling of the embedded LCE actuator, respectively. A) Origami-inspired crane using a Sarrus base module for folding. B) Origami-inspired Lily flower using a Sarrus base module for folding. C) Distributed actuation of the crawler with magnets going down a ferromagnetic vertical surface (Movie S6).

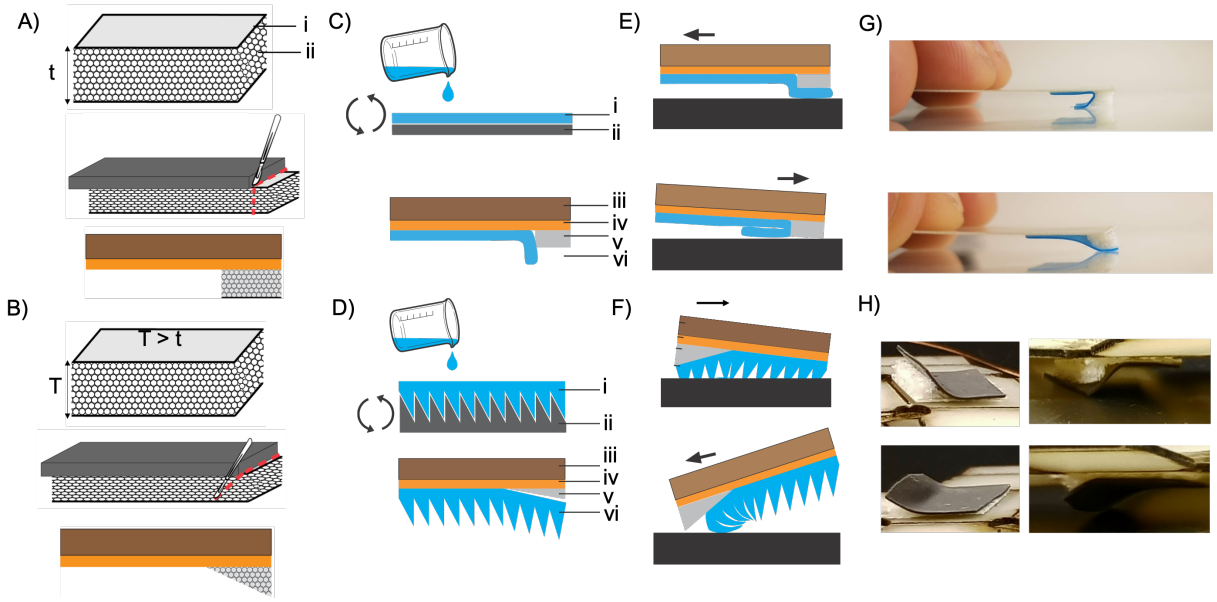

Figure A.7: Fabrication and design concept of the friction pads. A) Schematic of the fabrication process of the foam with rectangular cross-section area. Where i represents the backing of the foam, ii the foam itself, and t the foam pad thickness. B) Schematic of the fabrication process of the foam with triangular cross-section area. Where T is the foam pad thickness. C) Liquid silicone (i) is poured onto a wafer (ii). Spin coating makes an even, thin layer of high friction silicone. The one-way friction foot is assembled. Silicone adhesive (iv) binds an FR4 base (iii) to a low friction foam (v) and the silicone pattern. D) Similar fabrication process of the gecko pads, where the pattern follows the steps described in previous work.E)-F) When a shear load is applied in the preferred direction the silicone is pulled into contact with the surface, giving a high friction. When shear load is applied in the opposite direction, the silicone flap folds backwards and the angle of the foot tilts such that the low friction foam makes contact with the surface. G) Physical representation of the directional pad with the rectangular cross-section area foam. H) Side view of the directional pads with the triangular cross-section area foam design on the crawler upside down or at the ground.

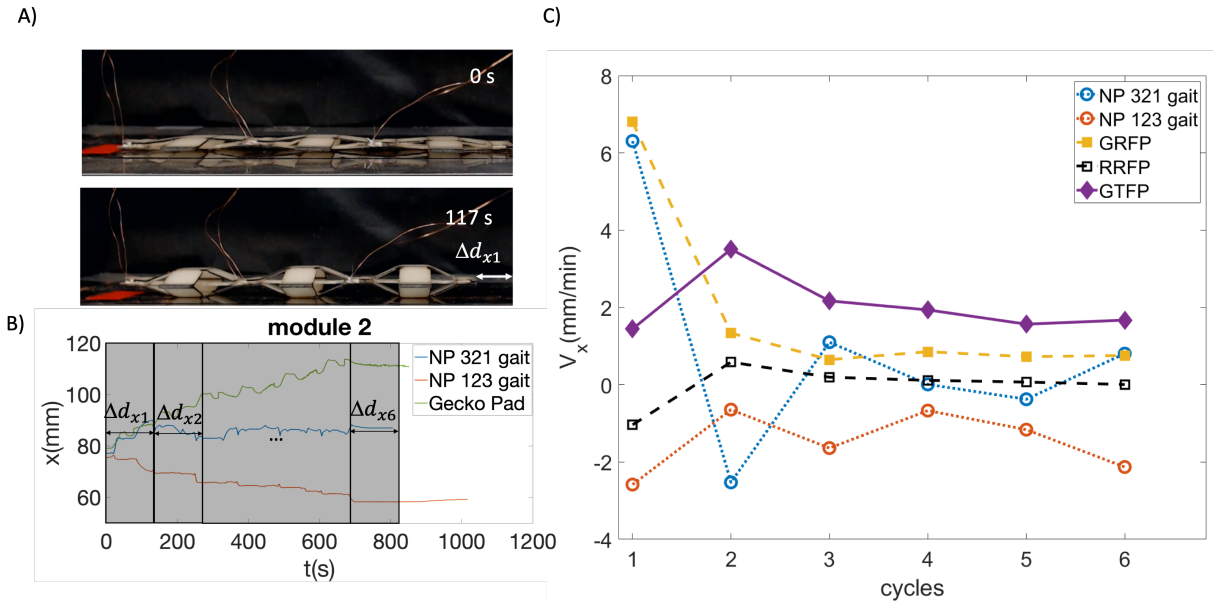

Figure A.8: Performance of the pads per cycle. A) Example of the displacement over the first cycle. B) Data representation of the break down of the horizontal displacement of the crawler per cycle. C) Velocity of the crawler with and without pads per cycle.

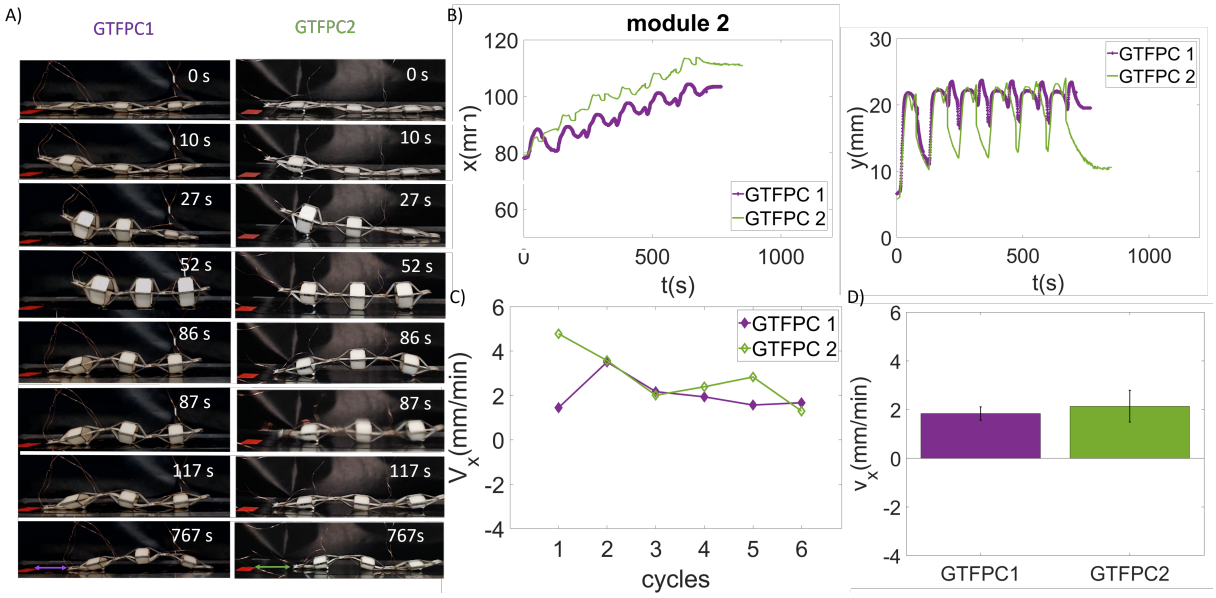

Figure A.9: Repeatable performance of the Gecko-inspired directional friction pad with two different crawlers. A) Displacement of the crawlers with the GTFP over time. B) Tracked locomotion of the second module over time in the x and y axis, respectively. C) Comparison of the crawlers velocities per cycle using the same GTFP.

Appendix B

Supplemental Materials: Soft Power Amplification System for Jumping using Patternable Artificial Muscle and Snap-through of Shells

B.1 Lumped Parameter Model for Jumping Height (t) with a Snap-through Shell

To estimate the jumping height of the robot over time, we used a lumped-parameter model. For simplicity, we used a mass-spring (MS) system that is compressed and released for jumping, equivalent to the configrations of the system immediately and before snapping (Figure B.1A, precompressed and take-off).

Coupling our quasi-static FE simulation with the MS system, we estimated the jumping height by using similar assumptions and steps as in previous work [76]. The stored energy is dependent on the FE simulation results and its assumptions (e.g., vertical reaction force, see

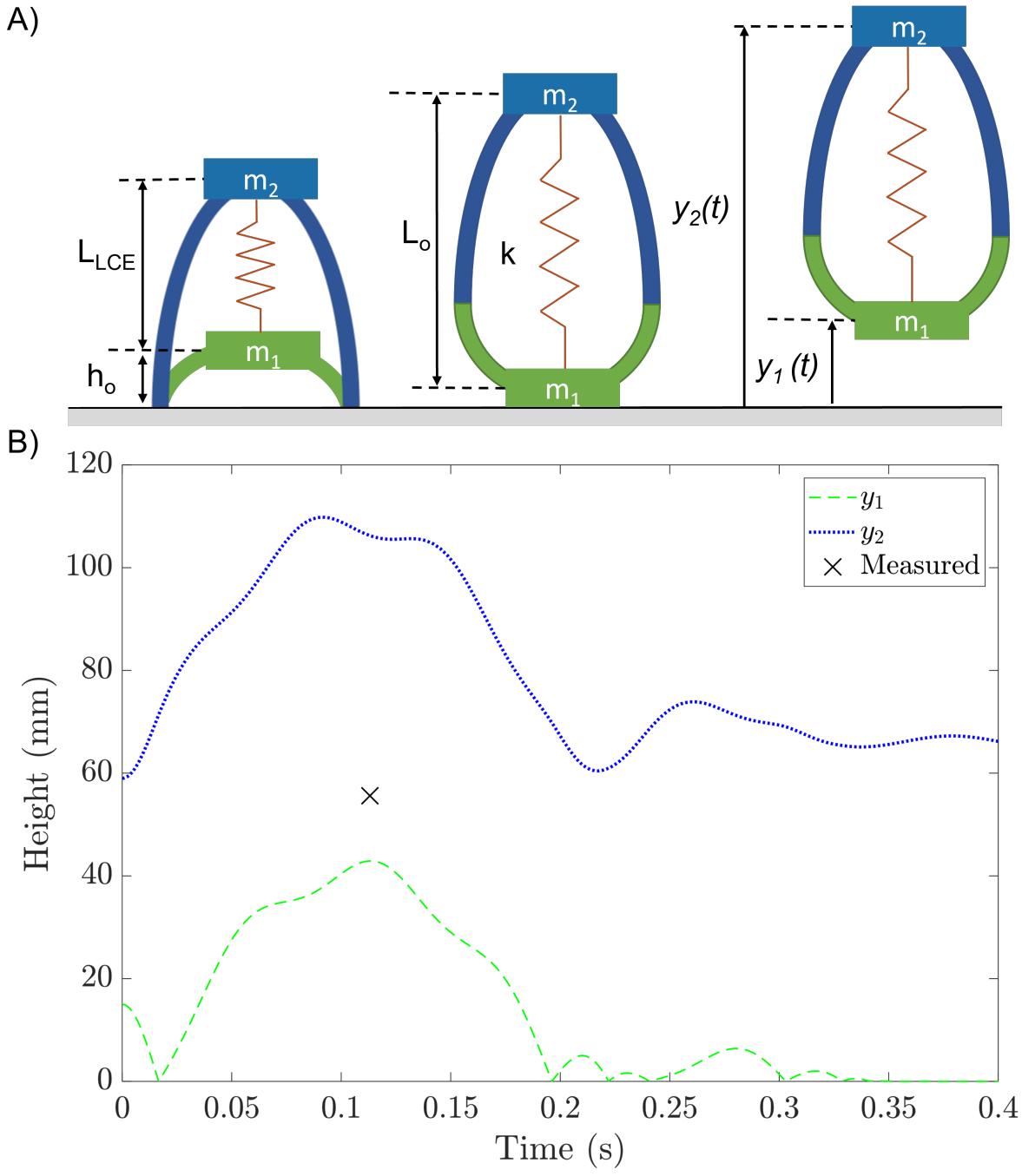

Figure B.1: Lumped parameter model for estimation of the jumping height of the robot over time. A) Schematic of the MS system with its respective initial precompressed, take-off, and airborn states. B) Prediction of the jumping height compared to the value experimentally measured (X).

section Shell Design and Fabrication for Energy Storage). Assumptions for the MS system: i) the system stores an amount of energy equivalent to the numerically simulated energy stored in the shell right before snapping-back (i.e., latch is triggered); ii) the spring is initially precompressed by a ΔL_{LCE} (i.e., contraction of the LCE actuator) making the lower mass being positioned at a distance $h_\circ$; iii) the stiffness of the spring can be approximated as $k = \dfrac{2SE}{\Delta L_{LCE}^2}$, where SE is the strain energy stored based on the shell right before snapping-back; iv) the masses of the system can be concentrated at its extremes.

The equations of motion for the MS system are Equations (B.1, B.2), where $L_\circ$ is the resting position of the spring (i.e., relaxed state of the LCE actuator), m_1 is the lower mass (i.e., shell, magnet, pouch, and payload), m_2 is the upper mass (i.e., top cap, magnet, LCE actuator) and g = 9.81 m/s^2.

$$m_1\ddot{y}_1 + k(y_1 - y_2) = -m_1 g - kL_o \tag{B.1}$$

$$m_2\ddot{y}_2 + k(y_2 - y_1) = -m_2 g + kL_o \tag{B.2}$$

We solved the differential equations using the numerical solver ODE45 of MATLAB, in which the coefficient of restitution used was assumed to be 0.5 [76] and the initial conditions of the system were $[y_{1\circ},\ y_{2\circ},\ \dot{y}_{1\circ},\ \dot{y}_{2\circ}] = [h_\circ,\ h_\circ + L_{LCE},\ 0,\ 0]$. The parameters to solve the equation were m_1 = 0.0327 Kg, m_2 = 0.0325 Kg, $L_\circ$ = 0.068 m, ΔL_{LCE} = 0.024 m (based on the results in the section *Actuator Characterization and Shell Selection*), $h_\circ$ = 0.015 m and SE = 0.0498 J.

The model estimated a maximum jumping height of 42.9 mm at 0.096 s measured from take-off (0.017 s) while the robot achieved a maximum jumping height of 55.6 mm at 0.113 s measured from take-off (0.021 s) (Figure B.1B). Thus, the MS model provided a good prediction for when the events of snapping and maximum height occur over time. For simplicity, we assumed that our model is coupled (i.e., with a constant stiffness before and after snapping with the estimated energy stored right before snapping from FE simulation). Since the actuator is separated from the shell at take-off (i.e., variable stiffness, from stiff to soft behavior when latched

[87]), we believe this assumption could have contributed to the difference between estimated and measured results. Nonetheless, our results provided a comparable first order approximation and can be used to estimate the affect of the system's parameters in its jumping height over time.

Bibliography

[1] K. Saito, S. Nomura, S. Yamamoto, R. Niiyama, and Y. Okabe, "Investigation of hindwing folding in ladybird beetles by artificial elytron transplantation and microcomputed tomography," *Proceedings of the National Academy of Sciences*, vol. 114, no. 22, pp. 5624–5628, 2017.

[2] G. Farley, M. Wise, J. Harrison, G. Sutton, C. Kuo, and S. Patek, "Adhesive latching and legless leaping in small, worm-like insect larvae," *Journal of Experimental Biology*, vol. 222, no. 15, p. jeb201129, 2019.

[3] D. Rus and M. T. Tolley, "Design, fabrication and control of origami robots," *Nature Reviews Materials*, p. 1, 2018.

[4] D. Rus and M. T. Tolley, "Design, fabrication and control of soft robots," *Nature*, vol. 521, no. 7553, pp. 467–475, 2015.

[5] S. M. Felton, M. T. Tolley, B. Shin, C. D. Onal, E. D. Demaine, D. Rus, and R. J. Wood, "Self-folding with shape memory composites," *Soft Matter*, vol. 9, no. 32, pp. 7688–7694, 2013.

[6] Z. Zhakypov, K. Mori, K. Hosoda, and J. Paik, "Designing minimal and scalable insect-inspired multi-locomotion millirobots," *Nature*, vol. 571, no. 7765, pp. 381–386, 2019.

[7] D.-Y. Lee, S.-R. Kim, J.-S. Kim, J.-J. Park, and K.-J. Cho, "Origami wheel transformer: A variable-diameter wheel drive robot using an origami structure," *Soft robotics*, vol. 4, no. 2, pp. 163–180, 2017.

[8] S. Miyashita, S. Guitron, K. Yoshida, S. Li, D. D. Damian, and D. Rus, "Ingestible, controllable, and degradable origami robot for patching stomach wounds," in *Robotics and Automation (ICRA), 2016 IEEE International Conference on*, pp. 909–916, IEEE, 2016.

[9] T. TolleyMichael, F. ShepherdRobert, C. GallowayKevin, J. WoodRobert, and M. WhitesidesGeorge, "A resilient, untethered soft robot," *Soft robotics*, 2014.

[10] R. F. Shepherd, F. Ilievski, W. Choi, S. A. Morin, A. A. Stokes, A. D. Mazzeo, X. Chen, M. Wang, and G. M. Whitesides, "Multigait soft robot," *Proceedings of the national academy of sciences*, vol. 108, no. 51, pp. 20400–20403, 2011.

[11] N. S. Usevitch, Z. M. Hammond, M. Schwager, A. M. Okamura, E. W. Hawkes, and S. Follmer, "An untethered isoperimetric soft robot," *Science Robotics*, vol. 5, no. 40, 2020.

[12] J. D. Madden, N. A. Vandesteeg, P. A. Anquetil, P. G. Madden, A. Takshi, R. Z. Pytel, S. R. Lafontaine, P. A. Wieringa, and I. W. Hunter, "Artificial muscle technology: physical principles and naval prospects," *IEEE Journal of oceanic engineering*, vol. 29, no. 3, pp. 706–728, 2004.

[13] M. D. Hager, S. Bode, C. Weber, and U. S. Schubert, "Shape memory polymers: past, present and future developments," *Progress in Polymer Science*, vol. 49, pp. 3–33, 2015.

[14] M. E. Nisser, S. M. Felton, M. T. Tolley, M. Rubenstein, and R. J. Wood, "Feedback-controlled self-folding of autonomous robot collectives," in *2016 IEEE/RSJ International Conference on Intelligent Robots and Systems (IROS)*, pp. 1254–1261, IEEE, 2016.

[15] A. Firouzeh, Y. Sun, H. Lee, and J. Paik, "Sensor and actuator integrated low-profile robotic origami," in *2013 IEEE/RSJ International Conference on Intelligent Robots and Systems*, pp. 4937–4944, Ieee, 2013.

[16] A. Kotikian, J. M. Morales, A. Lu, J. Mueller, Z. S. Davidson, J. W. Boley, and J. A. Lewis, "Innervated, self-sensing liquid crystal elastomer actuators with closed loop control," *Advanced Materials*, p. 2101814, 2021.

[17] M. J. Ford, C. P. Ambulo, T. A. Kent, E. J. Markvicka, C. Pan, J. Malen, T. H. Ware, and C. Majidi, "A multifunctional shape-morphing elastomer with liquid metal inclusions," *Proceedings of the National Academy of Sciences*, vol. 116, no. 43, pp. 21438–21444, 2019.

[18] C. Ohm, M. Brehmer, and R. Zentel, "Applications of liquid crystalline elastomers," in *Liquid Crystal Elastomers: Materials and Applications*, pp. 49–93, Springer, 2012.

[19] M. Taya, "Micromechanics modeling of smart composites," *Composites Part A: Applied Science and Manufacturing*, vol. 30, no. 4, pp. 531–536, 1999.

[20] O. Sigmund and S. Torquato, "Design of smart composite materials using topology optimization," *Smart Materials and Structures*, vol. 8, no. 3, p. 365, 1999.

[21] Q. Meng and J. Hu, "A review of shape memory polymer composites and blends," *Composites Part A: Applied Science and Manufacturing*, vol. 40, no. 11, pp. 1661–1672, 2009.

[22] M. T. Tolley, S. M. Felton, S. Miyashita, D. Aukes, D. Rus, and R. J. Wood, "Self-folding origami: shape memory composites activated by uniform heating," *Smart Materials and Structures*, vol. 23, no. 9, p. 094006, 2014.

[23] S. M. Felton, M. T. Tolley, C. D. Onal, D. Rus, and R. J. Wood, "Robot self-assembly by folding: A printed inchworm robot," in *Robotics and Automation (ICRA), 2013 IEEE International Conference on*, pp. 277–282, IEEE, 2013.

[24] S. M. Felton, M. T. Tolley, and R. J. Wood, "Mechanically programmed self-folding at the millimeter scale," in *Automation Science and Engineering (CASE), 2014 IEEE International Conference on*, pp. 1232–1237, IEEE, 2014.

[25] S. Felton, M. Tolley, E. Demaine, D. Rus, and R. Wood, "A method for building self-folding machines," *Science*, vol. 345, no. 6197, pp. 644–646, 2014.

[26] J.-H. Na, A. A. Evans, J. Bae, M. C. Chiappelli, C. D. Santangelo, R. J. Lang, T. C. Hull, and R. C. Hayward, "Programming reversibly self-folding origami with micropatterned photo-crosslinkable polymer trilayers," *Advanced Materials*, vol. 27, no. 1, pp. 79–85, 2015.

[27] R. Niiyama, X. Sun, C. Sung, B. An, D. Rus, and S. Kim, "Pouch motors: Printable soft actuators integrated with computational design," *Soft Robotics*, vol. 2, no. 2, pp. 59–70, 2015.

[28] J. Ou, M. Skouras, N. Vlavianos, F. Heibeck, C.-Y. Cheng, J. Peters, and H. Ishii, "aeromorph-heat-sealing inflatable shape-change materials for interaction design," in *Proceedings of the 29th Annual Symposium on User Interface Software and Technology*, pp. 121–132, ACM, 2016.

[29] X. Sun, S. M. Felton, R. Niiyama, R. J. Wood, and S. Kim, "Self-folding and self-actuating robots: A pneumatic approach," in *Robotics and Automation (ICRA), 2015 IEEE International Conference on*, pp. 3160–3165, IEEE, 2015.

[30] S. Ahmed, C. Lauff, A. Crivaro, K. McGough, R. Sheridan, M. Frecker, P. von Lockette, Z. Ounaies, T. Simpson, J.-M. Lien, and R. Strzelec, "Multi-field responsive origami structures: Preliminary modeling and experiments," in *ASME 2013 international design engineering technical conferences and computers and information in engineering conference*, pp. V06BT07A028–V06BT07A028, American Society of Mechanical Engineers, 2013.

[31] K. McGough, S. Ahmed, M. Frecker, and Z. Ounaies, "Finite element analysis and validation of dielectric elastomer actuators used for active origami," *Smart Materials and Structures*, vol. 23, no. 9, p. 094002, 2014.

[32] E. M. Ahmed, "Hydrogel: Preparation, characterization, and applications: A review," *Journal of Advanced Research*, vol. 6, no. 2, pp. 105–121, 2015.

[33] J. M. Jani, M. Leary, A. Subic, and M. A. Gibson, "A review of shape memory alloy research, applications and opportunities," *Materials & Design*, vol. 56, pp. 1078–1113, 2014.

[34] J.-s. Koh, S.-r. Kim, and K.-j. Cho, "Self-folding origami using torsion shape memory alloy wire actuators," in *ASME 2014 International Design Engineering Technical Conferences and Computers and Information in Engineering Conference*, pp. V05BT08A043–V05BT08A043, American Society of Mechanical Engineers, 2014.

[35] A. Firouzeh and J. Paik, "Robogami: a fully integrated low-profile robotic origami," *Journal of Mechanisms and Robotics*, vol. 7, no. 2, p. 021009, 2015.

[36] J. Leng, X. Lan, Y. Liu, and S. Du, "Shape-memory polymers and their composites: stimulus methods and applications," *Progress in Materials Science*, vol. 56, no. 7, pp. 1077–1135, 2011.

[37] H. Meng and G. Li, "A review of stimuli-responsive shape memory polymer composites," *Polymer*, vol. 54, no. 9, pp. 2199–2221, 2013.

[38] S. Petsch, R. Rix, P. Reith, B. Khatri, S. Schuhladen, D. Ruh, R. Zentel, and H. Zappe, "A thermotropic liquid crystal elastomer micro-actuator with integrated deformable micro-heater," in *Micro Electro Mechanical Systems (MEMS), 2014 IEEE 27th International Conference on*, pp. 905–908, IEEE, 2014.

[39] T. J. White and D. J. Broer, "Programmable and adaptive mechanics with liquid crystal polymer networks and elastomers," *Nature materials*, vol. 14, no. 11, pp. 1087–1098, 2015.

[40] M. Warner and E. M. Terentjev, *Liquid crystal elastomers*, vol. 120. OUP Oxford, 2003.

[41] C. Ahn, X. Liang, and S. Cai, "Inhomogeneous stretch induced patterning of molecular orientation in liquid crystal elastomers," *Extreme Mechanics Letters*, vol. 5, pp. 30–36, 2015.

[42] M. Rogóż, H. Zeng, C. Xuan, D. S. Wiersma, and P. Wasylczyk, "Light-driven soft robot mimics caterpillar locomotion in natural scale," *Advanced Optical Materials*, vol. 4, no. 11, pp. 1689–1694, 2016.

[43] T. H. Ware, M. E. McConney, J. J. Wie, V. P. Tondiglia, and T. J. White, "Voxelated liquid crystal elastomers," *Science*, vol. 347, no. 6225, pp. 982–984, 2015.

[44] K. Fuchi, T. H. Ware, P. R. Buskohl, G. W. Reich, R. A. Vaia, T. J. White, and J. J. Joo, "Topology optimization for the design of folding liquid crystal elastomer actuators," *Soft matter*, vol. 11, no. 37, pp. 7288–7295, 2015.

[45] C. Yakacki, M. Saed, D. Nair, T. Gong, S. Reed, and C. Bowman, "Tailorable and programmable liquid-crystalline elastomers using a two-stage thiol–acrylate reaction," *RSC Advances*, vol. 5, no. 25, pp. 18997–19001, 2015.

[46] M. O. Saed, A. H. Torbati, C. A. Starr, R. Visvanathan, N. A. Clark, and C. M. Yakacki, "Thiol-acrylate main-chain liquid-crystalline elastomers with tunable thermomechanical properties and actuation strain," *Journal of Polymer Science Part B: Polymer Physics*, vol. 55, no. 2, pp. 157–168, 2017.

[47] G. L. Wagner and E. Lauga, "Crawling scallop: Friction-based locomotion with one degree of freedom," *Journal of theoretical biology*, vol. 324, pp. 42–51, 2013.

[48] K. Song, E. Yeom, S.-J. Seo, K. Kim, H. Kim, J.-H. Lim, and S. J. Lee, "Journey of water in pine cones," *Scientific reports*, vol. 5, p. 9963, 2015.

[49] S. Ahmed, Z. Ounaies, and M. Frecker, "Investigating the performance and properties of dielectric elastomer actuators as a potential means to actuate origami structures," *Smart Materials and Structures*, vol. 23, no. 9, p. 094003, 2014.

[50] E. Hawkes, B. An, N. M. Benbernou, H. Tanaka, S. Kim, E. Demaine, D. Rus, and R. J. Wood, "Programmable matter by folding," *Proceedings of the National Academy of Sciences*, vol. 107, no. 28, pp. 12441–12445, 2010.

[51] S. Petsch, R. Rix, B. Khatri, S. Schuhladen, P. Müller, R. Zentel, and H. Zappe, "Smart artificial muscle actuators: Liquid crystal elastomers with integrated temperature feedback," *Sensors and Actuators A: Physical*, vol. 231, pp. 44–51, 2015.

[52] R. S. Kularatne, H. Kim, J. M. Boothby, and T. H. Ware, "Liquid crystal elastomer actuators: Synthesis, alignment, and applications," *Journal of Polymer Science Part B: Polymer Physics*, vol. 55, no. 5, pp. 395–411, 2017.

[53] A. Kotikian, R. L. Truby, J. W. Boley, T. J. White, and J. A. Lewis, "3d printing of liquid crystal elastomeric actuators with spatially programed nematic order," *Advanced Materials*, 2018.

[54] C. P. Ambulo, J. J. Burroughs, J. M. Boothby, H. Kim, M. R. Shankar, and T. H. Ware, "Four-dimensional printing of liquid crystal elastomers," *ACS applied materials & interfaces*, vol. 9, no. 42, pp. 37332–37339, 2017.

[55] M. López-Valdeolivas, D. Liu, D. J. Broer, and C. Sánchez-Somolinos, "4d printed actuators with soft-robotic functions," *Macromolecular rapid communications*, 2017.

[56] A. Kotikian, C. McMahan, E. C. Davidson, J. M. Muhammad, R. D. Weeks, C. Daraio, and J. A. Lewis, "Untethered soft robotic matter with passive control of shape morphing and propulsion," *Science Robotics*, vol. 4, no. 33, pp. Art–No, 2019.

[57] J. Ortín and L. Delaey, "Hysteresis in shape-memory alloys," *International Journal of Non-Linear Mechanics*, vol. 37, no. 8, pp. 1275–1281, 2002.

[58] J. Cui, T.-Y. Huang, Z. Luo, P. Testa, H. Gu, X.-Z. Chen, B. J. Nelson, and L. J. Heyderman, "Nanomagnetic encoding of shape-morphing micromachines," *Nature*, vol. 575, no. 7781, pp. 164–168, 2019.

[59] E. A. Peraza-Hernandez, D. J. Hartl, R. J. Malak Jr, and D. C. Lagoudas, "Origami-inspired active structures: a synthesis and review," *Smart Materials and Structures*, vol. 23, no. 9, p. 094001, 2014.

[60] C. Yuan, D. J. Roach, C. K. Dunn, Q. Mu, X. Kuang, C. M. Yakacki, T. Wang, K. Yu, and H. J. Qi, "3d printed reversible shape changing soft actuators assisted by liquid crystal elastomers," *Soft Matter*, vol. 13, no. 33, pp. 5558–5568, 2017.

[61] D. J. Roach, X. Kuang, C. Yuan, K. Chen, and H. J. Qi, "Novel ink for ambient condition printing of liquid crystal elastomers for 4d printing," *Smart Materials and Structures*, vol. 27, no. 12, p. 125011, 2018.

[62] A. Minori, S. Jadhav, Q. He, S. Cai, and M. Tolley, "Reversible actuation of origami inspired composites using liquid crystal elastomers," in *ASME 2017 Conference on Smart Materials, Adaptive Structures and Intelligent Systems*, pp. V001T08A015–V001T08A015, American Society of Mechanical Engineers, 2017.

[63] Q. He, Z. Wang, Y. Wang, A. Minori, M. T. Tolley, and S. Cai, "Electrically controlled liquid crystal elastomer–based soft tubular actuator with multimodal actuation," *Science Advances*, vol. 5, no. 10, p. eaax5746, 2019.

[64] C. Wang, K. Sim, J. Chen, H. Kim, Z. Rao, Y. Li, W. Chen, J. Song, R. Verduzco, and C. Yu, "Soft ultrathin electronics innervated adaptive fully soft robots," *Advanced Materials*, vol. 30, no. 13, p. 1706695, 2018.

[65] P. S. Sreetharan, J. P. Whitney, M. D. Strauss, and R. J. Wood, "Monolithic fabrication of millimeter-scale machines," *Journal of Micromechanics and Microengineering*, vol. 22, no. 5, p. 055027, 2012.

[66] H. Fang, C. Wang, S. Li, K. Wang, and J. Xu, "A comprehensive study on the locomotion characteristics of a metameric earthworm-like robot," *Multibody System Dynamics*, vol. 35, no. 2, pp. 153–177, 2015.

[67] S. Das, N. Cadirov, S. Chary, Y. Kaufman, J. Hogan, K. L. Turner, and J. N. Israelachvili, "Stick–slip friction of gecko-mimetic flaps on smooth and rough surfaces," *Journal of The Royal Society Interface*, vol. 12, no. 104, p. 20141346, 2015.

[68] A. Parness, D. Soto, N. Esparza, N. Gravish, M. Wilkinson, K. Autumn, and M. Cutkosky, "A microfabricated wedge-shaped adhesive array displaying gecko-like dynamic adhesion, directionality and long lifetime," *Journal of the Royal Society Interface*, vol. 6, no. 41, pp. 1223–1232, 2009.

[69] B. A. Trimmer, A. E. Takesian, B. M. Sweet, C. B. Rogers, D. C. Hake, and D. J. Rogers, "Caterpillar locomotion: a new model for soft-bodied climbing and burrowing robots," in *7th International Symposium on Technology and the Mine Problem*, vol. 1, pp. 1–10, Mine Warfare Association Monterey, CA, 2006.

[70] J. Brackenbury, "Fast locomotion in caterpillars," *Journal of insect physiology*, vol. 45, no. 6, pp. 525–533, 1999.

[71] Q. He, Z. Wang, Z. Song, and S. Cai, "Bioinspired design of vascular artificial muscle," *Advanced Materials Technologies*, vol. 4, no. 1, p. 1800244, 2019.

[72] M. Luo, Y. Pan, E. H. Skorina, W. Tao, F. Chen, S. Ozel, and C. D. Onal, "Slithering towards autonomy: a self-contained soft robotic snake platform with integrated curvature sensing," *Bioinspiration & biomimetics*, vol. 10, no. 5, p. 055001, 2015.

[73] N. W. Bartlett, M. T. Tolley, J. T. Overvelde, J. C. Weaver, B. Mosadegh, K. Bertoldi, G. M. Whitesides, and R. J. Wood, "A 3d-printed, functionally graded soft robot powered by combustion," *Science*, vol. 349, no. 6244, pp. 161–165, 2015.

[74] M. T. Tolley, R. F. Shepherd, M. Karpelson, N. W. Bartlett, K. C. Galloway, M. Wehner, R. Nunes, G. M. Whitesides, and R. J. Wood, "An untethered jumping soft robot," in *2014 IEEE/RSJ International Conference on Intelligent Robots and Systems*, pp. 561–566, IEEE, 2014.

[75] M. Duduta, F. Berlinger, R. Nagpal, D. Clarke, R. Wood, and F. Z. Temel, "Electrically-latched compliant jumping mechanism based on a dielectric elastomer actuator," *Smart Materials and Structures*, vol. 28, no. 9, p. 09LT01, 2019.

[76] B. Gorissen, D. Melancon, N. Vasios, M. Torbati, and K. Bertoldi, "Inflatable soft jumper inspired by shell snapping," *Science Robotics*, vol. 5, no. 42, 2020.

[77] S. Longo, S. Cox, E. Azizi, M. Ilton, J. Olberding, R. St Pierre, and S. Patek, "Beyond power amplification: latch-mediated spring actuation is an emerging framework for the study of diverse elastic systems," *Journal of Experimental Biology*, vol. 222, no. 15, p. jeb197889, 2019.

[78] Y. Forterre, J. M. Skotheim, J. Dumais, and L. Mahadevan, "How the venus flytrap snaps," *Nature*, vol. 433, no. 7024, pp. 421–425, 2005.

[79] C. Ahn, X. Liang, and S. Cai, "Bioinspired design of light-powered crawling, squeezing, and jumping untethered soft robot," *Advanced Materials Technologies*, vol. 4, no. 7, p. 1900185, 2019.

[80] M. Ilton, M. S. Bhamla, X. Ma, S. M. Cox, L. L. Fitchett, Y. Kim, J.-s. Koh, D. Krishnamurthy, C.-Y. Kuo, F. Z. Temel, and A. Crosby, "The principles of cascading power limits in small, fast biological and engineered systems," *Science*, vol. 360, no. 6387, 2018.

[81] T. Chen, O. R. Bilal, K. Shea, and C. Daraio, "Harnessing bistability for directional propulsion of soft, untethered robots," *Proceedings of the National Academy of Sciences*, vol. 115, no. 22, pp. 5698–5702, 2018.

[82] A. F. Minori, Q. He, P. E. Glick, I. Adibnazari, A. Stopol, S. Cai, and M. T. Tolley, "Reversible actuation for self-folding modular machines using liquid crystal elastomer," *Smart Materials and Structures*, vol. 29, no. 10, p. 105003, 2020.

[83] D. L. Thomsen, P. Keller, J. Naciri, R. Pink, H. Jeon, D. Shenoy, and B. R. Ratna, "Liquid crystal elastomers with mechanical properties of a muscle," *Macromolecules*, vol. 34, no. 17, pp. 5868–5875, 2001.

[84] H. Tian, Z. Wang, Y. Chen, J. Shao, T. Gao, and S. Cai, "Polydopamine-coated main-chain liquid crystal elastomer as optically driven artificial muscle," *ACS applied materials & interfaces*, vol. 10, no. 9, pp. 8307–8316, 2018.

[85] A. Gordon, A. F. Huxley, and F. Julian, "The variation in isometric tension with sarcomere length in vertebrate muscle fibres," *The Journal of physiology*, vol. 184, no. 1, pp. 170–192, 1966.

[86] M. Rosario, G. Sutton, S. Patek, and G. Sawicki, "Muscle–spring dynamics in time-limited, elastic movements," *Proceedings of the Royal Society B: Biological Sciences*, vol. 283, no. 1838, p. 20161561, 2016.

[87] S. Sadeghi, S. R. Allison, B. Bestill, and S. Li, "Tmp origami jumping mechanism with nonlinear stiffness," *Smart Materials and Structures*, vol. 30, no. 6, p. 065002, 2021.

[88] S. Sadeghi, B. D. Betsill, P. Tallapragada, and S. Li, "The effect of nonlinear springs in jumping mechanisms," in *Dynamic Systems and Control Conference*, vol. 51890, p. V001T04A002, American Society of Mechanical Engineers, 2018.

[89] Y. Kim, J. van den Berg, and A. J. Crosby, "Autonomous snapping and jumping polymer gels," *Nature Materials*, pp. 1–7, 2021.

[90] N. P. Bende, A. A. Evans, S. Innes-Gold, L. A. Marin, I. Cohen, R. C. Hayward, and C. D. Santangelo, "Geometrically controlled snapping transitions in shells with curved creases," *Proceedings of the National Academy of Sciences*, vol. 112, no. 36, pp. 11175–11180, 2015.

[91] A. Madhukar, D. Perlitz, M. Grigola, D. Gai, and K. J. Hsia, "Bistable characteristics of thick-walled axisymmetric domes," *International Journal of Solids and Structures*, vol. 51, no. 14, pp. 2590–2597, 2014.

[92] A. Brinkmeyer, M. Santer, A. Pirrera, and P. Weaver, "Pseudo-bistable self-actuated domes for morphing applications," *International Journal of Solids and Structures*, vol. 49, no. 9, pp. 1077–1087, 2012.

[93] M. Gomez, D. E. Moulton, and D. Vella, "Dynamics of viscoelastic snap-through," *Journal of the Mechanics and Physics of Solids*, vol. 124, pp. 781–813, 2019.

[94] M. Santer, "Self-actuated snap back of viscoelastic pulsing structures," *International Journal of Solids and Structures*, vol. 47, no. 24, pp. 3263–3271, 2010.

[95] K. Narumi, H. Sato, K. Nakahara, Y. ah Seong, K. Morinaga, Y. Kakehi, R. Niiyama, and Y. Kawahara, "Liquid pouch motors: Printable planar actuators driven by liquid-to-gas phase change for shape-changing interfaces," *IEEE Robotics and Automation Letters*, vol. 5, no. 3, pp. 3915–3922, 2020.

[96] Z. Wang, A. A. Volinsky, and N. D. Gallant, "Crosslinking effect on polydimethylsiloxane elastic modulus measured by custom-built compression instrument," *Journal of Applied Polymer Science*, vol. 131, no. 22, 2014.

[97] A. Samy, M. Mahmoud, M. Khashaba, and W. Ali, "Friction of rubber sliding against ceramics part i dry and water lubricated conditions," *KGK. Kautschuk, Gummi, Kunststoffe*, vol. 60, no. 6, pp. 322–327, 2007.

[98] D. Santos, M. Spenko, A. Parness, S. Kim, and M. Cutkosky, "Directional adhesion for climbing: theoretical and practical considerations," *Journal of Adhesion Science and Technology*, vol. 21, no. 12-13, pp. 1317–1341, 2007.

[99] E. W. Hawkes, E. V. Eason, D. L. Christensen, and M. R. Cutkosky, "Human climbing with efficiently scaled gecko-inspired dry adhesives," *Journal of The Royal Society Interface*, vol. 12, no. 102, p. 20140675, 2015.

[100] H. Jiang, E. W. Hawkes, C. Fuller, M. A. Estrada, S. A. Suresh, N. Abcouwer, A. K. Han, S. Wang, C. J. Ploch, A. Parness, and M. Cutkosky, "A robotic device using gecko-inspired adhesives can grasp and manipulate large objects in microgravity," *Science Robotics*, vol. 2, no. 7, p. eaan4545, 2017.

[101] A. Kalantari, K. Mahajan, D. Ruffatto, and M. Spenko, "Autonomous perching and take-off on vertical walls for a quadrotor micro air vehicle," in *2015 IEEE International Conference on Robotics and Automation (ICRA)*, pp. 4669–4674, IEEE, 2015.

[102] P. Glick, S. A. Suresh, D. Ruffatto, M. Cutkosky, M. T. Tolley, and A. Parness, "A soft robotic gripper with gecko-inspired adhesive," *IEEE Robotics and Automation Letters*, vol. 3, no. 2, pp. 903–910, 2018.

[103] E. W. Hawkes, H. Jiang, D. L. Christensen, A. K. Han, and M. R. Cutkosky, "Grasping without squeezing: Design and modeling of shear-activated grippers," *IEEE Transactions on Robotics*, vol. 34, no. 2, pp. 303–316, 2017.

[104] D. L. Christensen, E. W. Hawkes, S. A. Suresh, K. Ladenheim, and M. R. Cutkosky, "μtugs: Enabling microrobots to deliver macro forces with controllable adhesives," in *2015 IEEE International Conference on Robotics and Automation (ICRA)*, pp. 4048–4055, IEEE, 2015.

[105] S. A. Suresh, C. F. Kerst, M. R. Cutkosky, and E. W. Hawkes, "Spatially variant microstructured adhesive with one-way friction," *Journal of the Royal Society Interface*, vol. 16, no. 150, p. 20180705, 2019.

[106] E. W. Hawkes, D. L. Christensen, and M. R. Cutkosky, "Vertical dry adhesive climbing with a 100$\times$ bodyweight payload," in *2015 IEEE International Conference on Robotics and Automation (ICRA)*, pp. 3762–3769, IEEE, 2015.